Title

Optoelectronic and bioelectrochemical characteristics of graphene integrated devices

Permalink

https://escholarship.org/uc/item/2009r49x

Author

Dong, Yongliang

Publication Date

2022

Peer reviewed|Thesis/dissertation

UNIVERSITY OF CALIFORNIA SAN DIEGO

Optoelectronic and bioelectrochemical characteristics of graphene integrated devices

A Dissertation submitted in partial satisfaction of the requirements
for the degree Doctor of Philosophy

in

Materials Science and Engineering

by

Yongliang Dong

Committee in charge:

Professor Prabhakar Bandaru, Chair
Professor Michael Fogler
Professor Javier Garay
Professor Vitaliy Lomakin
Professor Oscar Vazquez Mena

2022

The Dissertation of Yongliang Dong is approved, and it is acceptable
in quality and form for publication on microfilm and electronically.

University of California San Diego

2022

DEDICATION

To my wife, my loved one, and my best friend, Xiaochen Li, who always accompany me and encourage, and support me through all the challenging circumstances.

To my family, who supported me in every stage of my life and always stand with me.

To my academic advisor, Prof. Prabhakar Bandaru, who supported and guided me through my Ph.D. research and future career.

TABLE OF CONTENTS

LIST OF FIGURES

LIST OF TABLES

ACKNOWLEDGEMENTS

First, I would like to thank my academic supervisor Dr. Prabhakar Bandaru, who provided support and guidance through my thesis research and career development. I appreciate his suggestions, time, and research ideas in both numerical analysis study and experimental research investigation. His ideas with multidisciplinary research background helped me to convert the research idea into my thesis research. His physics insight into the modeling provided me with a deeper understanding of the result and deliver clear conclusions into publications. His academic and industrial expertise guided me to career opportunities after academic research. In addition, I would like to thank his suggestion to improve my communication and oral presentation skills. He is a great supervisor with patience and expertise, I am appreciated to be in his group.

Next, I want to thank my thesis dissertation committees: Dr. Michael Fogler, Dr. Javier Garay, Dr. Vitaliy Lomakin, and Dr. Oscar Vazquez Mena for their time and suggestions for my thesis research. Their comments provided me with a tight direction in research. I would like to thank Dr. Michael Fogler and Dr. Vitaliy Lomakin for their suggestions in the numerical study of surface plasmonics resonance. I am also wanting to thank Dr. Javier Garay and Dr. Oscar Vazquez Mena for their patience and enthusiasm.

I would like to thank Dr. Deependra Kumar Ban and Dr. Ratneshwar Lal for their collaboration in incorporating graphene field-effect transistors with biomolecular sensor development. I want to thank them for their time and valuable guidance in both experiments and paper preparations.

I also want to thank all my group members. I want to thank the help from Sreyam Natani for the fabrication and measurements of the graphene field effect transistor. I also want to thank Dr. Nirjhar Sarkar, Dr. Erick Martinez Loran, and Dr. Anna Alexander for helping me onboard with my numerical and experimental skills. I want to thank Dr. Hidenori Yamada for the valuable suggestions in the physical models of my research projects. And Dr. Yun Zhou, Dr. Bei Fan, Dr. Peng Chen, Zichen Zhang, Li Cheng, Alex Lee, Kesong Wang for all the help and support in the lab.

I would like to especially thank my wife, Xiaochen Li, for her companionship and support throughout my academic study and life. We married in 2021 during the tough time of the pandemic and we share each other love, honor, and happiness. I am so thankful I have her with me from now till the end.

Finally, I also want to say great thanks to my parents, Qiuhong Yang and Xiangsheng Dong, who guided my entire life. I want to thank them for all their support during every stage of my study and life. I cannot be where I am right now without them.

The material in this dissertation is based on the following papers which are published or submitted.

Chapter 2, in full, is a reprint of the material as it appears in Dong, Yongliang, and Prabhakar R. Bandaru. "Interaction and hybridization of orthogonal Fabry-Pérot like surface plasmon modes in metal-dielectric grating structures." *Optics express* 28.3 (2020): 3541-3551. The dissertation author was the primary investigator and author of this paper

Chapter 3, in full, is a reprint of the material as it appears in Dong, Yongliang, and Prabhakar R. Bandaru. "Enhanced graphene surface plasmonics through incorporation into metallic nanostructures." *Optics Express* 30.17 (2022): 30696-30704. The dissertation author was the primary investigator and author of this paper

Chapter 4, in full, has been submitted for publication of the material as it may appear in ACS Applied Nano Materials, 2022, Yongliang Dong, Alex W. Lee, Deependra Kumar Ban, Kesong Wang, Prabhakar Bandaru, 2022. The dissertation author was the primary researcher and author of this paper.

VITA

2015	Bachelor of Science in Applied Physics, Beihang University, Beijing, China
2018	Master of Science in Material Science and Engineering, University of California San Diego, La Jolla, CA, United States
2022	Doctor of Philosophy in Material Science and Engineering, University of California San Diego, La Jolla, CA, United States

ABSTRACT OF THE DISSERTATION

Optoelectronic and bioelectrochemical characteristics of graphene integrated devices

by

Yongliang Dong

Doctor of Philosophy in Materials Science and Engineering

University of California San Diego, 2022

Professor Prabhakar Bandaru, Chair

This dissertation focuses on the development of graphene integrated devices for optoelectronics and bioelectrochemical applications. The numerical finite element method revealed improvement of surface plasmonics resonance (SPP) refractive index sensor with graphene. A methodology for enhancing the SPP resonance associated with graphene, through nanoscale metal-dielectric-metal (MDM) gaps, is proposed. In addition, the electrolyte gated field effect transistor integrated with graphene is investigated for bioelectrochemical application, providing motivation for development of portable, label free, point of care (POC) devices with both high specificity and sensitivity.

INTRODUCTION

Sensor technology

In modern research and industry, sensor plays an important role to detect, identify and analyze the physical phenomenon from different disciplinaries. For example, the change of the environment/sample such as temperature, pH, elements near the sensor can be translate into the sensing signal. It has been shown that the development of material engineering and science plays an important role for manifesting the sensor performance and reducing the cost. For example, the temperature sensor was initially developed by resistance measurement by using various materials at the beginning of 90 century, and later on the sensitivity of the resistance temperature sensor was significant improved by the copper resistance [1]. In the recent decades, the expansion of semiconductor industry realized the large-scale silicon top-down fabrication. By doing the patterning and tuning the semiconductor material properties, people could generate a new way to convert the sensing physical phenomena into signals which can be easily managed through a computer. the evolutionary development of material technology and new materials will provide better sensor material properties and behaviors, generate advanced new sensors features, such as higher sensitivity up to atomic scale, lower cost, and rapid detection of physical properties.

The sensors are widely implemented in biological/medical point of care detection, which requires the detection of certain biological reaction or the existence of certain biomolecules. The goal for biological/medical sensors (or named biosensors) is to achieve rapid diagnostics with a desired limit of detection. There are many applications of the biosensors, for instance, diagnostic certain disease, drug development, and identification of certain pollutants in the environment and so on. Biosensors are able to translate the biochemical reaction or existence of specific molecules into signals for analysis, with respect to the reference analyte [2].

To achieve the detection, the biosensors are usually consisting of bioreceptors (for specifically diagnostic), transducer (for translating sensing phenomenon into digital/analytical signals). The response of the sensor will be translated through detector signals (optical/chemistry/electronics, and so on) and analyzed based on the threshold of the response signal. Such biosensor application requires certain level of sensitivity, stability and specificity/selectivity, etc. The sensitivity stands for the minimum amount of target analyte that can be identified by the biosensor, i.e., for pollutants in our water system the sensitivity means the minimum concentration of pollutant element/molecules. The stability/sustainability means how will the biosensors remain the function within the ambient environment. As for the specificity, it attributes to how accurate the biosensor can distinguish the target analyte from other analytes. The growth of biosensors market has attracted academia and industrial efforts to invent new technologies for better biosensors.

Nanotechnology in Sensing Application

In recent years, high throughput nanofabrication methods been introduced in industry, manifest the development in various filed. In biosensor application point of view, the nanotechnology has been contributing to the development of sensors performance in various reasons: The better signal to noise ratio, attributes to the smaller size of biosensors, say in nanoscale; The lower cost of analytes/samples, the cost of detection has been reduced since only small amount of sample is required for nanoscale sensor technology; The surface-volume ratio is higher for nanoscale biosensor devices, indicating improved specification through bioreceptors binding and manifested binding efficiency at the sensing surface.

One of the major approaches for nanoscale sensor devices is the new material development, which paves new way of sensor improvement. There are many efforts done to find new material which has high sensitivity, stability, and sustainability in the real application. Low dimensional materials were showing promising performance in the sensor material family, such as metallic nanowires (one-dimension, or 1D) and graphene (two-dimension, 2D) materials [3]. Such low dimensional materials have better signal to noise ratio and higher surface to volume ratio, which make them to be appropriate for biosensor application at nanoscale [4].

Deployment of Graphene in Sensing Application

The 2010 physics Noble Prize was awarded to the groundbreaking experiment achievement in real 2-dimensional material graphene, an atomic layer of sp^2-hybridized carbon sheet that easily exfoliated by the tape or fabricated by chemical vapor deposition. Since then, the 2D graphene has been extensively studied and demonstrated the extraordinary physical properties in electrical, thermal, and mechanical: from the electrical measurement, the ambipolar field effect is observed representing the charge carrier shifting between electrons and holes; besides, the high carrier mobility is revealed by the quantum Hall effect measurement, indicating the high thermal and electrical conductivity. Therefore, there is huge interest in the application of graphene in various devices. The initial mechanical exfoliation has difficulty in scalable devices, whereas the chemical vapor deposition (CVD) methods compile with silicon nanofabrication methods paves the way of device application, in high-speed electronics, single molecular detection and etc. [5].

Surface Plasmonics polarization (SPP) in Sensing Application

One of the approaches for sensing technology is called the surface plasmoncis polarization (SPP) resonance sensing, which showed high sensitivity in the change of the surface refractive index and was extensively implemented in surface analytes characteristics. Recently, the SPP resonance sensor has been developed further with the application of new materials such as graphene.

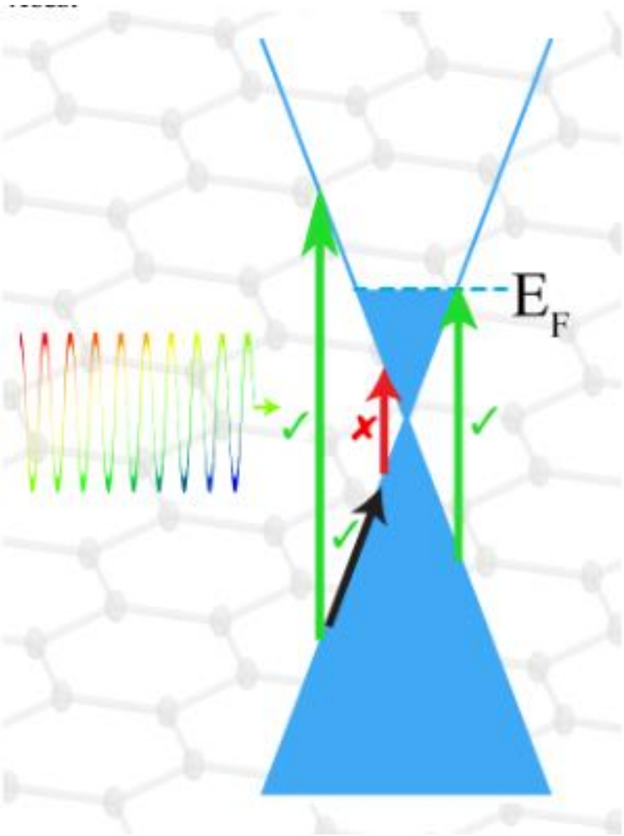

Figure1. 1 The graphene SPP resonances and graphene Fermi level [6]

The advantages of deploying graphene in SPP sensors are the following [6]:

1. The dynamical tunability of graphene optical properties, enabling the modulation of the SPP for various sensing applications.
2. The optimized confinement of graphene intrinsic SPP because of the nature of 2D material.

The tunability of graphene optical properties is dependent on the band stricture of graphene in reciprocal space, in which the conduction band and valance band touches at the first Brillouin zone showing ambipolar effect named as Dirac point, as shown in Figure1. 1. As the optical properties are directly related to the electronic properties of graphene, the doping carrier density could strongly modulate the optical intraband and interband transitions and therefore change the optical conductivity and the permittivity.

The approach of designing the graphene implemented SPP sensors could be investigated through the numerical modeling method. For example, the finite element simulation method, using the discrete grain structure and finite element frequency domain boundaries to calculate the SPP resonance mode in the deigned structure.

In our work, we implemented the graphene into molecular detection through the SPP, which was done numerically by finite-element simulation (commercial software COMSOL Multiphysics) with metallic nanostructure.

The graphene SPP and related sensing application finite element study contains two chapter: in Chapter 2, the detailed study has been done for SPP in metallic nanostructure, investigating the SPP resonance absorption coupling effect at certain frequency and geometry. Chapter 3 follows the simulation work in metallic SPP with graphene integrated, potential high sensitivity has been shown from far field spectra.

Electrolyte Gated Field Effect Transistor in Sensing Application

Another well-known type of sensor is the electronic field effect transistor (FET) sensor which can transduce the sensing media change into the electronic signal and been implemented in life science, chemical and physical sensing applications. The advantages of the FET sensors are based on the high sensitivity of the electronic signal detection and the high throughput low-cost fabrications from the semiconductor manufacturing facilities. Generally, the sensitivity of the FET based sensor is interpreted as the change of surface potential, as shown in Figure1. 2, where the electronic potential applied channel of the FET (semiconductor or graphene etc.) will changed the channel properties based on the characteristic of target materials [7].

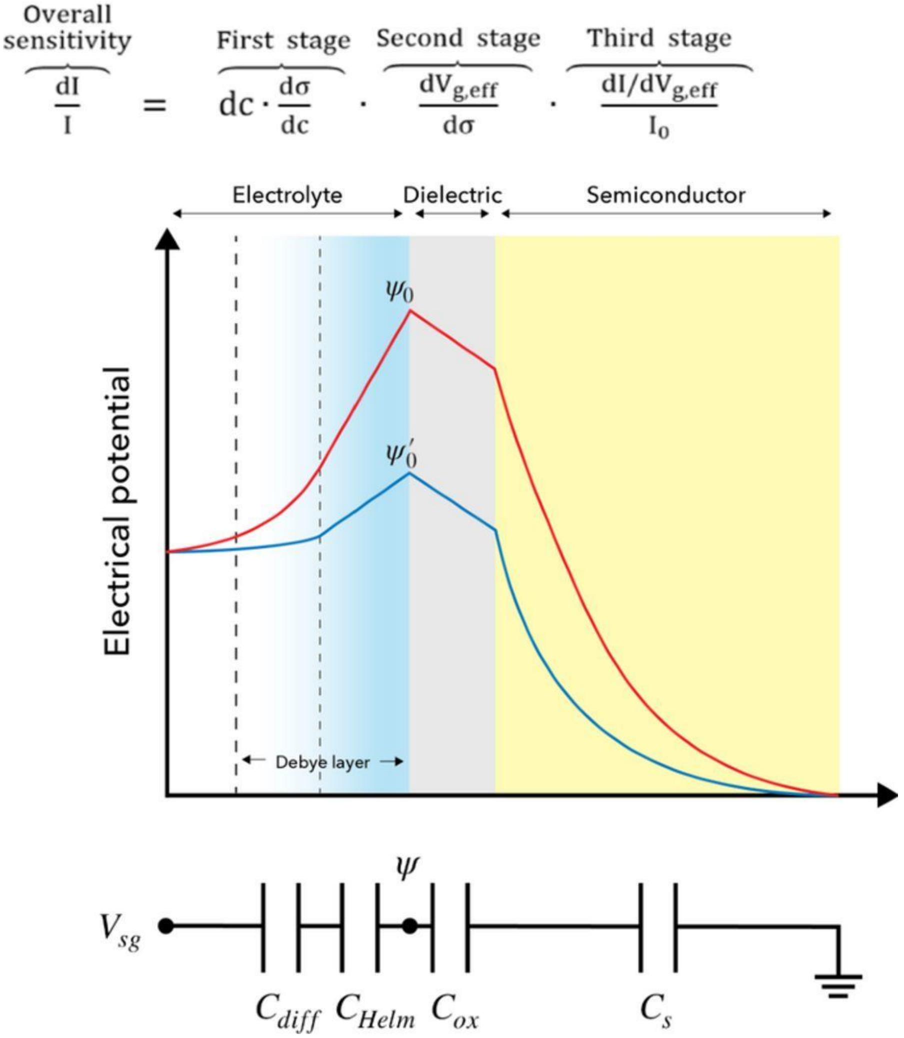

Figure1. 2 The electrical potential profile near the electrolyte and channel interface of the FET based sensor [7].

In the application of biosensor, for example, the FET based sensors are well implemented in the detection/diagnostics of the heavy metal ions, nucleotides, protein, antigen, diseases etc. The principle of the detection is based on the electronic potential change from the liquid and solid interfaces, which will apply an additional potential on the gate of the FET and change the electron characteristics in the measurements. The change of the potential is usually modulated by the designed functional surface group such as single strand nucleotides, antibody, aptamer etc. To the point of care technology development, a threshold voltage and limit of detection is usually defined to interpret the sensitivity of the sensor.

The graphene has the promising electronic behaviors such as high carrier mobility, mechanical strength and compatible to the semiconductor device platform. With the modulation of surface potential, the graphene can be tuned by the positive or negative electric field and generate electron and holes, respectively. The switching of main carriers is the ambipolar effect of graphene and could be observed as a V-shape curved I_{ds} over V_g, where the minimum of conductivity point is the charge neutral point (or Dirac point). Near the Dirac, the graphene served as the channel material is very sensitive to the modification of surface electric potential therefore can be used for sensing applications.

The second part of my graphene sensor research is implementing the electronics graphene FET (GFET) biosensor platform for ultrasensitive sensor platform development and improvement. In Chapter 4, we demonstrated an ultrasensitive lead ion detection through GFET, with detailed understanding through Hills-Langmuir mechanism and capacitance modeling.

Chapter 2. Interaction and hybridization of orthogonal Fabry-Pérot like surface plasmon modes in metal-dielectric grating structures

Introduction

The interaction of specific surface plasmon modes in metal-dielectric-metal arrangements is investigated, motivated by their relevance to device-based configurations. The absorption spectra of the relevant nanostructures considering geometrical variation, such as the width and height of the metal or dielectric, are probed considering such interactions. Frequency domain simulations are used to study related multiple surface plasmon polariton resonance modes. It is indicated that the resonant energy level interaction due to the coupling between modes in a horizontal dielectric layer and those in a vertical groove can be engineered and understood in terms of energy level hybridization.

Considering that two-dimensional integrated circuit (IC) related feature sizes are now routinely at the deep sub-wavelength scale, possible visible light based far-field optical interrogation would be enabled through a better understanding of the local/near-field optical response [8,9,10] of metal-dielectric systems. While the related surface plasmon polaritons (SPP) and optical resonances have been much investigated for applications ranging from energy harvesting [11,12] to Raman spectroscopy [13,14,15] and biosensors [16], the present study seeks to extend the domain of application to IC diagnostics, such as feature size variation. We study the plasmonic characteristics relevant to confined geometries and the modulation of the absorption features that may be observed, *e.g.*, due to slight discrepancy in intended lithographic design. The interaction as well as the coupling between the SPPs originating from different underlying geometries, *e.g.*, vertical *vs.* horizontal modes, are also probed in detail, with respect to the intrinsic electric and magnetic fields.

Foundational to this work, SPP modes at metal /dielectric (M/D) and metal/dielectric/metal (M/D/M) interfaces [17,18] indicating enhanced absorption in deeply sub-wavelength grooves [19] and structures such as metal nanocubes with dielectric spacers [20,21,22] have been previously studied. The resonances in a vertical metal slit [19,23,24,25] as well as the horizontal thin dielectric spacer were probed [20,21,22,26,27,28,29,30], *e.g.,* the SPP modes in a M/D/M cavity were characterized through Fabry-Pérot (F-P) resonances fulfilling the condition: $\beta \cdot l$ ~ an integer multiple of $\pi/2$, with β ($= 2\pi/\lambda_{spp}$), where λ_{spp} is the effective wavelength, *i.e.,* the ratio of the free space light wavelength (λ_0) to the effective refractive index: $n_{eff} = \lambda_0/\lambda_{spp}$, at a given length scale (l). Moreover, the coupling between localized/cavity SPP modes and propagating surface SPP modes associated with periodic gratings was evaluated [30,31,32,33], with observed energy splitting. Such features and aspects may be used in design [20,21,22,26,27] as well as diagnostics.

Here, we probe the coupling effects related to localized/cavity SPP interactions in non-planar geometries. Such interactions are studied with respect to a grating-like background, with specific superimposed structures, constituted from both metal (M) and dielectric (D). A representative assembly, with incident illumination shown, is depicted in Figure2. 1(a), as Schematic of a metal grating on the top of dielectric spacer (chosen to be SiO_2) and metal (Ag) substrate, with normally incident p-polarized light. The model system is constituted from a horizontal M/D/M cavity in addition to a vertical Metal/Air/Metal (M/A/M) cavity. Such a model was chosen to correspond, for example, to possible topology of metal layers in an IC configuration, where the A and D may be representative of two different dielectrics.

The two confined SPP modes in M/A/M groove and the M/D/M horizontal cavity may be characterized by respective wave propagation constants (β) and pertinent length scales, as of the F-P kind. Relevant geometrical parameters that were used to tune the SPP related absorption characteristics are the (i) length of the metal cavity: w, (ii) groove width: g, (iii) the periodicity: p ($= w + g$), (iv) the height of the grating: h, as well as the (v) the dielectric spacer thickness: t. The formed SPP modes and their interactions were then probed, through monitoring the variation of the absorption spectra as a function of such tuning. For instance, a SPP mode in a M/A/M groove is excited when $\beta_{MAM} \cdot h \approx n\pi/2$. Similarly, a SPP mode in a M/D/M cavity would be excited when $\beta_{MDM} \cdot w \approx m\pi$. The n and m are odd integers corresponding to constructive interference [19,20].

The relevant computational simulations to obtain insights related to the metal-dielectric geometries were done using COMSOL®. The configuration for the simulation is shown in Figure2. 1 (b), where the simulation unit cell (with periodic boundaries – red vertical lines), indicating the metal/dielectric/metal (M/D/M) as well as the metal/air/metal (M/A/M) constituents. The geometrical parameters studied include the length of the metal cavity (w), groove width (g), periodicity (p) = w + g, height of the grating (h), and the dielectric spacer thickness (t). The two ports (port 1: input, port 2: output) were used for the simulations. The mesh size was in the range of 0.1 nm – 40 nm, and the corners were rounded out with ~ 1 nm radius. The light (p-polarized) is incident normal to the sample surface, with incident wavelength (λ_0) in the range of 400 nm to 800 nm. The mismatch between the confined M/D/M or the M/A/M mode and propagating guided modes would be relevant at higher energies, compared to the energies (< 3 eV) considered in this work. For instance, an M/D interface guided mode does not play a major role with small gap widths, say < 50 nm; instead, F-P like cavity modes dominate and will be studied here.

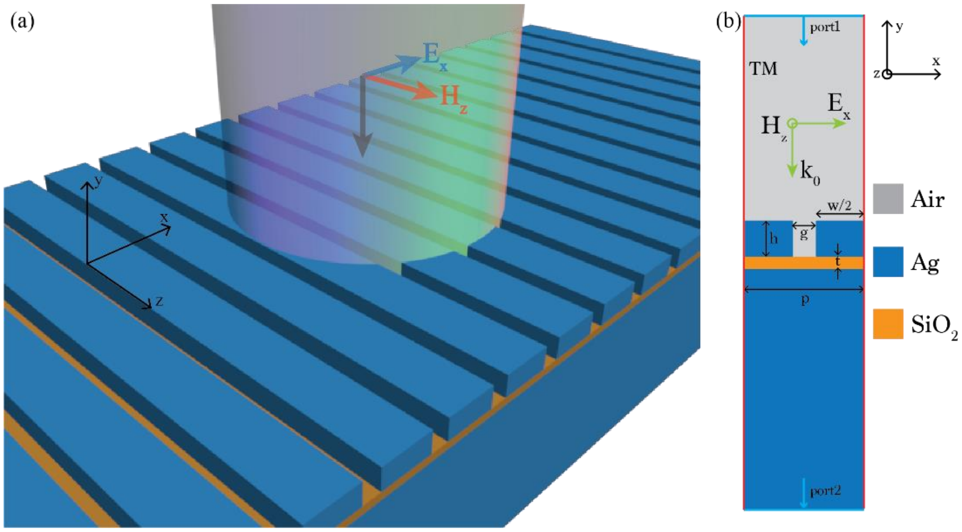

Figure2. 1**(a)** Schematic of a metal grating on the top of dielectric spacer (chosen to be SiO_2) and metal (Ag) substrate, with normally incident p-polarized light. **(b)** The configuration of the simulation unit cell

SPP induced absorption peaks of metallic grating with dielectric spacer

We first investigate the influence of the dielectric spacer in the M/D/M constituent, with respect to the absorption spectra and related mode structure. For metallic grating with subwavelength periodicity, significant absorption may occur under normally incident p-polarized light due to SPP excitation inside the groove. With small slit widths in the metallic grating, the SPP mode excited on the groove surface can be made to satisfy the resonance condition $\beta \cdot h \approx \pi/2$ [19]. The initial choice of parameters, i.e., $p = 200$ nm, $g = 40$ nm, $h = 40$nm, $t = 5$nm, were in the range achievable through commercial lithography, as deployed in IC fabrication. The metal was chosen to be silver (Ag) and the dielectric (D) was SiO_2. The absorption spectra, obtained from the simulations, are plotted in Figure2. 2(a), for $t = 0$ nm and $t = 5$ nm, *i.e.,* in the latter case, with an additional dielectric spacer layer in between the Ag grating on the top and the Ag substrate, on the bottom. In detail, the Absorption (A) spectra of Ag grating with ($t = 5$ nm, orange dotted line) and without ($t = 0$ nm, blue solid line) SiO_2 dielectric layer spacer, with $p = 200$ nm, $h = 40$ nm and $g = 40$ nm. For the labeled absorption peaks in Figure2. 2 (a), the magnitude of the out-of-plane magnetic field are plotted for structure with dielectric spacer in Figure2. 2 **(b)** E ~ 1.62 eV: peak 1, Figure2. 2 **(c)** E ~ 2.15 eV: peak 2, and Figure2. 2 **(d)** E ~ 2.57 eV: peak 3. The magnitude of the magnetic field is indicated at the right of the figure. The dielectric constant of the Ag (= ε_m) was estimated from a Lorentz model: $\varepsilon_m(\omega) = 1+\sum_n\{\varepsilon_n/[a_n(i\omega)^2-b_n(i\omega)+c_n]\}$, where ε_n is the resonance strength, a_n, b_n and c_n are fitted coefficients [30]. The dielectric constant of SiO_2 (= ε_d) was determined through a Sellmeier type equation [34],: $\varepsilon_d = 1+\sum_{i=1,2,3}[(B_i\lambda^2)/(\lambda^2-C_i)]$. The absorption $A = 1-R-T$, where R and T are reflectance and transmittance extracted from two ports at the top and bottom boundaries – see the simulation setup in Figure2. 1 (b). The $T = 0$ since there is negligible transmittance for Ag substrate (of thickness > 100 nm) in the visible wavelength range.

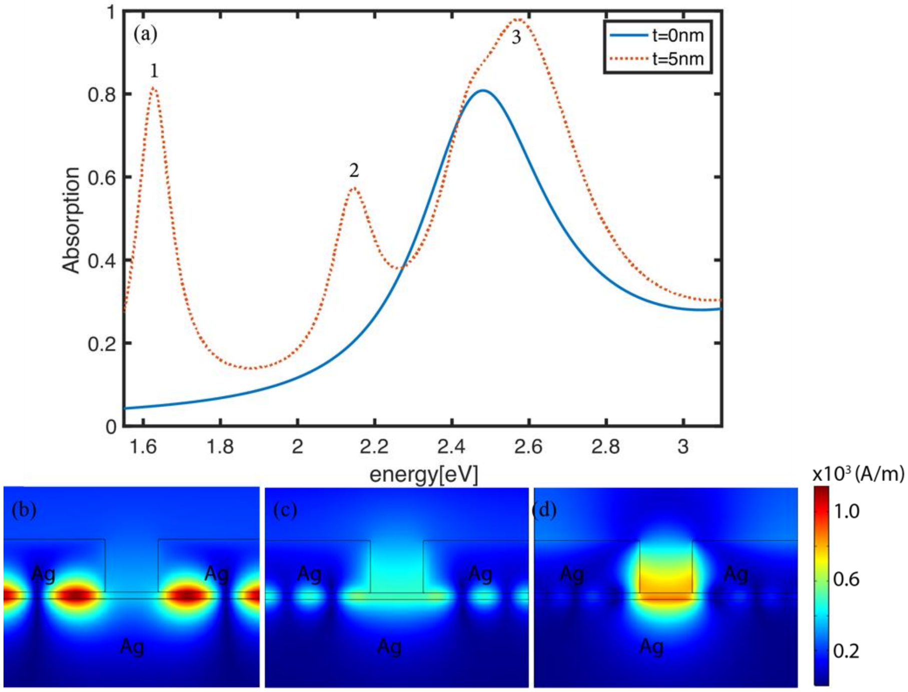

Figure2. 2**(a)** Absorption (A) spectra of Ag grating with and without dielectric layer spacer. The out-of-plane magnetic fields are plotted for **(b)** E ~ 1.62 eV: peak 1, **(c)** E ~ 2.15 eV: peak 2, and **(d)** E ~ 2.57 eV: peak 3.

An absorption spectrum with more delineated peaks was observed for the structure with dielectric spacer (M/D/M) – dotted line in Figure2. 2 (a), in comparison to that seen on a grooved Ag surface (solid line in Figure2. 2 (a)) when the spacer was absent. An absorption peak observed at ~ 2.48 eV was ascribed to F-P like SPP resonances in the vertical M/A/M groove, with the resonance condition inferred through:

$$\beta_{MAM} \cdot h + \phi / 2 \approx n\pi / 2 \tag{2.1}$$

Here, ϕ denotes the reflection phase change (in radians) at the bottom of the groove and may be obtained numerically from the full field simulation [20,35,36]. The β_{MAM} was estimated through using the following relations [19]:

$$\tan\left(\zeta g / 2\right) \approx -i\eta / \varepsilon_m \zeta \tag{2.2a}$$

$$\zeta = \left(k_0^2 - \beta_{MAM}^2\right)^{1/2} \tag{2.2b}$$

$$\eta = \left(\varepsilon_m k_0^2 - \beta_{MAM}^2\right)^{1/2} \tag{2.2c}$$

From E = 2.48 eV, we deduce the k_0 (= $E/\hbar c$ = $2\pi/\lambda_0$). Subsequently, we estimate: β_{MAM} = 20.8 μm^{-1} with $n_{eff} = \lambda_0\beta_{MAM}/2\pi$ = 1.65 and ϕ = 1.1 from simulations. Eq. (1.1) may not be exactly satisfied, due to the scattering around the corner of the grating and the SPP propagating loss inside the structure.

The use of a thin dielectric spacer layer between the grating and the substrate can support SPP in the related M/D/M structure, with an associated resonance condition:

$$\beta_{MDM} \cdot w + \delta \approx m\pi \tag{2.3}$$

Here, δ (in radians) was the phase difference between the right and left propagating SPP modes in M/D/M horizontal cavity, and is directly obtained from numerical simulation [20,35,36].

The absorption peaks essentially arise from the energy stored in the respective resonances associated with the M/A/M and the M/D/M geometries. While the peak, in the absence of a dielectric layer, is related predominantly to an M/A/M resonance, in contrast, peak 3 (with a dielectric layer present) arises from the coupling of modes comprising both M/A/M and M/D/M resonances. In the latter case, *e.g.*, for the peak ~ 2.57 eV, we estimate: $\beta_{MAM} = 24.5\ \mu\text{m}^{-1}$ with $n_{eff} = 1.9$ and $\phi = 0.95$ from the simulations. It is relevant to note the variation in β_{MAM} as a function of the added dielectric spacer. There are additional resonances specific to the M/D/M geometry, with F-P like character ascribed to the absorption peaks at 1.62 eV, 2.15 eV, and 2.57 eV. The magnetic field profiles are indicated at the bottom of Figure2. 2, for each of these peaks. However, the field profile related to E ~ 2.57 eV, seems to be different in character, compared to the profiles related to peaks 1 and 2, with finite t. As the t is much smaller than λ_0, the β_{MDM} of the fundamental guided mode in the M/D/M structure was determined through the following set of relations [18]:

$$\tan\left(k_d t\right) = 2\varepsilon_d \varepsilon_m k_d k_m / \left(\varepsilon_m^2 k_d^2 - \varepsilon_d^2 k_m^2\right) \tag{2.4a}$$

$$k_d = \left(\varepsilon_d k_0^2 - \beta_{MDM}^2\right)^{1/2} \tag{2.4b}$$

$$k_m = \left(\beta_{MDM}^2 - \varepsilon_m k_0^2\right)^{1/2} \tag{2.4c}$$

The respective values of the $\beta_{MDM} = 50.6\ \mu\text{m}^{-1}$ (for peak 1 at 1.62 eV), $= 85\ \mu\text{m}^{-1}$ (for peak 2 at 2.15 eV) and $= 135\ \mu\text{m}^{-1}$ (for peak 3 at 2.57 eV). From simulations, it was observed that $\delta \sim 2$ (at 1.62 eV), ~ 2.6 (at 2.15 eV) and ~ 0.9 (at 2.57 eV). Consequently, with w = 160 nm, $m \sim 3$ (peak 1), $m \sim 5$ (peak 2) and $m \sim 7$ (peak 3) in Eq. (1.3) – all with reference to Figure2. 2 (b) - 2(d), respectively. The absorption peak 3 is enhanced with the introduced dielectric thin film layer and is to be compared with the relatively broad absorption peak at E ~ 2.48 eV, for the Ag grating without the dielectric spacer. Further, the broadening and energy shifting of the respective absorption peaks may be indicative of coupling between the M/A/M and M/D/M SPP modes. For greater understanding of such coupling, further variation in the grating geometry was considered.

Investigating absorption with respect to grating groove width

The air gap width (g) was varied, at a fixed p (of 200 nm, as previously stated) to investigate possible M/A/M - M/D/M mode coupling. Figure2. 3(a) compares the Absorption (A) spectra for g = 40 nm (blue solid line), with absorption peaks (1, 2, and 3) and g = 20 nm (orange dotted line), with absorption peaks (a, b, and c). For the smaller g, there is a redshift of the absorption peaks as the horizontal M/D/M resonator length, w, is longer implying a smaller β_{MDM} required to match the constancy of the $\beta_{MDM} \cdot w$ product. Moreover, there are two clear absorption features - peaks (b) and (c) in Figure2. 3 (a) observed at E = 2.33 eV and E = 2.44 eV. From Eqs. 2(a)- 2(c), we obtain β_{MDM} = 103.3 μm^{-1} – for peak (b) at 2.33 eV, and = 117.5 μm^{-1} – for peak (c) at 2.44 eV. With a corresponding $\delta \sim 2.8$, obtained from simulations, $m \sim 7$ in Eq. (3). Additionally, we obtain β_{MAM} = 26 μm^{-1}, and $\delta \sim 0.9$, with correspondence to Eq. (1) and yielding a $n \sim 1$, related to the M/A/M SPP resonance.

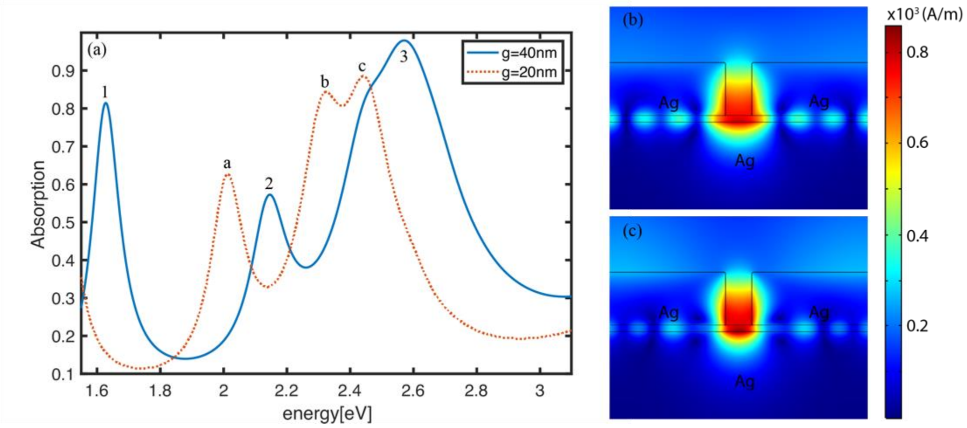

Figure2. 3**(a)** Absorption (A) spectra for g = 40 nm and g = 20 nm. The magnitude of the out-of-plane magnetic field at **(b)** E ~ 2.33 eV, and the higher energy peak **(c)** E ~ 2.44 eV.

Consequently, we conclude that the SPP resonance modes supported by the M/A/M vertical groove and horizontal M/D/M cavity resonator both contribute to the two absorption features – related to peaks (b) and (c) in Figure2. 3 (a), as plotted by the magnitude of the out-of-plane magnetic field are plotted for the lower energy peak Figure2. 3 **(b)** E ~ 2.33 eV, and the higher energy peak Figure2. 3 **(c)** E ~ 2.44 eV. The magnitude of the magnetic field is indicated at the right. The field profiles corresponding to the peak features are plotted in the corresponding Figure2. 3 (b) and 3(c) and show enhanced magnetic field in both groove and dielectric spacer, but differ in detailed distribution, *e.g.,* there seems to be a greater spread of energy in the case of Figure2. 3 (c). For *g* varying in the range of 5 nm to 50 nm, and a fixed *w* of 180 nm, the absorption spectra are compared in Figure2. 4(a), with an aim of understanding the origin of the two peaks. In Figure2. 4 (a), we showed that the variation of the absorption (A) spectra as a function of the groove width (g) in the range of 5 nm (bottom) to 50 nm (top). The M/D/M cavity length (w) is fixed at 180 nm, and the groove height (h) at 40 nm, with t = 5 nm. The circles and the triangles represent the high and low energy modes inside the vertical groove. The absorption peaks labeled by short black lines, on the left, are related to F-P like SPP resonances in the horizontal M/D/M resonator satisfying the resonance condition $\beta_{\mathrm{MDM}} \cdot w \approx 5\pi$, indicates an energy gap. The redshift of the lower energy peaks (~ 2 eV, labeled by short black lines) is hypothesized as due to the interaction of the magnetic moments between two M/D/M cavities on either side of the groove, and will be discussed later in Section 4.

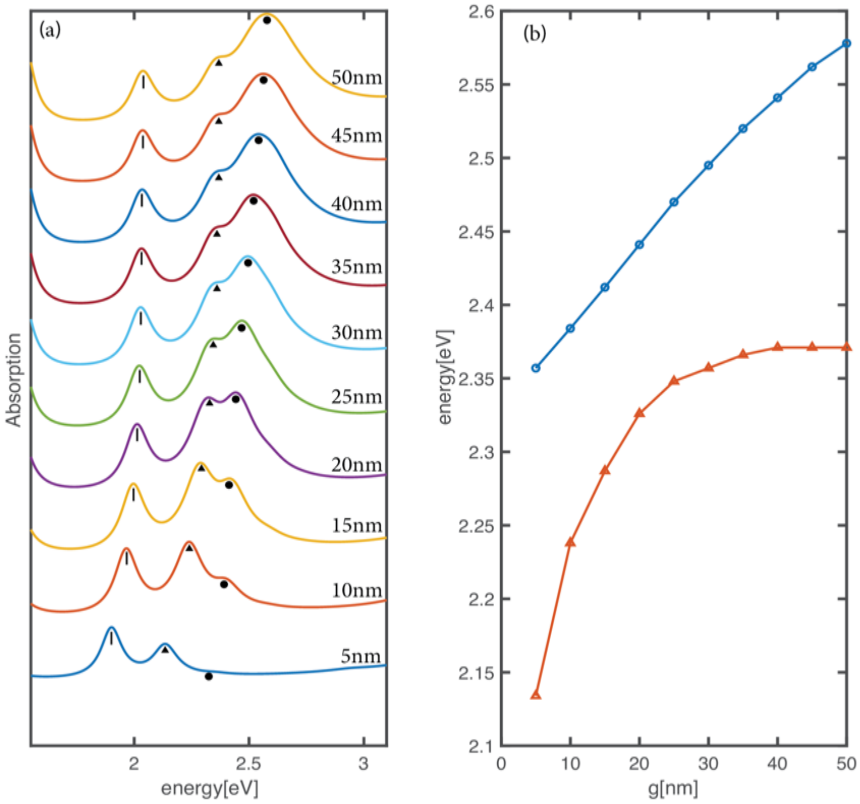

Figure2. 4**(a)** The variation of the absorption (A) spectra as a function of the groove width (g) **(b)** A plot of the high and low energy modes, from **(a)** indicates an energy gap.

For the higher energy features (2.1 eV – 2.6 eV), it was seen - from Figure2. 4 (a) that the high (/low) energy mode has a larger amplitude for large (/small) *g*. The respective high and low energy resonance energies are plotted in Figure2. 4 (b) as a function of the *g*, showing an energy gap. These two resonance peaks may be revealing of energy hybridization and splitting of coupled SPP modes originating from the M/A/M groove and M/D/M cavity. Here we choose three representative groove widths to illustrate: *g* = 10 nm (with the 2.24 eV and 2.38 eV, as the low and high energy modes), *g* = 20 nm (with the 2.33 eV and 2.44 eV, as the low and high energy modes) *g* = 50 nm (with the 2.37 eV and 2.58 eV, as the low and high energy modes). In the dielectric layer, the magnitude of E_x is plotted in Figure2. 5(b)-5(d), where we observe that two modes have distinct field profiles – the higher energy mode is mostly situated inside the groove while the lower energy mode is localized to the groove edge. In Figure2. 5, the horizontal electric field (E_x) profiles along the dotted yellow line, are plotted for **(b)** g = 10 nm, **(c)** g = 20 nm, and **(d)** g = 40 nm, for the respective lower and higher energy modes, taken from Figure2. 4 (a). The electric fields may be related to the surface current at the bottom of the groove. The black dashed lines in **(b-d)** indicate the position of the groove walls.

A discrimination of the difference between the two resonance modes inside the groove may be considered on the basis of the horizontal E_x components along the dielectric. the higher energy mode dominates *over* the lower energy mode *inside* the groove. Specifically, the area under the horizontal electric field (E_x) – spatial variation (*position*) curve may be related to a potential difference at the bottom of the groove and was found to increase with increased gap width (g). The potential difference (or the related E_x) may be related to a surface current. It was deduced that the high energy mode is dominant at the bottom of the groove, while the lower energy mode is dominant at the groove edge due to the interaction of SPPs.

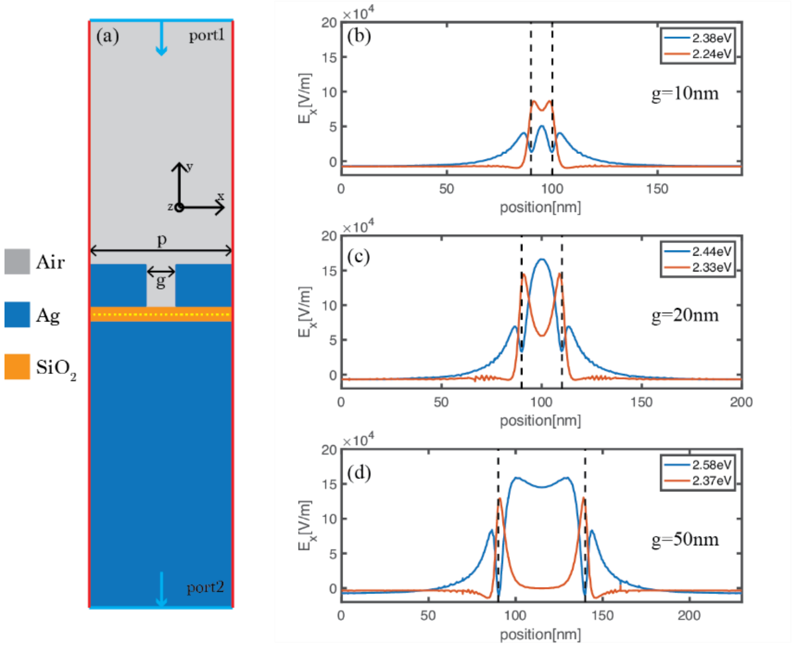

Figure2. 5**(a)** The horizontal electric field (E_x) profiles, plotted for **(b)** g = 10 nm, **(c)** g = 20 nm, and **(d)** g = 40 nm, for the respective lower and higher energy modes.

The hybridization of cavity F-P like SPP modes

To further explain the absorption peak and dispersion ~ 2.4 eV, in Figure2. 4 (a), the metallic grating was modeled as incorporating an F-P like SPP resonance: (a) in the vertical M/A/M groove, and (b) in horizontal M/D/M cavity and included the subsequent possibility of coupling between the modes related to (a) and (b).

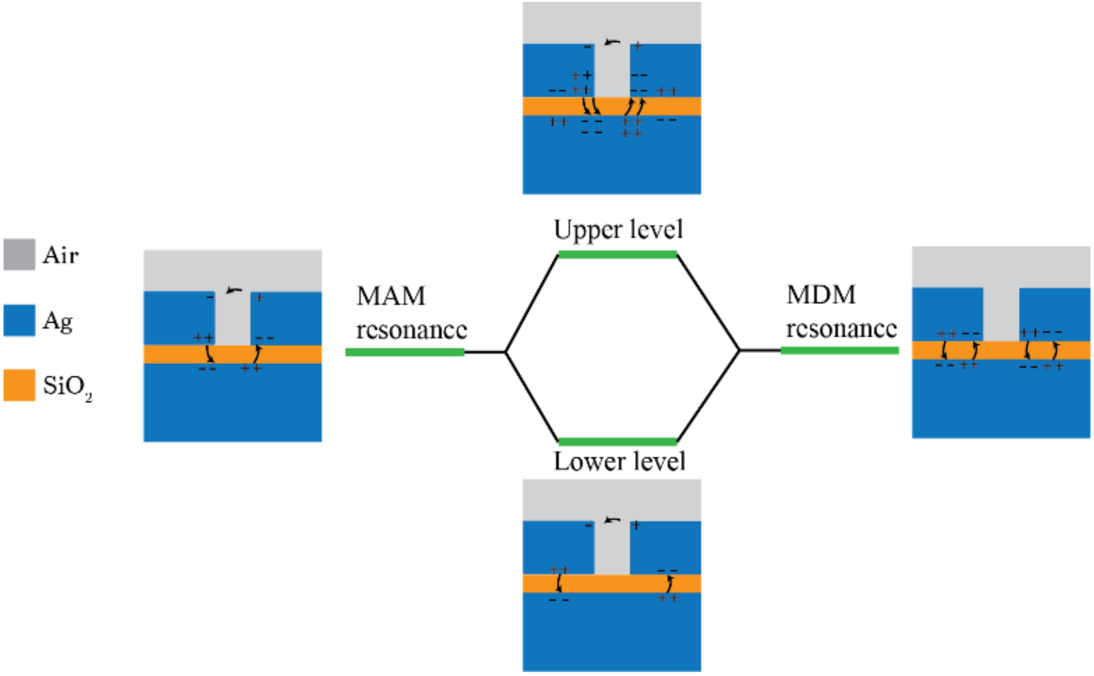

Figure2. 6 The generation of hybrid modes mediated by the interaction of the M/A/M with the M/D/M energy levels.

The energy level interaction and subsequent energy gap formation, as in Figure2. 4 (b), is indicative of energy level hybridization. Consequently, we hypothesize that the individual M/A/M and M/D/M related modes (in the groove and dielectric spacer, respectively) may interact with each other and generate the double peaked structure near ~ 2.4 eV in Figure2. 4 (a). The interaction is schematically indicated in Figure2. 6, where the generation of hybrid modes mediated by the interaction of the M/A/M with the M/D/M energy levels. The groove M/A/M mode is coupled to the M/D/M resonance mode, yielding local surface charges and currents (depicted by the black arrows) and related to the electric field profiles of Figure2. 5. The width of the hybridized energy gap would be proportional to the extent of coupling between the modes and will be discussed subsequently. From a physical standpoint, the surface charges due to the SPP couple together near the groove. The hybrid mode is constituted from larger surface currents near the groove bottom at higher energies, (blue E_x curves in Figure2. 5 (b) – 5(d)) as well as the enhanced field amplitude at/near the side wall/s of the groove.

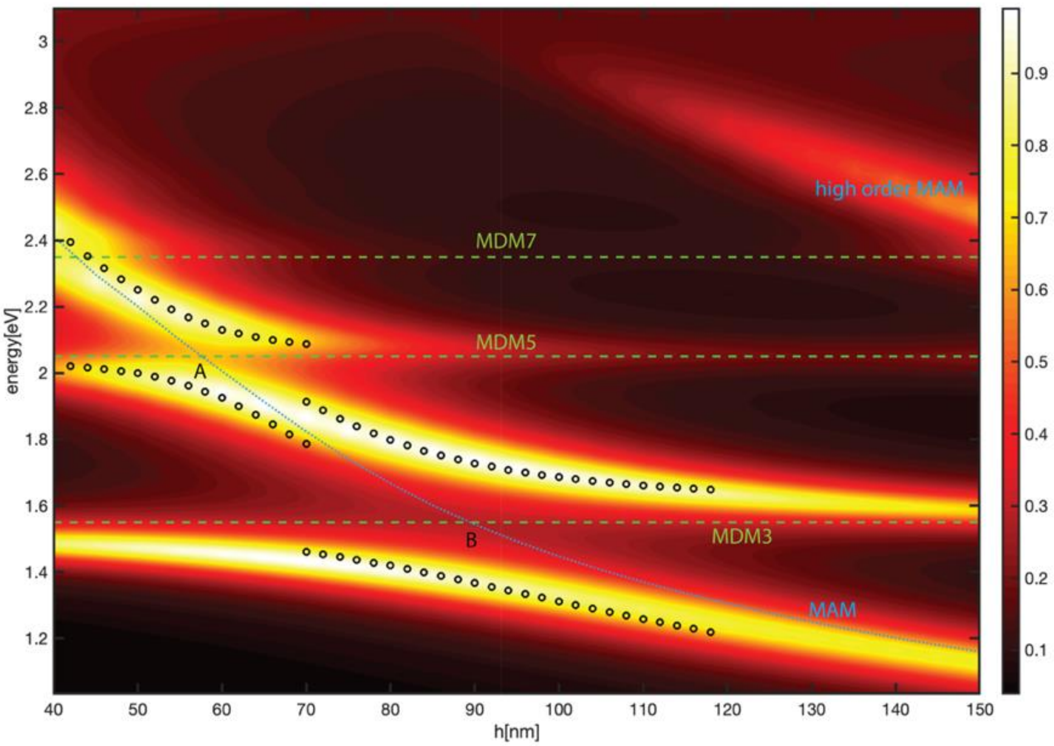

Figure2. 7 The coupling of the M/A/M modes with the M/D/M leads to energy level interaction and gap formation as seen in the absorption spectra as a function of the grating height (h).

The energy splitting, related to the mode coupling, and resultant absorption may be tuned by modifying the grating geometry parameters. While the M/A/M resonance mainly depends on *h* as well as the *g* (changing β_{MAM}), changing *w* and *t* can modify the M/D/M resonances. If the *p* is close to the incident photon wavelength, long range propagating SPP modes would also play a role [31]. With such a goal of tuning the energy splitting, we varied the *h* to investigate the influences on the hybridization. The M/D/M mode resonance is unaltered as the *w* and *t* are not changed. The overall effects are indicated in Figure2. 7, indicating the coupling between M/A/M and M/D/M related SPP modes. In Figure2. 7, the coupling of the M/A/M modes (characterized by Eq. (1)) with the M/D/M modes (characterized by Eq. (3)) leads to energy level interaction and gap formation as seen in the absorption spectra as a function of the grating height (h). The numbers after the MDM refer to the m in Eq. (3). Here, the g = 20 nm, while p = 200 nm, w = 180 nm, and t = 5 nm. The incident photon wavelength is varied from 400 nm to 1200 nm. The magnitude of the absorption coefficient is indicated on the right. For instance, the energy level hybridization at *h* ~ 55 nm (at 2.05 eV): A in Figure2. 7, corresponding to *m* ~ 5, and *h* ~ 90 nm (at 1.55 eV): B in Figure2. 7, corresponding to *m* ~ 3, due to interaction between the M/A/M (with *n* ~ 1) and the respective M/D/M modes is clearly observed. Higher order M/A/M F-P resonance mode (with *n* ~ 3) at ~ 2.5 eV, are also seen at larger *h* (at values larger than 100 nm). The magnitude of the hybridization energy gap is directly proportional to the coupling strength of the two SPP modes. To describe the coupling behavior, a relevant Hamiltonian (*H*) for the resonance structure may be posited to be:

$$H = \begin{pmatrix} E_{MDM} & V \\ V & E_{MAM} \end{pmatrix} \qquad (2.5)$$

Here, the E_{MDM} and E_{MAM} are the energy of M/D/M modes and M/A/M modes, and V denotes the coupling between these two SPP F-P like modes. We obtained the eigenvalues of the energy from Eq. (1.5) to be:

$$E_{+/-} = \frac{1}{2}\left[\left(E_{MAM} + E_{MDM} \right) \pm \sqrt{\left(E_{MAM} + E_{MDM} \right)^2 + 4V^2} \right] \qquad (2.6)$$

The E_{MAM} and the E_{MDM} are the respective energies of the MAM and MDM modes obtained through simulation. For different grating heights (h), the bare resonance energies are plotted in Figure2. 7. The upper and lower coupled mode energies (E_+ and E_-, respectively) are estimated and labeled by black circles in Figure2. 7, with a fitted coupling parameter V ~ 0.1 eV and ~ 0.18 eV at points A and B, respectively, through a graphical fit using MATLAB®. Such a value of V is in close agreement with observations in literature[37] , *e.g.*, involving coupling between a surface plasmon mode and a F-P resonance mode[38], or related to the coupling across a silica spacer layer between a MoS_2 sheet and a periodic array of metal nanogrooves[39]. Consequently, our computationally predicted upper and lower energy bounds, and related V are in good agreement with those in literature and correspond well to the interaction between the associated M/A/M and M/D/M resonances.

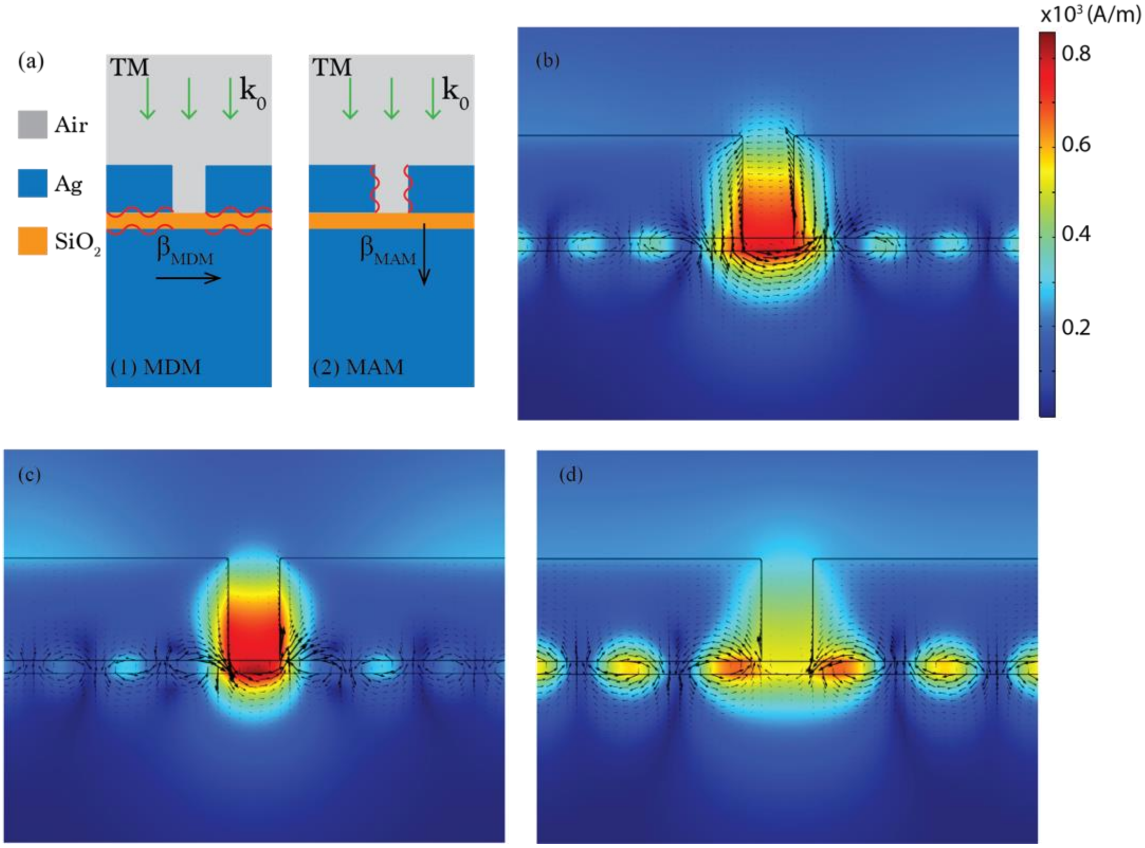

Figure2. 8**(a)** An overall summary of the M/D/M and M/A/M modes with related SPPs. The magnitude of the out-of-plane magnetic field and simulated current flow are plotted for peaks **(b)** E ~ 2.33 eV, **(c)** E ~ 2.44 eV **(d)** E ~ 2.01 eV.

The notion of mode hybridization implies both symmetric (attractive) – lower energy, and anti-symmetric (repulsive) – higher energy interactions and may be used to yield absorption bands of larger bandwidth. In Figure2. 8, we show an overall summary of the horizontal M/D/M and vertical M/A/M modes with related SPPs. The magnitude of the out-of-plane magnetic field are plotted for peaks in Figure2. 8 **(b)** E ~ 2.33 eV, Figure2. 8 **(c)** E ~ 2.44 eV – from Figure2. 8 (a), as well as for the lower energy modes, i.e., Figure2. 8 **(d)** E ~ 2.01 eV. The current flow directions are related to induced magnetic moments and their related interactions. A higher degree of interaction leads to a larger energy gap and broader energy gap. The magnitude of the magnetic field is indicated at the right. Such interactions may also be considered in terms of current loops with associated magnetic moments: Figure2. 8 (b)- (d). Near the side walls of the groove, the two current loops in the M/D/M constituent have the same direction, implying greater interaction related to higher energies, and a larger β_{MDM}. Such interactions would be enhanced with decreasing g. The shift of the energy resonances, as seen in Figure2. 4 (a) is now understood on a deeper physical basis.

The novelty of our work is related to (a) the detailed study of possible interactions between two types of confined surface plasmon polariton modes, as may be ascribed to Fabry-Perot resonances, with a motivation related to (b) applying the related findings to confined geometries as may be found, e.g., in integrated circuit layouts. While mode interaction would inevitably yield energy splitting, e.g., as in the interaction between a localized mode and delocalized mode[31], here the nature of the studied interacting modes is different.

Moreover, plasmonic considerations may allow the determination of variations in critical dimensions through optical interrogation instead of laborious and destructive SEM (scanning electron microscopy) or related FIB (focused-ion-beam) based probing. Given the nanoscale features of modern electronic devices, plasmonic characteristics, as related for example to absorption features may now be used. The main advantages would then be the use of non-destructive techniques coupled with the use of visible light, and spectroscopic characterization. The validity of the proposed methodology may be tested through experimentally varying the feature size (as indicated in the paper) through electron-beam lithography-based procedures (which may be probed through SEM) and observing the changes in the related absorption spectra.

Conclusions

In summary, the hybridization of SPP modes, e.g., between the vertical M/A/M groove SPP resonance mode and a horizontal M/D/M cavity SPP resonance mode, has been indicated. The F-P like M/A/M and M/D/M SPP modes could be tuned by a relevant geometry length scale and related to a particular propagation constant: β_{MAM} or β_{MDM}, through Eq. (1) and Eq. (3), respectively. Consequently, the mode coupling, and the resultant energy hybridization and energy gap could be engineered by the variation of geometrical parameters. Such mode interactions could be used to broaden the energy absorption spectra, as for energy harvesting [20,21,26]. The aspect of the multiple resonances and interactions brought about through both vertical and horizontal geometries in metal-dielectric (/air)-metal geometries would be of relevance to understanding optical interactions in circuit geometries and be of utility for diagnostics related to parameter variation in lithographic fabrication.

Acknowledgements

Chapter 2, in full, is a reprint of the material as it appears in Dong, Yongliang, and Prabhakar R. Bandaru. "Interaction and hybridization of orthogonal Fabry-Pérot like surface plasmon modes in metal-dielectric grating structures." *Optics express* 28.3 (2020): 3541-3551. The dissertation author was the primary investigator and author of this paper.

Chapter 3. Enhanced Graphene Surface Plasmonics through incorporation into Metallic nanostructures

Introduction

The phenomena related to surface plasmon polariton (SPP) resonances, based on the collective oscillation of carriers excited by incident electromagnetic (EM) waves, has been well explored at metal (negative refractive index: n_m)-dielectric (positive refractive index: n_d) interfaces [8,9]. The high sensitivity of the resonance to the refractive index difference (Dn), has resulted in the use of SPP-based phenomena for scientific insights into near-field EM interactions as well as technological applications, such as label-free diagnostics and sensing [16,40,41,42]. For instance, the manifestation of distinct SPP mode varieties [24,31,32], *e.g.*, in metallic nanogaps incorporating Fabry-Perot (F-P) resonances and the related peak splitting in the far field [44], enabling a larger spectral range has been previously considered. The magnitude of such interactions is determined by the geometry and material constituting the metal/dielectric/metal (MDM) gaps, of size less than the incident wavelength (l_0) [19]. Such gaps could be fabricated by lithography or through using the spaces between metallic nanocubes [19,20,21].

One aim of the present work was to bring forth the characteristic utility of low dimensional materials, such as graphene, integrated with such MDM gratings for the further modulation of F-P based SPP resonances [45,46,47,48,49,50,51]. The ability to vary the carrier density of graphene by orders of magnitude, through electronic gating [47] or chemical doping could be harnessed in this regard. For instance, with increased carrier density, the in-plane dielectric constant ($e_{||}$) of graphene may be made negative in the near-IR regime (with l_0 in the range of 0.7 µm to 1 µm) and helps support a graphene SPP (GrSPP) at the graphene/dielectric interface [47]. The formation of such a GrSPP has been previously verified through near field spectroscopy [47].

Here, we indicate the coupling of the GrSPP with F-P like MDM gap resonances, and their spectroscopic signature. To manifest and tune the GrSPP[48, 51], a carrier density in the range of 0.75×10^{14} cm^{-2} to 2×10^{14} cm^{-2} was chosen - implying a Fermi energy (m) in the range of 1 eV to 1.7 eV. While it has previously been shown that the m of the graphene could be tuned through using metal nanoparticles [52], the use of metallic material implies loss and it would be better to use graphene alone. Previous work on the modulation of the GrSPP through metallic gratings, considered the coupling of the localized resonances *via* the magnetic polaritons with the GrSPP, at larger wavelengths (l_0 ~ 10 mm) [53] as a function of grating geometry [54]. The influence of conformational changes of the graphene overlaid on metallic gratings on the GrSPP was revealed through a *red* shift in the absorption peak at l_0 ~ 3 mm, with m of the order of 0.3 eV [55], indicating a frequency dependency to the GrSPP phase shift [56]. Here, we propose the use of hexagonal boron nitride (hBN) to reduce wrinkles while promoting an ultra-flat, loosely bound configuration for the graphene [57]. Considering smaller l_0 values and higher m values, our models cover a much larger range of m of up to 1.7 eV and have observed blue shifts of the MDM SPP due to the presence of graphene. Moreover, the graphene is placed underneath the metal-dielectric-metal grating, for greater ease of fabrication. We also suggest a new application considering the GrSPP - MDM SPP interactions and related tunability, for sensor modality.

We have conducted finite-element frequency simulation by COMSOL®, for comparing both metal SPP and graphene SPP in the Ag/air/Ag grating – corresponding to the MDM configuration with graphene at the bottom, as shown in Figure3. 1(a). In practice, a graphene layer may be isolated, through etching it off the copper substrate, and subsequent placement of the layer through a wet transfer assisted transfer onto hBN placed on top of a Si/SiO_2 substrate. An MDM grating, with a defined periodicity (*p*), grating height (*h*), width (*w*), and gap width (*g*): set as the geometric parameters in the unit cell used for the simulation, shown in Figure3. 1 (b), could be fabricated on the graphene through electron-beam lithography-based procedures. It is also plausible, as indicated previously, that the gaps related to the MDM grating could be realized through using the spaces between metallic nanocubes, synthesized through chemical processing[19,20,21].

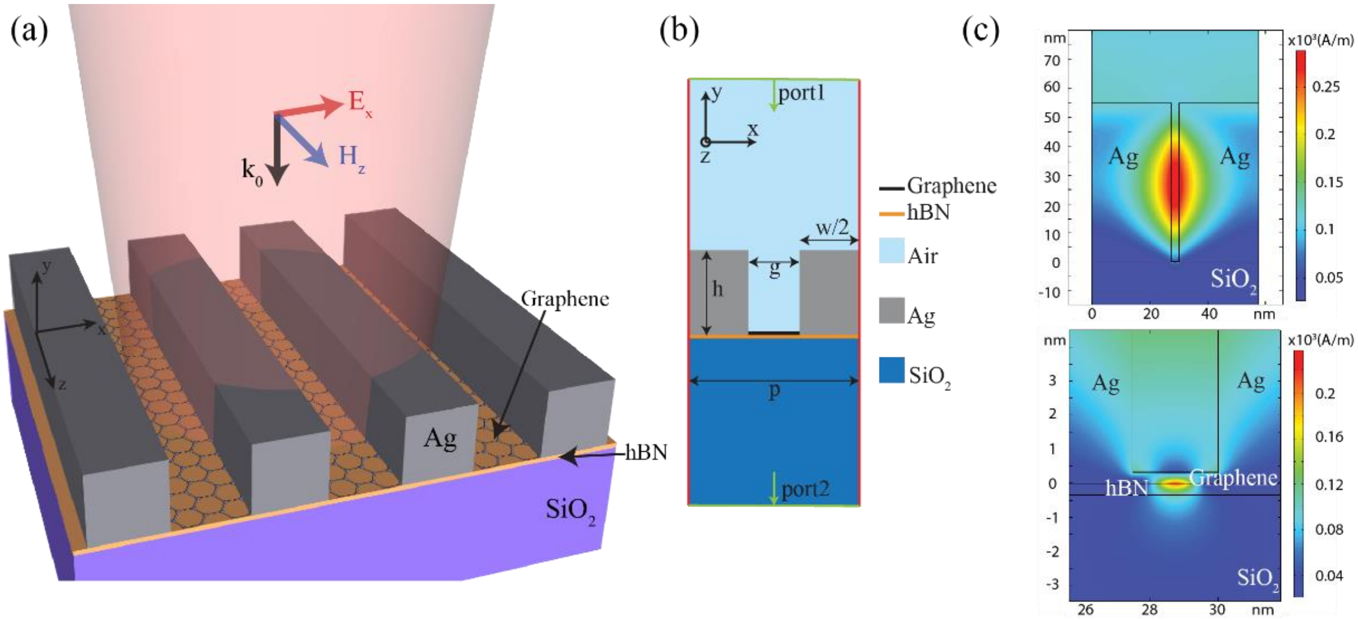

Figure3. 1(a) A schematic of the investigated substrate; (b) The unit cell used for the simulation; (c) The magnetic field magnitude for MDM SPP and GrSPP resonance.

The periodic unit cell for the simulation is indicated through a domain annotated in Figure3. 1 (b). The *top*(/*bottom*) indicates the input (/output) ports: 1 (/2), for the simulation. A *p*-polarized plane wave (with an electric field orientation in the *x-y* plane: $E_{x,y}$) is incident vertically and excites

F-P based MDM SPP modes and GrSPP modes within the thin vertical slit. Such an aspect is manifested, for instance, through the output magnetic field magnitude ($|H_z|$) as related to the resonances of F-P like MDM SPP (Figure3. 1 (c): top) and GrSPP (Figure3. 1 (c): bottom). A clear coupling and energy splitting between MDM F-P SPP and related Gr SPP was observed. The resultant modulation of the coupled resonance modes may be correlated to a change in the effective refractive index (Δn) of the graphene integrated MDM structure.

Resonances related to the metal-dielectric-metal (MDM) gaps

The occurrence of the SPP was investigated in terms of the geometrical parameters, related to the MDM geometry, as indicated in Figure3. 1 (b). For the metallic grating with subwavelength periodicity ($p \ll \lambda_0$), the SPP in the MDM gap is termed F-P *like* from fulfilling the resonance condition: $\beta_{\mathrm{MDM}} \cdot h \sim m\pi$, where β_{MDM} is the wavevector of the MDM SPP and m is an integer representing the order of the resonance. The unit cell is shown in Figure3. 2 (a), used for simulating the MDM SPP resonance, with the related SPP propagating along the vertical direction. Such a condition can be estimated by the MDM gap mode relations [44], with enhancement of the SPP resonance brought about by constructive interference inside the slit as indicated through the $|H_z|$ maximum at the slit center: Figure3. 1 (c): *top*). We had previously investigated the geometry dependence of the β_{MDM} and the related resonances [44]. Here, we indicate the resonance peaks obtained in the absorption spectrum of the grating structure.

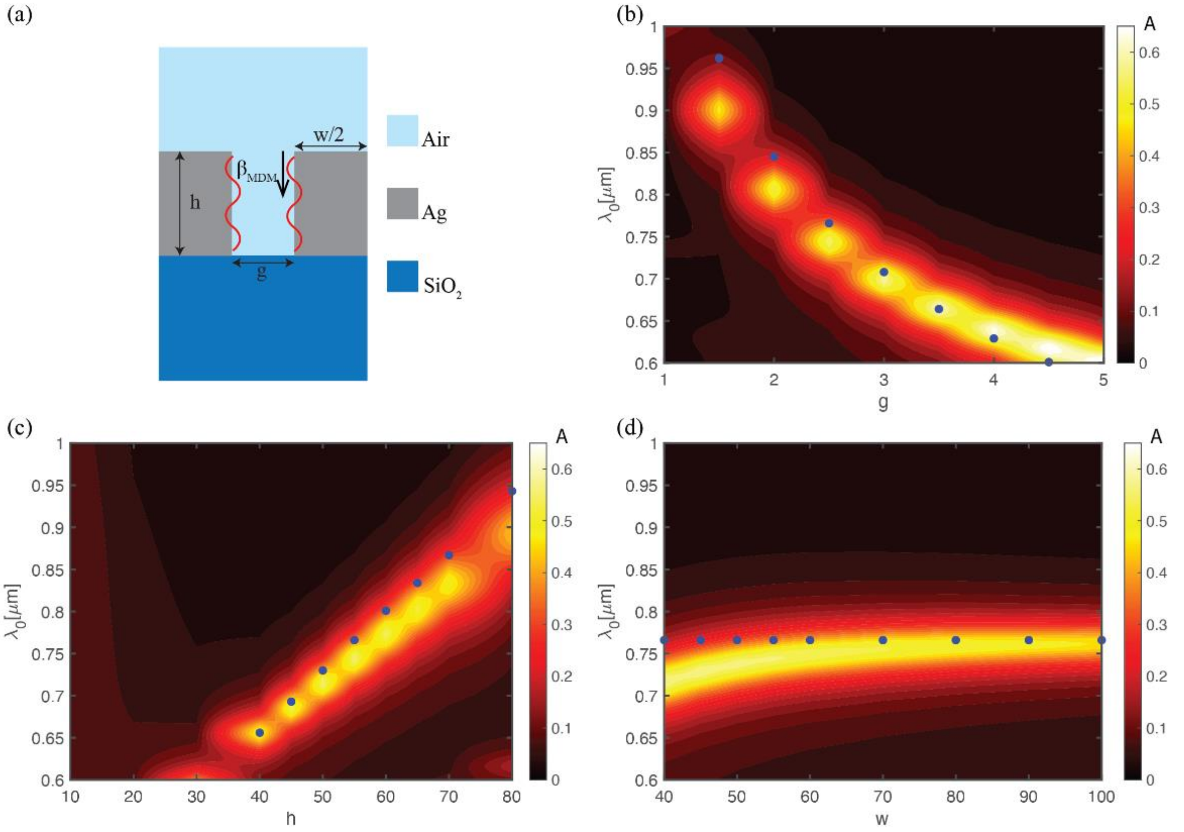

Figure3. 2(a) The unit cell, used for simulating the MDM SPP resonance. The variation of the absorption (A) as a function of the grating structure geometry, with (b) g; (c) h; and (d) w.

In Figure3. 2 (b) the spectral variation of the far field absorption (A) as a function of the grating width: *g*, is shown. The *h* and *w* were set at ~ 55 nm – a value corresponding to commercial Ag nanocube length scales (*e.g.*, from nanoComposix.com), which could support MDM F-P like resonances [20]. The resonance peak (blue dots) variation with *g*, considered in accord with the β_{MDM} dispersion indicated in Figure3. 3(a), is also shown.

The MDM F-P like SPP wave is excited by the TM incident light inducing resonances satisfying the condition: $\beta_{MDM} \cdot h \sim m\pi$, *m* is an integer representing the order of the resonance, shown as the blue dots in Figure3. 2 (b-d). Here β_{MDM} is the wavevector of MDM SPP wave (Ag/Air/Ag configuration), and may be calculated from the following equations:

$$\begin{aligned} &\tan\left(g\xi/2\right) \approx -i\varphi/\varepsilon_{Ag}\xi \\ &\xi = \sqrt{\left(2\pi/\lambda_0\right)^2 - \beta_{MDM}^2} \qquad (3.1) \\ &\varphi = \sqrt{\varepsilon_{Ag}\left(2\pi/\lambda_0\right)^2 - \beta_{MDM}^2} \end{aligned}$$

Where $\varepsilon_{\mathrm{Ag}}$ is the dielectric constant of Ag obtained from the Lorentz model.

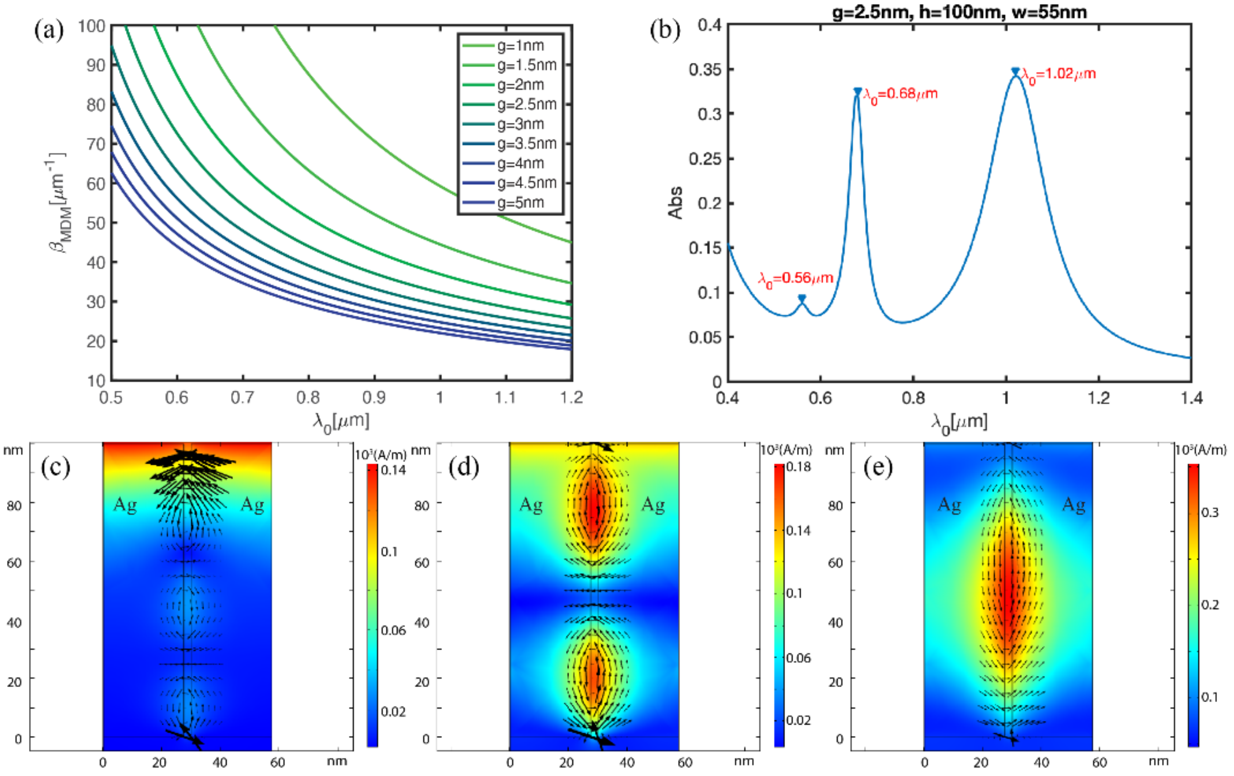

Figure3. 3(a) The dispersion relationship plot of MDM SPP resonance with different g. (b) The absorption spectra (c-d) the corresponding $|H_z|^2$ color map of each resonance peaks.

The obtained dispersion relationship (β_{MDM}-λ_0) for MDM F-P like SPP resonance is plotted for different *g and* shown in Figure3. 3 (a). To demonstrate the different orders of MDM F-P like resonances, an MDM structure with *h* = 100nm was chosen (*g* = 2.5nm, and *w* = 55nm Ag grating on top of SiO_2/Si substrate), showing three peaks in the absorption spectra (Figure3. 3 (b)). In an ideal F-P like resonance, the wave in the cavity is related to a standing wave interference with total $m\pi$ phase change. Such a resonance can be schematically represented by the magnitude of H_z at certain λ_0, in Figure3. 3 (c-e), showing the corresponding $|H_z|^2$ color map of each resonance peaks with the black arrows indicating the surface current flow. From Figure3. 3 (a) at g=2.5nm, β_{MDM}~32μm^{-1} at λ_0=1.02μm β_{MDM}~58μm^{-1} at λ_0=0.68μm and β_{MDM}~85μm^{-1} at λ_0=0.56μm. With h=100nm, the $\beta_{MDM}\cdot h$=3.2~1π at λ_0=1.02μm, $\beta_{MDM}\cdot h$=5.8~2π at λ_0=0.68μm and $\beta_{MDM}\cdot h$=8.5~3π at λ_0=0.56μm. The slight mismatch in second and third order resonances are due to the phase shift at the edge of the slit [44,67]. For instance, in Figure3. 3 (c), three resonance enhanced field nodes inside MDM gap attribute to resonance $\beta_{MDM}\cdot h$~3π, while the field and surface current flow near the top gap opening represent the F-P like SPP resonance phase mismatching.

It was seen that the peak shifts through reducing g (say, from 5 nm to 1 nm) substantially from ~ 0.6 μm to ~ 1 μm. A smaller g implies a shift to higher λ_0 and is associated with decreasing A due to the smaller MDM gap volume [44]. A higher h implies a shift to a smaller β_{MDM}/larger λ_0 : see Figure3. 2 (c) (the A as a function of h, with w = 55nm and g = 2.5nm) from $\beta_{MDM}\cdot h \sim m\pi$. The influence of the grating width (w) on the resonance shift, as indicated in Figure3. 2 (d) (the A as a function of w with h = 55nm, g = 2.5 nm), is less pronounced. The interference between adjacent MDM slits at reduced w may be expected to yield a blue shift.

The excitation of GrSPP resonances in confined single-layer graphene

Integrating graphene into the metallic grating adds a new *tunable* degree of freedom for further modulating SPP resonances. As is well known, the tuning of the graphene carrier density to vary the electrical conductivity coupled with the all-surface characteristic of the graphene enables specificity and sensitivity [45,46,47,48,49,50,51,52,58,59,60], that may be utilized for sensing applications. In our simulations, an atomically thin single layer graphene (SLG) of thickness t = 0.34 nm [61], *e.g.*, in the form of graphene nanoribbons (GNR) was placed at the bottom of the Ag grating constituted MDM gap, with an underlying layer of hBN: Figure3. 4(a) which shows the simulation unit cell incorporating the single layer graphene (SLG) overlaid on hBN on a SiO_2/Si substrate. The GrSPP propagates along the SLG surface. The hBN has been typically used for atomically smooth and ultra-flat graphene surfaces [57]. The MDM related barriers help for the confinement of GrSPP in the gap following its excitation by the *p*-polarized illumination.

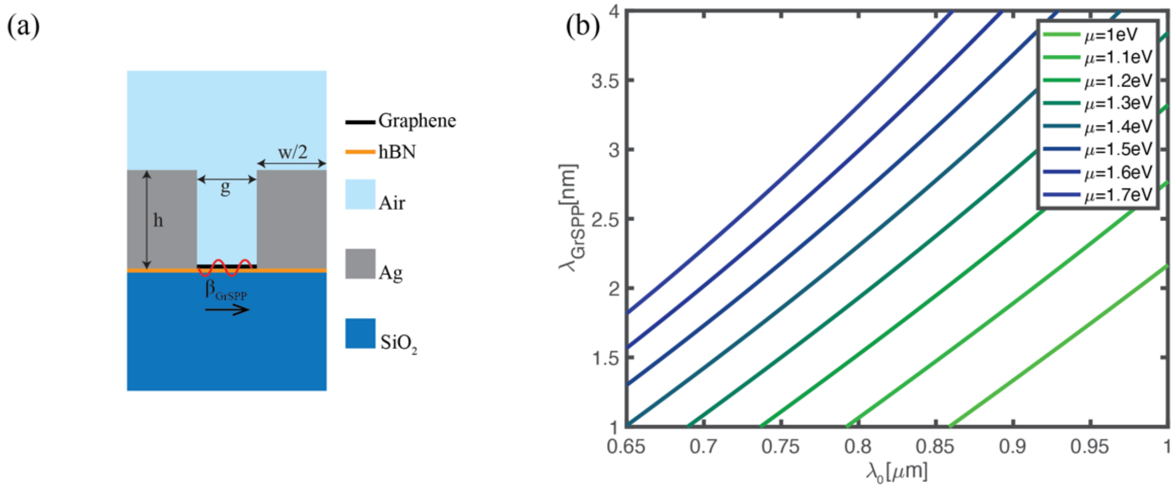

Figure3. 4(a) The simulation unit cell incorporating the SLG overlaid on hBN with GrSPP propagates along the SLG surface; (b) Estimation of graphene SPP dispersion relationship.

In this study, the carrier density of graphene was modulated over a range of 0.75×10^{14}cm^{-2} to 2×10^{14}cm^{-2}, with μ varying in the range of 1 eV to 1.7 eV (Figure3. 5 (a)), for tuning the GrSPP response in the near-IR. The carrier density of graphene may be tuned through an (i) applied voltage, or through (ii) chemical doping, as indicated in the introductory sections. For instance, a negative (/positive) gate voltage applied to the back of the Si substrate would decrease (/increase) the carrier density [62]. Alternately, the use of electron donor (/acceptor) molecules, e.g., aniline and tetrathiafulvalene: TTF) (/oxygen or tetracyanoethylene: TCNE) could increase (/decrease) the carrier density of the graphene. Such an aspect for manifesting the surface plasmons through modulations of the carrier density has been extensively indicated in literature [47]. Consequently, the graphene in-plane optical conductivity: $\sigma = \sigma_{intra} + \sigma_{inter}$; involves both *intra*-band and *inter*-band contributions from electron-phonon scattering and electronic energy level transitions, respectively and is indicated as a function of μ, through the following relations [58,59,60]:

$$\begin{aligned} \sigma_{\mathrm{int}ra} &= \frac{2ie^2 k_B T}{\hbar^2 \pi (\omega + i\Gamma)} \ln\left[2\cosh\left(\frac{\mu}{2k_B T}\right)\right] \\ \sigma_{\mathrm{int}er} &= \frac{e^2}{4\hbar}\left[\frac{1}{2} + \frac{1}{\pi}\tan^{-1}\left(\frac{\hbar\omega - 2\mu}{2k_B T}\right) - \frac{i}{2\pi}\ln\frac{(\hbar\omega - 2\mu)^2}{(\hbar\omega - 2\mu)^2 + (2k_B T)^2}\right] \end{aligned} \tag{3.2}$$

Here, e is the unit of elementary electronic charge, ω is the frequency of incident light ($\omega = 2\pi c/\lambda_0$), Γ is the charge carrier scattering rate of ~ 10 ps^{-1} [63] and T the temperature (300K) [60]. The in-plane dielectric constant $\varepsilon_{||}$ ($= 1 + i\sigma/\varepsilon_0 \omega t$) for SLG was obtained from a thin slab model [60]. The out-of-plane dielectric constant ($\varepsilon_{\perp}$) was assumed to be 6.9 as a constant since the charge oscillation is limited to the atomic plane [64]. The calculated real and imaginary parts of the $\varepsilon_{||}$ are plotted in the Figure3. 5 (b, c), over a range of μ from 1 eV to 1.7 eV.

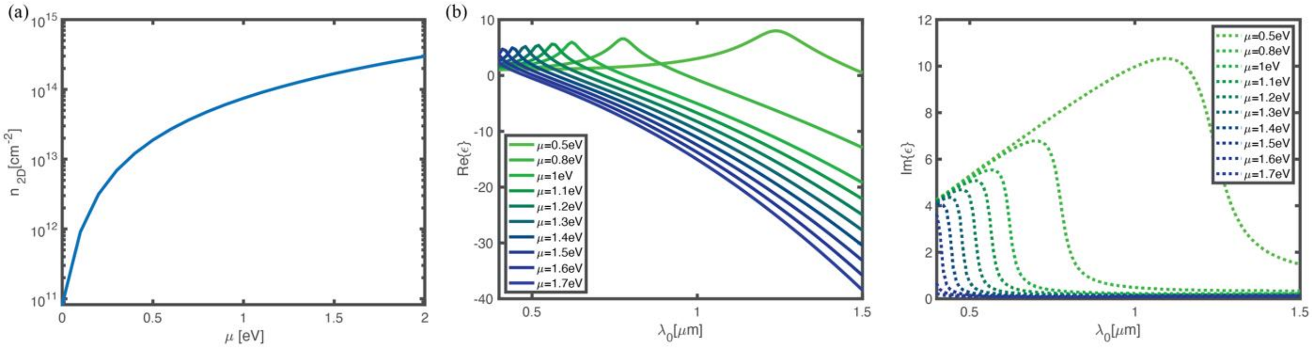

Figure3. 5(a) Calculated n_{2D} and it's corresponding μ. (b,c) The real and imaginary parts of in-plane graphene dielectric constant ($e_{||}$) with m of 0.5eV, 0.8eV and the range of 1 eV to 1.7 eV.

The μ of graphene can be modulated through the carrier density modulation via electronic gating [62] or charge carrier transfers [47]. The relationship between graphene carrier density (n_{2D}) and Fermi level can be calculated as [68]:

$$n_{2D} = \frac{2}{\pi}\left(\frac{k_B T}{\hbar v_F}\right)^2 F_1\left(\frac{\mu}{k_B T}\right) \qquad (3.3)$$

Where the F_1 is Fermi-Dirac integral and v_F is Fermi velocity of graphene carriers. The obtained $n_{2\mathrm{D}}$ with respect to μ is plotted in Figure3. 5 (a). To obtain the μ from 1eV to 1.7eV, a $n_{2\mathrm{D}}$ of $0.75\times10^{14}\mathrm{cm}^{-2}$ to $2\times10^{14}\mathrm{cm}^{-2}$ is required. From equation (3.1), the real and imaginary parts of graphene in-plane dielectric constant are shown in Figure3. 5 (a) and (b) with μ ranging from 1eV to 1.7eV along with μ of 0.5eV and 0.8eV, showing a negative dielectric constant in the near-IR range with high doping level (μ>1eV).

The negative Re $\{\varepsilon_{||}\}$ was observed with λ_0 from 0.7 μm to 1 μm, and is crucial for the GrSPP mode at the graphene-dielectric (where $\varepsilon > 0$) interface. To further understand the GrSPP characteristics, a λ_0-λ_{GrSPP} relationship was computed. Considering the SLG enclosed by two dielectrics ($\varepsilon_1, \varepsilon_2$), such as air($\varepsilon_1$=1) and anisotropic hBN($\varepsilon_{2,||}$=4.97 with $\varepsilon_{2,\perp}$=2.89 [65], and incident TM polarization, we have $\beta_{\mathrm{GrSPP}} = 2\pi/\lambda_{\mathrm{GrSPP}} = i\varepsilon_0(\varepsilon_1+\varepsilon_2)\omega/\sigma$ [60]. The resultant plot in Figure3. 4 (b) shows that the GrSPP has wavelength λ_{GrSPP} two orders of magnitude smaller than the λ_0, implying significant confinement of the related SPP. Such an aspect is in accord with the notion that while the GrSPP can be excited, there is nominally negligible response in the far field spectrum due to the near field confinement. Such a response is indicated at the bottom of Figure3. 6 (a) through the relatively flat green feature. However, the integration of the graphene with an MDM will be now shown to yield significant spectral modulation.

Probing single-layer graphene SPP coupled to MDM resonances

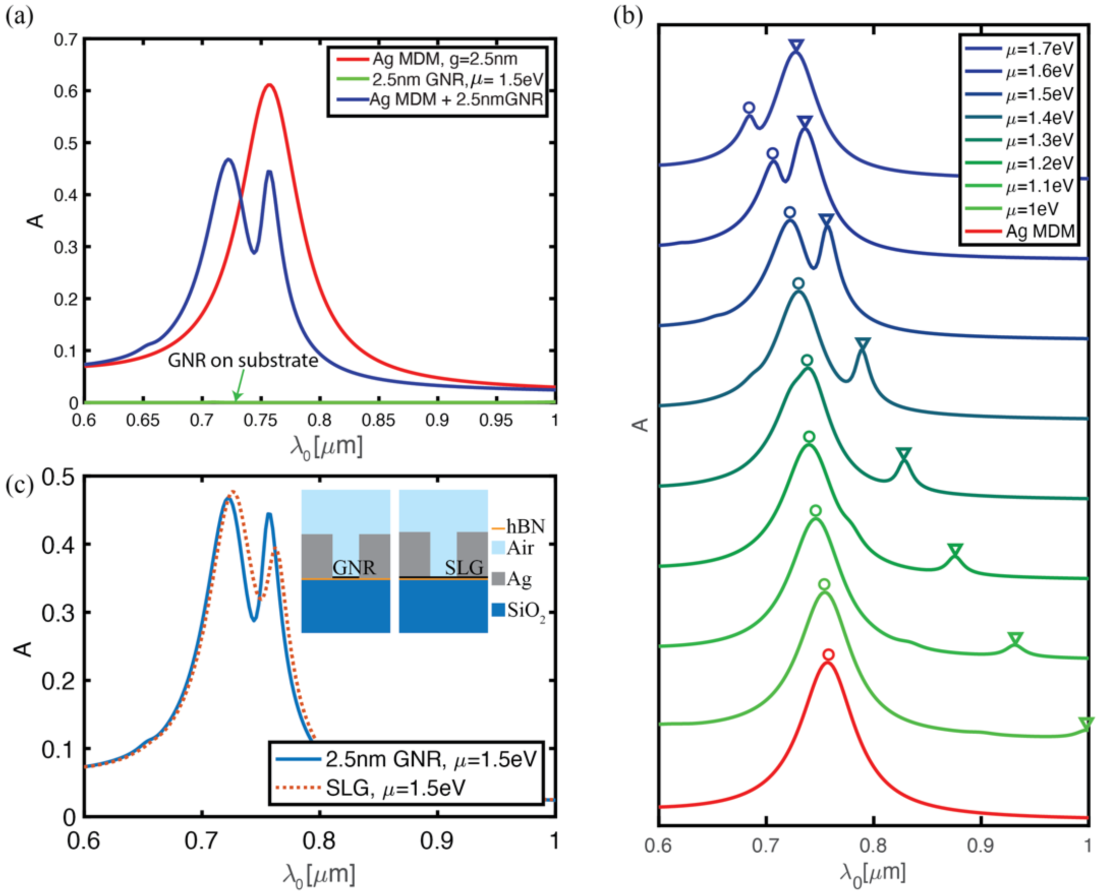

Figure3. 6(a)The absorption (A) vs λ_0 with and without GNR. (b) The absorption spectra for GNR in the MDM structure, with m varying from 1eV to 1.7eV; (c) Spectral variation of the absorption, for GNR and SLG.

We investigate the influence of the GrSPP resonance signal in the far-field spectrum through its modulation of the F-P resonance related to the MDM structure, considering the configuration of Figure3. 4(a). Here, the metallic grating serves to support the F-P like mode and presents a reflective boundary for the GrSPP. The confined GrSPP forms standing wave resonances, at the bottom of the gap. When the GrSPP and MDM F-P like SPP resonances are comparable in energy, the mutual coupling of the related excitations would need to be considered [44]. This may occur through the simultaneous excitation of *both* the GrSPP and MDM F-P like

SPP arising from the redistribution of electrical charges proximate to the graphene and Ag interface [44].

In Figure3. 6 (a), a comparison of the absorption in the MDM grating (*red curve*) with that for the grating with the SLG at the bottom of the gap (*blue curve*) is shown, for μ = 1.5 eV and g = 2.5 nm. The absorption (A) vs λ_0 of the metallic grating with and without a 2.5nm GNR (μ = 1.5eV) at the bottom of the MDM gap (h=w=55nm, g=2.5nm); The absorption related to the GNR on a substrate - without metallic grating is also indicated through the flat green feature at the bottom. While only one SPP resonance peak, corresponding to the MDM F-P like SPP mode, is apparent in the former case, with graphene there are two peaks. The coupling between GrSPP and F-P like MDM mode is evident. For the GrSPP, the resonance follows the criteria:

$$\beta_{\mathrm{GrSPP}} \cdot g \sim 2p\pi \tag{3.4}$$

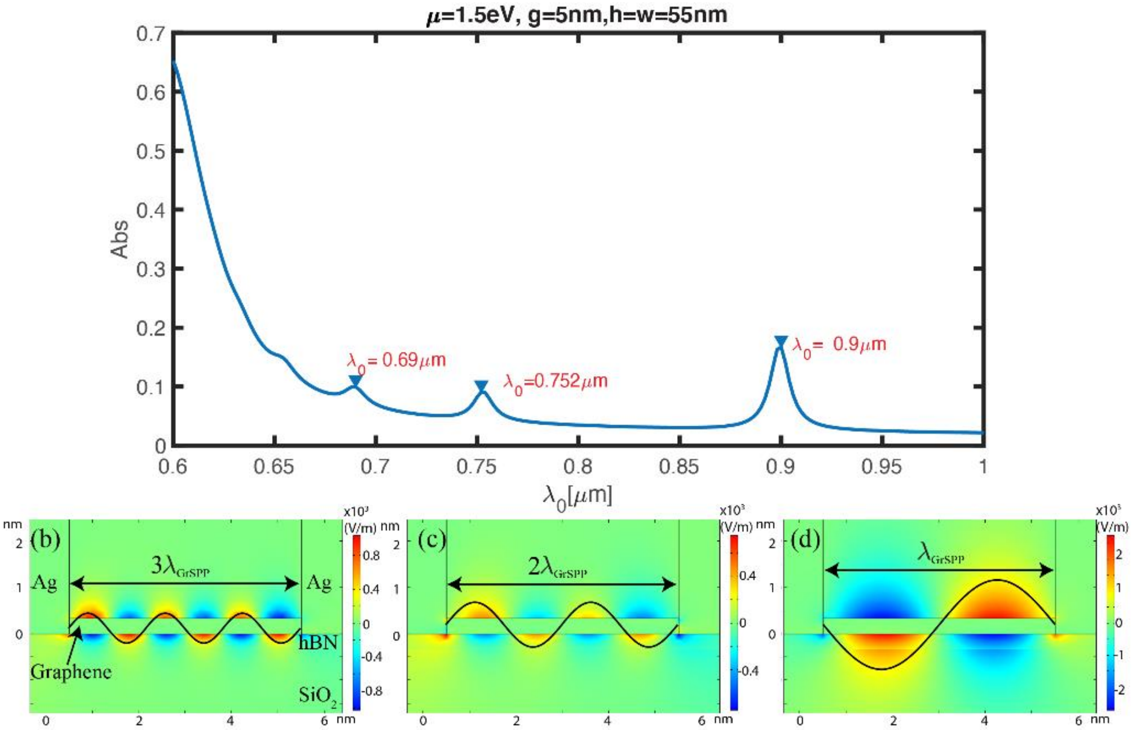

Figure3. 7(a) The absorption spectra of GrSPP resonances (μ=1.5eV) for an MDM structure with g=5nm, h=w=55nm; the corresponding E_y color map of each resonance peaks is shown in (c-d).

Here, p is an integer and the condition in Eqn. (3.4) implies coupling to the incident light, related to the electric field component: E_y as further elucidated, through Figure3. 7. The GrSPP resonance (along x) is antisymmetric, implying that the electric field on both surfaces of graphene is out of phase- see Figure3. 7 (b-c). As a result, the constructive interference only occurs for modes with even values of p [66]. From the dispersion relationship of GrSPP at a given μ: (b) and the MDM SPP: Fig. S1(a), we estimate the β_{GrSPP}=2856 μm^{-1} ~ (2π/2.5nm) and β_{MDM}~50μm^{-1}~(π/55nm) at λ_0~0.75μm, fulfilling the condition for the occurrence of both the MDM and graphene related SPP resonances: $\beta_{\mathrm{MDM}} \cdot h \sim \pi$ and $\beta_{\mathrm{GrSPP}} \cdot g \sim 2\pi$ (with h = 55 nm and g = 2.5 nm).

More specifically, an example of GrSPP resonances enhanced by the MDM F-P like SPP component is shown in Figure3. 7. The geometrical parameters, with g=5nm and h=w=55nm was chosen for indicating multiple orders of GrSPP resonances. In Figure3. 7(a), we are showing the absorption spectra of GrSPP resonances (μ=1.5eV) enhanced by MDM F-P like SPP resonances for an MDM structure with g=5nm, h=w=55nm; There are three clear peaks observed in the far field absorption spectra, in Figure3. 7(a). From the dispersion relationship of GrSPP (μ=1.5eV) in Figure3. 4(d), we obtain the following λ_{GrSPP} at each resonance peaks: λ_{GrSPP}~1.6nm (at λ_0=0.69μm), λ_{GrSPP}~2.2nm (at λ_0=0.752μm) and λ_{GrSPP}~3.8nm (at λ_0=0.9μm). In Figure3. 7 (c-d), The Ey field near the SLG surface is shown, representing different orders of standing wave constructive interferences corresponding to the resonance peaks in Figure3. 7(a), and fulfilling the resonance condition $\beta_{\mathrm{GrSPP}}\cdot g = (2\pi/\lambda_{\mathrm{GrSPP}})\cdot g \sim 2p\pi$ [66]. For example, at the wavelength of λ_0=0.69μm, $\beta_{\mathrm{GrSPP}}\cdot g = (2\pi/1.6)\times 5 \sim 6\pi$.

The double peak feature may be understood through a resonant energy splitting criteria [44]. With both MDM F-P like SPP and GrSPP (μ =1.5 eV) resonances coinciding at λ_0~0.75 μm, a resonance peak splitting was observed with two absorption peaks at 0.722 μm and 0.756 μm, in Figure3. 6 (a). By tuning the μ in the range of 1 eV to 1.7 eV, a modulation of the GrSPP and MDM SPP resonances is indicated: Figure3. 6 (b). The peaks on the right (downward triangles), when the μ < 1.5 eV represents the GrSPP resonance following $\beta_{\mathrm{GrSPP}}\cdot g \sim 2\pi$. For instance, with μ = 1.1 eV, at λ_0~0.9 μm we have λ_{GrSPP}~2.3 nm, and the observation of a small GrSPP resonance peak in the absorption spectrum. However, with an increased μ = 1.5 eV, the related GrSPP peak occurs at λ_0 ~ 0.76 μm with a seven-fold increase in the absorption, due to coupling with the MDM F-P like SPP. The blue shift of the MDM SPP with increasing μ indicates the enhanced influence of the graphene and is further discussed with Figure3. 8 .

The modulation effect (/modulation depth) of GrSPP at different μ on the MDM SPP resonance absorption from Figure3. 6 (b) can be defined as:

$$ModulationDepth = \frac{A_{MDM+GrSPP}(\mu) - A_{MDM}}{A_{MDM}} \times 100(\%) \qquad (3.5)$$

Here, A_{MDM} represents the absorption from the MDM (in the *absence* of graphene), while the $A_{MDM+GrSPP}$ represents the absorption from the MDM integrated with graphene (as a function of μ) The obtained modulation depth is indicated below in Figure3. 8 for λ_0 from 0.6 to 1.

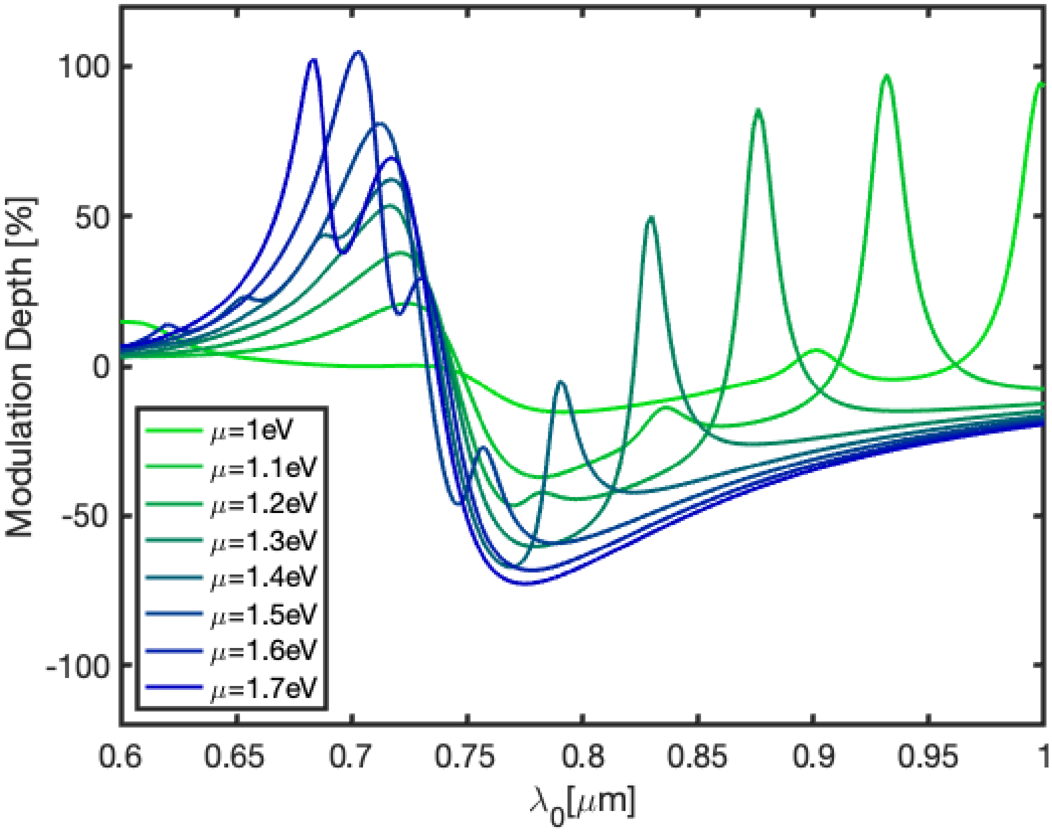

Figure3. 8 GrSPP modulation depth at different μ.

It is seen that a given modulation, say 50%, is achieved with a low (/high) μ, at a high (/low) l_o.- corresponding to a smaller (/larger) incident photon energy. Hence, the effect of GrSPP modulating MDM SPP at different doping level will determine the maximum modulation λ_0.

Generally, the placement of GNR with precise control of metallic structures on top is practically difficult. Alternatively, a complete single layer of graphene (SLG) can be used as shown in the *right inset* figure of Figure3. 6 (c). The related SLG SPP mode interaction with the F-P like MDM gap mode is indicated through the *red dotted* trace in Figure3. 6 (c). However, the absorption peak splitting corresponding to the GrSPP, and MDM SPP interaction seems less pronounced compared to the GNR case: Figure3. 6 (c). The latter is related to a more tightly confined GrSPP resonance as defined through *both* the graphene as well as the metal edges.

Deployment of the *hybrid* GrSPP – MDM SPP interaction for transducing refractive index changes and application for analyte sensing

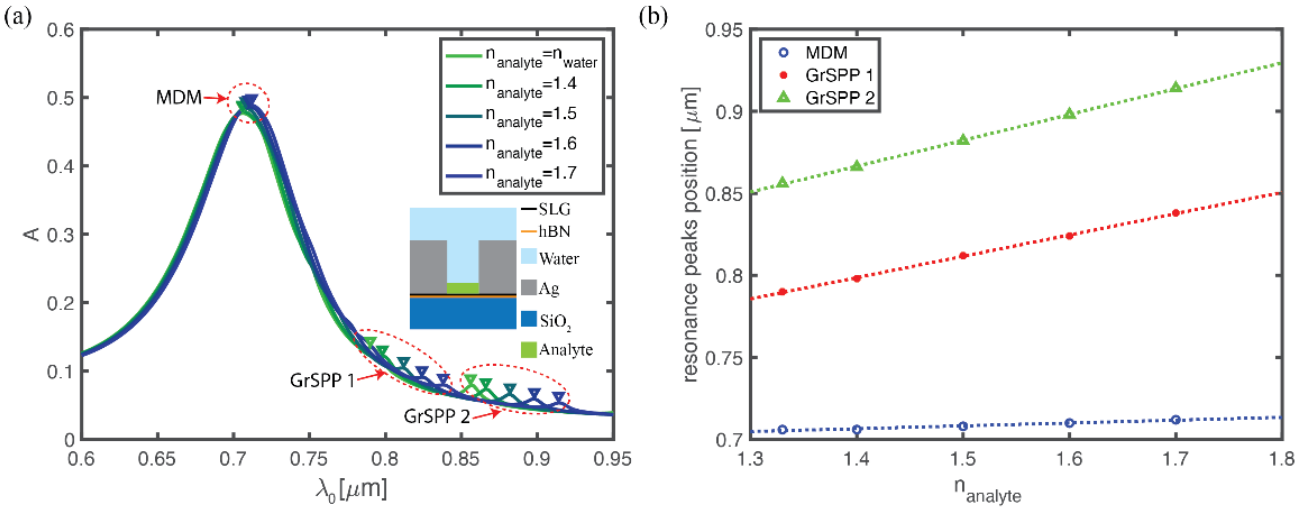

Figure3. 9(a) The spectral variation of the absorption (A) as a function of an analyte ($n_{analyte,}$); (b) The respective resonance peak shift as a function of the change in the refractive index unit (RIU) of the analyte.

Taking advantage of the tunability of the GrSPP - MDM SPP interaction, we propose its utilization for a sensor modality. We define the sensitivity of the *hybrid* SPP resonance through the peak shift (in wavelength units) with respect to a given refractive index (n) change, in units of nm/RIU, where RIU: refractive index unit. As an example, consider the SLG (say, of $\mu = 1.5$ eV) embedded under the Ag grating structure with $g = 10$ nm, $w = 80$ nm, $h = 80$ nm, the chosen parameters chosen for length scales achievable through lithography. With the analyte (say, of thickness ~ 1 nm) adsorbed on the graphene surface: Figure3. 9(a) inset, the effective n of the assembly would be manifested in the observed spectrum. A varying analyte characteristic *e.g.,* the n_{analyte}, from ~ 1.3 (say, glucose) to 1.7 (say, for mutagens such as diiodomethane) would be indicated through a shift of the SPP resonances. The spectral variation of the absorption (A) as a function of an analyte ($n_{\text{analyte,}}$) –as considered through the refractive index. Three resonance peaks were observed, in Figure3. 9 (a). Three absorption peaks were observed at ~ 0.7 μm, ~ 0.8 μm and ~ 0.9 μm, and labeled as MDM, GrSPP1 and GrSPP2, respectively. The change of the resonance peak position with respect to the n_{analyte}, is indicated in (b), plotted as the respective resonance peak shift as a function of the change in the refractive index unit (RIU) of the analyte, which can be used for transducing the index changes of the analyte. The GrSPP related peaks show a ten-fold higher sensitivity (GrSPP1~ 130 nm/RIU at λ_0 ~ 0.8μm and GrSPP2 ~ 157.6 nm/RIU at λ_0 ~ 0.9μm) compared to the MDM SPP resonance (~ 17.2 nm/RIU at λ_0~ 0.7μm). The utility of the GrSPP in concert with the SPPs arising from MDM based resonances for sensing applications is hence indicated. A further investigation of GrSPP based sensing, with respect to MDM geometry, is discussed in Figure3. 10.

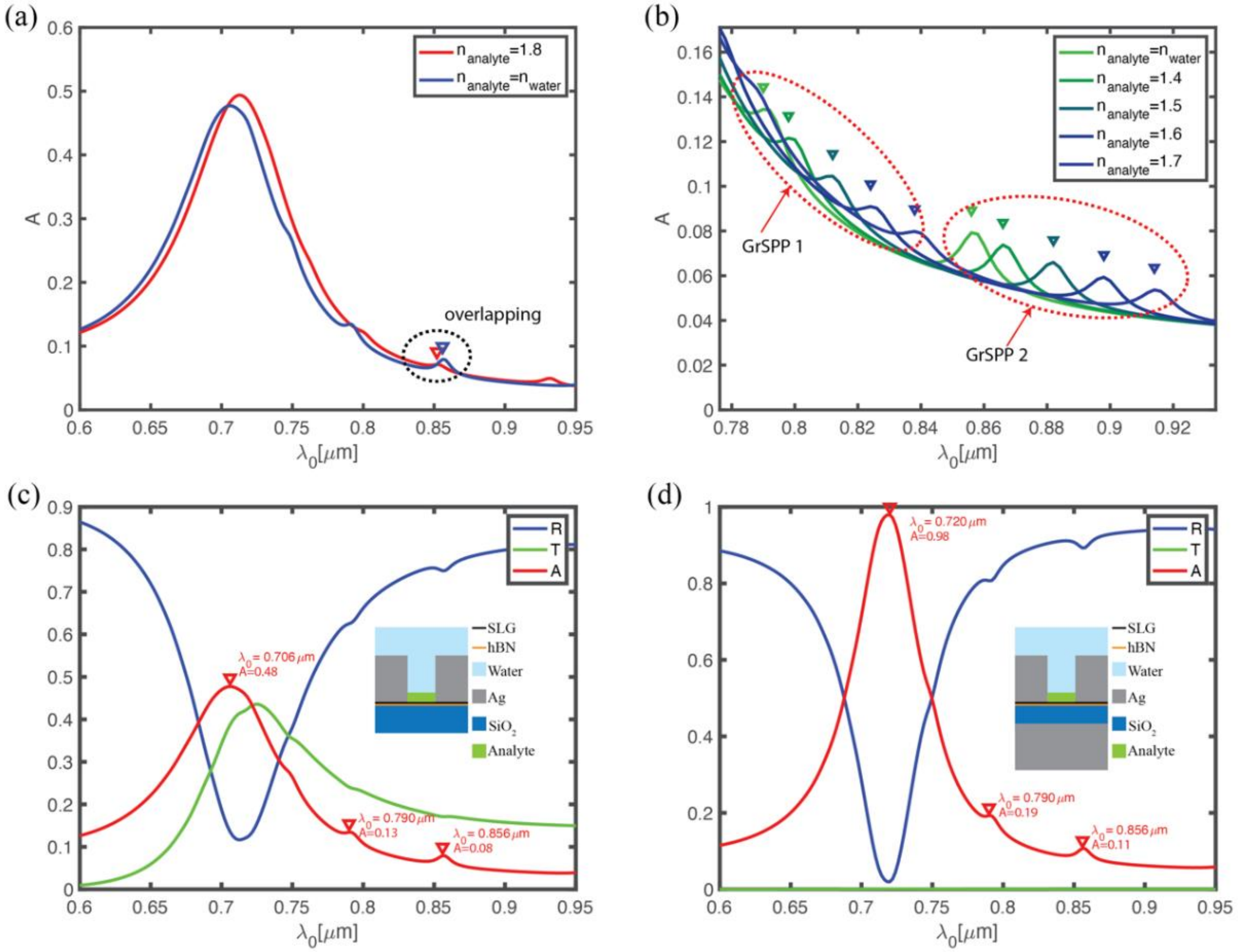

Figure3. 10(a) The overlap of the first and second order GrSPP; (b) The magnitude of the absorption decreases with higher $n_{analyte}$. (c) A nominal reflection (R), transmission (T), and absorption (A); (d) The A could be increased to be close to unity through a change in the structural.

The significant enhancement of GrSPP surface refractive index sensing with MDM SPP (Figure3. 9) shows great potential of sensing application. As in Figure3. 9 (a), there are two resonances from GrSPP (GrSPP1 and GrSPP2, at short and long wavelengths, respectively). A shift of the resonance peaks (i) towards longer λ_0 , along with (ii) reduced amplitude of absorption (A), was observed with a higher $n_{analyte}$. The former aspect could lead to potential overlap from the different resonance orders of the GrSPP resonance. An example of GrSPP1 ($n_{analyte}$=1.8) overlapping with GrSPP2 in an aqueous environment (n_{water} = 1.33), as relevant to biological media, is shown in Figure3. 10(a). The decrease of the magnitude of the absorption of the GrSPP resonances with increasing $n_{analyte}$ is indicated in Figure3. 10 (b). Consequently, the fidelity of detection of the absorption would be reduced with a higher $n_{analyte}$ due to the (i) overlap with features, say in aqueous ambients, as well as (ii) reduced signal to background contrast.

There could be potential improvements in the absorption characteristics related to the MDM SPP. Indeed, structural geometry variations could boost the absorption close to unity, as indicated in Figure3. 10 (c) and (d). Figure3. 10 (c) indicates the reflection (R), transmission (T), and absorption (A) plotted together, considering the GrSPP - MDM SPP interaction (g = 10nm, w = h = 80nm) for analyte sensing, e.g., with $n_{analyte}$= 1.33, corresponding to the refractive index for water. A nominal reflection (R) of ~ 0.1, transmission (T) ~ 0.4, and an absorption (A) ~ 0.48 is indicated. The resonance absorption could be enhanced to unity, e.g., through using an additional reflection layer (Ag) under the dielectric layer (10nm thickness, SiO_2), as shown in the inset to Figure3. 10 (d). With a consequent T ~ 0, we obtain a near unity absorption in the designed MDM grating. The absorption increase is now mainly related to the MDM SPP resonance at λ_0 ~0.7μm. While the absorption related to the MDM SPP resonance is increased by a factor of two, i.e., from ~ 0.48 to ~ 0.98, the magnitude of absorption (A) of the GrSPP1 peak increases ~ 46% (from ~ 0.13 to ~ 0.19) while the absorption for the GrSPP2 peak increases ~ 38 % (from ~ 0.08 to ~ 0.11). Therefore, the relative absorption of the GrSPP1, i.e., the ratio of A(GrSPP1) to A(MDM) decreases from 0.27 to 0.19, and the relative response of GrSPP2 also decreases from ~ 0.17 to ~0.11. The sensitivities of GrSPP with and without reflection layer was also investigated, however, we did not observe the improvement of sensitivity even through the MDM absorption may be made to increase substantially.

Conclusion

We have indicated that the hybrid coupling of SPP modes, arising from the GrSPP and the MDM SPP, can be modulated by tuning the μ of the graphene, through carrier density variation. A seven-fold enhancement of the GrSPP resonance peak was observed in the far field spectra in the near - IR regime, when a supporting MDM based grating was deployed. The hybrid GrSPP-MDM SPP platform can be used for enhanced signal as well as larger sensitivity, *e.g.*, an order of magnitude larger spectral change was obtained for a given refractive index unit change. The related principles offer possibility for analyte sensing at the nanometer scale.

Acknowledgements

Chapter 3, in full, is a reprint of the material as it appears in Dong, Yongliang, and Prabhakar R. Bandaru. "Enhanced graphene surface plasmonics through incorporation into metallic nanostructures." *Optics Express* 30.17 (2022): 30696-30704. The dissertation author was the primary investigator and author of this paper.

Chapter 4. Femto-molar level specific detection of lead ions in aqueous environments, using aptamer-derivatized graphene field effect transistors

The detection of lead ion (Pb^{2+}) contamination in aqueous media is relevant for preventing endemic health issues as well as damage to cognitive and physical health. Existing home kit tests are unable to achieve clinically relevant sensitivity and specificity. Here, a label free graphene field-effect transistor (GFET) sensor for detecting Pb^{2+} at the femto-molar (fM) level, discriminating between confounding ions, is reported. The sensing principle is based on electrically monitoring Pb^{2+} binding mediated conformational changes of a specific aptamer tethered to graphene, modeled through the Hills-Langmuir mechanism. A *record sensitivity* - through a limit of detection (LoD) of ~ 61 fM (femtomolar), for Pb^{2+} was demonstrated. For model verification, *specific* discrimination of Pb^{2+} from other ions, at the 1 picomolar (pM) level was shown. The reported work provides motivation for development of portable, label free, point of care (POC) devices with *both* high specificity and sensitivity.

Introduction

Lead exposure is a serious health concern with detrimental effects on public health [69,70,71], and through endemic disease outbreaks [72,73,74,75]. A lead concentration more than 15 ppb (~72 nM) in drinking water and larger than 100 µg/L (0.48 mM) in blood could lead to pernicious outcomes such as stunted human growth and development [76]. Consequently, there is substantial motivation for lead ion (Pb^{2+}) detection. The conventional methods of detection, *e.g.,* inductively coupled plasma mass spectrometry (ICP-MS), atomic emission/absorption spectroscopy, *etc.,* while accurate, involve costly instrumentation [71,77,78]. Alternately, home-kits utilizing colorimetric schemes are unreliable and have a poor limit of detection (LoD), typically ~ 10 mg/L (~ 48 mM) [69]. Given such issues, portable electrochemical sensors conjugated with Pb^{2+} specific aptamer (*Ap*) [79,80,81] and relying on sensor surface interactions, promise an attractive alternative for improved LoD. However, nonspecific interactions between confounding ions must be prevented to reduce the chances of false reporting.

Considering all such aspects, we propose an *Ap* (short chain ssDNA) incorporated graphene field effect transistor (GFET) - based device for Pb^{2+} detection [79,80,81,82,83,84]. The graphene layer in the GFET was functionalized with specific *Ap* receptor probes [79,80,81,82,83,84,85,86,87,88]. The binding of the target Pb^{2+} to the *Ap* is transduced into modulations of the electrical current through the GFET. While graphene, has been extensively deployed in FET-based sensors, as indicated in many reviews [95,96,97,98], significantly less work [81] has been done with regard to specific and sensitive Pb^{2+} detection.

We demonstrate how optimization of sensing protocols yields *ultrasensitive* lead ion concentration: [Pb^{2+}], specific detection, at the femtomolar (fM) level significantly improving, by orders of magnitude, extant reported values [79,80,81,82,83]. Further, the specificity was substantially enhanced to the picomolar (pM) level. Comparing to earlier GFET related work, it was indicated that the use of 8-17 nucleotide (NT) DNAzyme [81,82] (with dsDNA) for Pb^{2+} detection - enabled through the cleavage of one strand in the presence of Pb^{2+}, yielded an LoD of ~ 0.2 nM [81] and ~ 0.02 nM [82] with Au-nanoparticle decorated GFET, with specificity at 0.5 nM [81] and 0.1 nM [82], respectively. While DNAzymes show strong Pb^{2+} affinity, their large

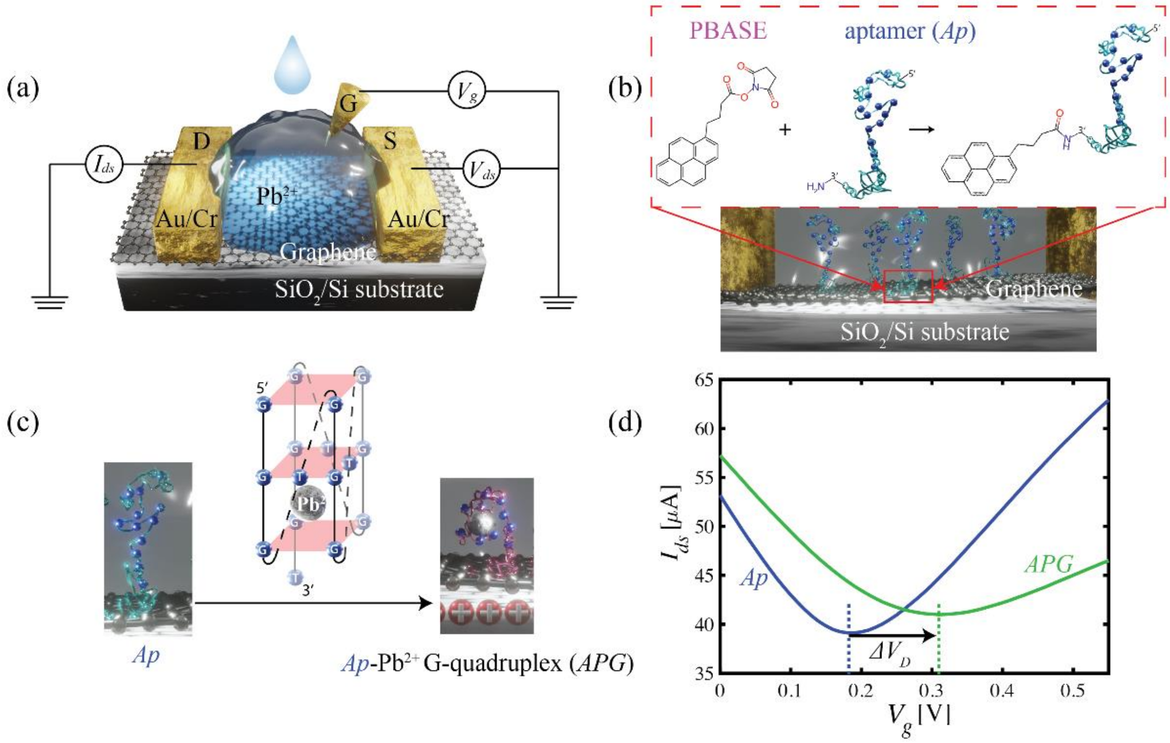

Figure4. 1**(a)** A schematic of the utilized GFET configuration. **(b)** Illustration of aptamer (Ap) immobilization on the graphene surface. **(c)** An unbound Ap (left) yields an Ap- Pb^{2+} G-quadruplex (APG). **(d)**The GFET Pb^{2+}detection mechanism.

size and related structural rigidity [102] make lower LoD difficult. In other studies [79,80], a guanine (G) enriched *Ap* placed on the graphene surface was reported to have an LoD of 2 μM [80] with a SiO_2 back-gated GFET and an LoD of ~ 0.8 nM [79] of Pb^{2+} on an HfO_2 gated GFET, with specificity ~ 48 nM [79].

We show that the LoD as well as the specificity for [Pb^{2+}] detection may be improved significantly by *orders of magnitude*. We adapted a G-quadruplex structured *Ap* based modality for label-free Pb^{2+} detection, yielding LoD as low as ~ 61 fM and specific determination of [Pb^{2+}] at 1 pM. The LoD was found to be critically dependent on the incubation time, which regulates the amount of immobilized *Ap* on the graphene surface. An optimal sensing protocol was determined through extensive experimentation. Further, the sensitivity was related to the doping induced carrier density (n_0) and carrier mobility (m) of the graphene, arising from an *Ap* -Pb^{2+} - G-quadruplex (*APG*) formation.

Experimental Section and methods:

The GFET fabrication and details on experimental measurements, as indicated in Figure4. 1**(a)** A schematic of the utilized *GFET* configuration. **(b)** Illustration of aptamer (Ap) immobilization on the graphene surface. **(c)** An unbound Ap (left) yields an Ap- Pb2+ G-quadruplex (APG). **(d)**The GFET Pb2+detection mechanism.**(a)**, which shows A schematic of the utilized graphene field effect transistor (GFET) configuration with source (S), drain (D), and gate (G) electrodes for the current (I) – voltage (V) measurements. The analyte consisting of various Pb^{2+} concentration/s is placed in contact with the graphene (transferred onto a SiO_2/Si substrate). A top electrolyte gating scheme was used for improved efficiency [105,106,107,108]. And further discussed in the *Methods and Supporting Information* (Sections S1 and S2). Briefly, 1-*P*yrene-*B*utanoic *A*cid N-hydroxy*S*uccinimidyl (NHS) *E*ster (PBASE, Anaspec, Inc.) was initially immobilized on the graphene surface. The pyrene group in PBASE is attached to the graphene surface *via* π-π interaction: as illustrated in Figure4. 1**(a)** A schematic of the utilized *GFET* configuration. **(b)** Illustration of aptamer (Ap) immobilization on the graphene surface. **(c)** An unbound Ap (left) yields an Ap- Pb2+ G-quadruplex (APG). **(d)**The GFET Pb2+detection mechanism. **(b)** where aptamer (Ap) immobilization on the graphene surface through a PBASE linker. Subsequently, the *Ap* (5'-GGGTGGGTGGGTGGGT/-NH_2-3', from IDT, Inc.) was linked to the PBASE: Figure4. 1**(a)** A schematic of the utilized *GFET* configuration. **(b)** Illustration of aptamer (Ap) immobilization on the graphene surface. **(c)** An unbound Ap (left) yields an Ap- Pb2+ G-quadruplex (APG). **(d)**The GFET Pb2+detection mechanism. **(b)**. The *Ap* was selected on the basis of (i) the affinity of nucleobases with Pb^{2+}, as well as its (ii) size, and (iii) extent of dynamic structure sensitive changes on binding to the Pb^{2+}. The Pb^{2+} ion shows stronger affinity toward N7/(C6)O of the G while the binding with cytosine (C), adenine (A), and thymine (T) is weaker, even compared to PBASE related phosphodiester linkage [99,100,101]. Consequently, a ssDNA based *Ap* with multiple G in the sequence was expected to enhance the *Ap* - Pb^{2+} binding affinity, with low affinity to other ions (*e.g.*, Ca^{2+}, Co^{2+}, Al^{3+}, Fe^{3+}, *etc*.) found in aqueous environments [79,102]. The related interaction between the amine group of the *Ap* with the NHS ester [79,80,81,82] is indicated in Figure4. 1**(a)** A schematic of the utilized *GFET* configuration. **(b)** Illustration of aptamer (Ap) immobilization on the graphene surface. **(c)** An unbound Ap (left) yields an Ap- Pb2+ G-quadruplex (APG). **(d)**The GFET Pb2+detection mechanism. **(b)**.

The PBASE-graphene platform functionalized with the chosen *Ap*, facilitates the formation of a specific *APG* (*Ap* -Pb^{2+} - G-quadruplex) structure - consisting of three planar arrays of four G NTs with Pb^{2+} in the cavity [101,102]: Figure4. 1**(a)** A schematic of the utilized *GFET* configuration. **(b)** Illustration of aptamer (Ap) immobilization on the graphene surface. **(c)** An unbound Ap (left) yields an Ap- Pb2+ G-quadruplex (APG). **(d)**The GFET Pb2+detection mechanism. **(c)**. In Figure4. 1**(a)** A schematic of the utilized *GFET* configuration. **(b)** Illustration of aptamer (Ap) immobilization on the graphene surface. **(c)** An unbound Ap (left) yields an Ap- Pb2+ G-quadruplex (APG). **(d)**The GFET Pb2+detection mechanism. **(c)**, an unbound Ap (left) yields an Ap- Pb^{2+} G-quadruplex (APG) – right, with trapped Pb^{2+} in between the parallel stacked G-quadruplex planes. The APG plays a role in p-doping the graphene channel The *APG* is expected to induce positive charge carriers into the graphene surface channel, due to a conformational transformation arising from the Pb^{2+} binding that brings the negatively charged G species closer to the surface and forms the basis for the sensor response [79]. Due to its small size (16 NTs) as well as binding mediated dynamic folding, the chosen *Ap* enables Pb^{2+} detection in variable environments, *e.g.*, background electrolyte concentration/s. Subsequent to *Ap* immobilization, the graphene surface was treated by Ethanolamine (EA) to passivate the unlinked PBASE NHS groups. The electrical measurements were performed with the GFET in aqueous solutions with different Pb^{2+} concentration ($[Pb^{2+}]$), as described in further detail in the *Methods* section.

Graphene synthesis. Single layer graphene (SLG) was synthesized through low pressure (300 mTorr) chemical vapor deposition (LPCVD) on Cu foil (25 μm thickness, MTI Corp.), through using a mixture of Hydrogen (H_2, 15 sccm) and methane (CH_4, 2 sccm) for 2 hrs. The foil was pre-cleaned by trichloroethylene (TCE) followed by acetone and isopropyl alcohol (IPA) rinsing and N_2 blow dry. The pre-cleaned Cu foil was folded to ensure stable precursor flow [125], resulting in high quality large area SLG growth. The Cu foil was annealed for 1hr at 1000 ^{o}C, under 85 mTorr, to reduce residual contamination. The LPCVD grown SLG on Cu was spin coated (at 3000 rpm for 45 s) by 120K MW poly (methyl methacrylate) (PMMA) for subsequent wet transfer [126] onto an electrode patterned SiO_2/Si substrate. Oxygen (O_2) plasma etching was used to remove the SLG on the backside of the Cu foil. Ammonium persulfate (0.1M) solution was used to etch Cu foil and subsequently rinsed with DI water. The PMMA was dissolved using acetone for 1 h followed by IPA rinse and N_2 blow dry. The GFET fabrication was conducted through thin film deposition, photolithography, and plasma etching, as described in Figure. S2 of the *Supporting Information.*

Device Measurement. The GFET I_{ds}-V_g measurement was performed using two sourcemeters (Keithley 2400) one for applying constant source drain voltage V_{ds}(= 0.2 V) and monitoring the I_{ds}, the other for supplying V_g and monitoring the gate current (I_g). Prior to an I_{ds}-V_g measurement, the GFET sensor was pre-cleaned by DI water three times after the incubation of

PBASE, *Ap* and ethanolamine. The varying [Pb^{2+}] is directly measured in an electrolyte, with varying [Pb^{2+}]. The V_g was swept from negative voltage to positive voltage and backward for three cycles, at ~ 30 mV/s. The Dirac voltage: V_D was estimated from the V_g corresponding to the I_{ds} minimum in each cycle. For all measurements, the gate leakage current was found to be less than ~ 10 nA.

Results and Discussion:

In summary, the underlying mechanism related to FET based detection is broadly understood [79,80,81,82,83,84,85,86,87,88,103,104,105] and involves the modulation of the electrical current (I_{ds}) in the graphene channel between the drain and source electrodes, by the sensing moiety, such as the Pb^{2+} ion – which has been considered here as attached to the *Ap* yielding the *APG*. When there is no attached Pb^{2+}, there would be a particular gate voltage (V_g) where the I_{ds} may be tuned to a minimum: *blue trace* in Figure4. 1**(a)** A schematic of the utilized *GFET* configuration. **(b)** Illustration of aptamer (Ap) immobilization on the graphene surface. **(c)** An unbound Ap (left) yields an Ap- Pb2+ G-quadruplex (APG). **(d)**The GFET Pb2+detection mechanism. **(d)**. Alternately, when there is attachment of Pb^{2+}, manifested through the *APG* formation, a different V_g would be required to indicate the I_{ds} minimum: *green trace* in Figure4. 1**(a)** A schematic of the utilized *GFET* configuration. **(b)** Illustration of aptamer (Ap) immobilization on the graphene surface. **(c)** An unbound Ap (left) yields an Ap- Pb2+ G-quadruplex (APG). **(d)**The GFET Pb2+detection mechanism. **(d)**. The related V_g yielding the minimum I_{ds} is termed the Dirac voltage (= V_D). The difference of the V_g in both the cases is indicated through the ΔV_D, indicating The Pb^{2+}detection mechanism involves the *APG* formation that is detected as a shift in the Dirac voltage: ΔV_D, in the $I_{ds} - V_g$ characteristics. A positive (/negative) value of the ΔV_D may be obtained to the presence of positive

(/negative) n_0 in the graphene. The n_0 may be correlated to the amount of *APG* formation, and as proportional to the present [Pb^{2+}].

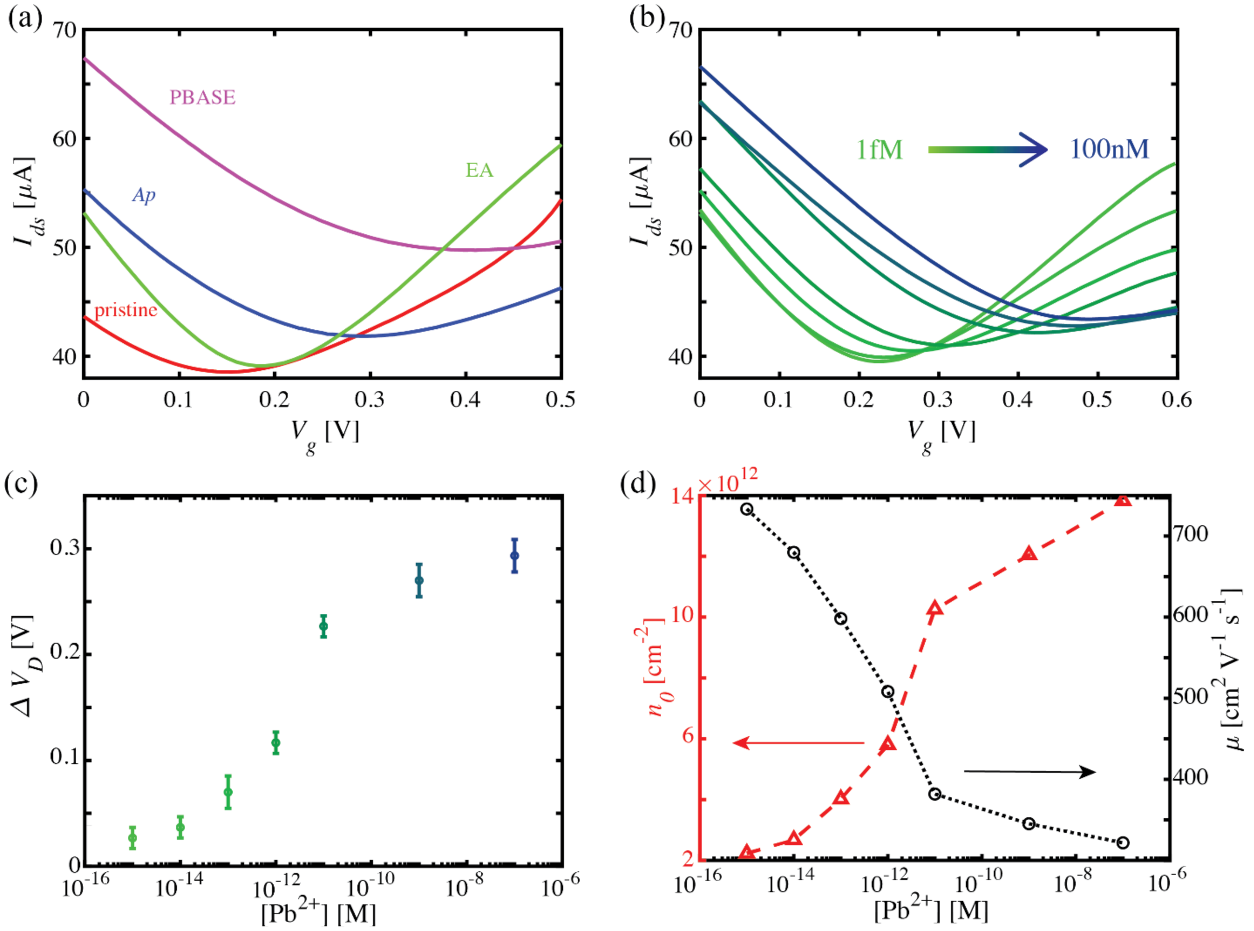

Figure4. 2**(a)** The variation of the I_{ds}-V_g characteristics as a function of the preparation of the GFET for Pb^{2+} detection. **(b)** The change in the I_{ds}-V_g characteristics as a function of [Pb^{2+}]. **(c)** The change in the V_D with [Pb^{2+}]. **(d)** The determined charge carrier density n_0, and the hole mobility (μ), as a function of the estimated [Pb^{2+}].

However, given the extreme responsivity of the graphene surface, it is important to monitor the variation of the V_D arising just from the preparation of the GFET towards Pb^{2+} detection: Figure4. 2**(a)** The variation of the Ids-Vg characteristics as a function of the preparation of the GFET for Pb2+ detection. **(b)** The change in the Ids-Vg characteristics as a function of [Pb2+]. **(c)** The change in the VD with [Pb2+]. **(d)** The determined charge carrier density n0, and the hole mobility (μ), as a function of the estimated [Pb2+].**(a)**, which shows The variation of the I_{ds}-V_g characteristics as a function of the preparation of the GFET for Pb^{2+} detection, comparing (i) pristine graphene, with the characteristic after (ii) attachment of the PBASE linker onto the graphene: purple, followed by (iii) addition of the Ap (10 mM): blue, and then (iv) ethanolamine (EA) addition: green. We outline the related modulations of the electrical signals. In sequence, (i) a positive shift of V_D ~ 0.25 V was observed after attaching the PBASE linker onto the graphene, due to the positive charge transfer from the PBASE to the graphene [109], (ii) the addition of the *Ap* (10 mM, diluted in 1X PBS: phosphate buffered saline solution) induced an opposite/negative V_D shift of ~ - 0.1 V after 30 minutes (min) of incubation, and (iii) finally, the EA addition yields again a negative V_D shift of ~ - 0.1 V. The net V_D change, just due to the preparation, is ~ 0.05 V, and sets a baseline for subsequent measurement related to Pb^{2+} addition. The electrical measurements were performed after ~ 10 min of incubation with various concentrations of Pb^{2+} (from 1 fM upwards: Figure4. 2**(a)** The variation of the Ids-Vg characteristics as a function of the preparation of the GFET for Pb2+ detection. **(b)** The change in the Ids-Vg characteristics as a function of [Pb2+]. **(c)** The change in the VD with [Pb2+]. **(d)** The determined charge carrier density n0, and the hole mobility (μ), as a function of the estimated [Pb2+]. **(b)**) in aqueous electrolyte background – prepared through mixing $Pb(NO_3)_2$ with DI water. The saturation of the ΔV_D with $[Pb^{2+}]$ > 1 nM: Figure4. 2**(a)** The variation of the Ids-Vg characteristics as a function of the preparation of the GFET for Pb2+ detection. **(b)** The change in the Ids-Vg characteristics as a function of [Pb2+]. **(c)** The change in the VD with [Pb2+]. **(d)** The determined charge carrier density n0, and the hole mobility (μ), as a function of the estimated [Pb2+]. **(c)**, indicates that the majority of the attached *Ap* has combined with the added Pb^{2+}. Different $[Pb^{2+}]$ yield proportional amounts of the *APG* and could be correlated to the magnitude of the ΔV_D.

A continuous ΔV_D shift to a more positive value with increasing $[Pb^{2+}]$ was observed: Figure4. 2**(a)** The variation of the Ids-Vg characteristics as a function of the preparation of the GFET for Pb2+ detection. **(b)** The change in the Ids-Vg characteristics as a function of [Pb2+]. **(c)** The change in the

VD with [Pb2+]. **(d)** The determined charge carrier density n0, and the hole mobility (μ), as a function of the estimated [Pb2+]. **(b) & (c**). In Figure4. 2**(a)** The variation of the Ids-Vg characteristics as a function of the preparation of the GFET for Pb2+ detection. **(b)** The change in the Ids-Vg characteristics as a function of [Pb2+]. **(c)** The change in the VD with [Pb2+]. **(d)** The determined charge carrier density n0, and the hole mobility (μ), as a function of the estimated [Pb2+]. **(b)**, the change in the I_{ds}-V_g characteristics as a function of Pb^{2+} concentration ([Pb^{2+}]) in the range of 100 aM to 100 nM was plotted. The $(V_g)_{min}$ is termed the Dirac voltage (V_D). In Figure4. 2**(a)** The variation of the Ids-Vg characteristics as a function of the preparation of the GFET for Pb2+ detection. **(b)** The change in the Ids-Vg characteristics as a function of [Pb2+]. **(c)** The change in the VD with [Pb2+]. **(d)** The determined charge carrier density n0, and the hole mobility (μ), as a function of the estimated [Pb2+]. **(c)**, the change in the V_D with [Pb^{2+}] was shown. Such variation was understood in terms of increased *p*-doping of the graphene channel induced *via* the *APG* formation [79,80,101]. We quantify the extent of the related positive charge (/*hole*) induction, through a [Pb^{2+}] accrual induced carrier density (n_0) [110,111,112]. The n_0 was parameterized through the product of a total capacitance (C_T) and the ΔV_D, through:

$$n_0 = \frac{C_T(\Delta V_D)}{e}$$

$$\frac{1}{C_T} = \left(\frac{1}{C_{EDL} + C_P} + \frac{1}{C_Q}\right) \tag{4.1}$$

The C_T was measured to be ~ 2 μF/cm^2 (see *Section S3* of the *Supporting Information* for detailed capacitance modeling and measurement/s), and constituted from a C_{EDL}: an electrolyte double layer capacitance in parallel to a capacitance C_P [113] contributed by the surface immobilized *Ap*, along with a quantum capacitance [114] (C_Q) in series with the C_{EDL} and C_P. The carrier (/hole) mobility (μ) in the graphene was then estimated from the following relation [110,111,112]:

$$R_{channel} = \frac{L/W}{e\mu n_{tot}} = \frac{L/W}{e\mu\sqrt{\left(\frac{C_T}{e}\right)^2 \left(V_g - V_D\right)^2 + {n_0}^2}} = \frac{V_{ds}}{I_{ds}} \tag{4.2}$$

The $R_{channel}$ is the resistance of the graphene channel, with L (= 500 μm) and W (= 200 μm) as the channel length and width. The $(C_T/e)(V_g\text{-}V_D)=n_g$ is the gate induced carrier density at different V_g with respect to the V_D, and n_{tot} (= $\sqrt{{n_0}^2 + {n_g}^2}$) is a *net* carrier density [111]. The variation of the ΔV_D with [Pb^{2+}] is shown in Figure4. 2**(a)** The variation of the Ids-Vg characteristics as a function of the preparation of the GFET for Pb2+ detection. **(b)** The change in the Ids-Vg characteristics as a function of [Pb2+]. **(c)** The change in the VD with [Pb2+]. **(d)** The determined charge carrier density n0, and the hole mobility (μ), as a function of the estimated [Pb2+]. **(c),** and the estimated μ and n_0 is shown in Figure4. 2**(a)** The variation of the Ids-Vg characteristics as a function of the preparation of the GFET for Pb2+ detection. **(b)** The change in the Ids-Vg characteristics as a function of [Pb2+]. **(c)** The change in the VD with [Pb2+]. **(d)** The determined charge carrier density n0, and the hole mobility (μ), as a function of the estimated [Pb2+]. **(d)**, where the determined charge carrier density n_0: red triangles, and the hole mobility (m): black open circles, as a function of the estimated [Pb^{2+}] was shown. It was observed that higher [Pb^{2+}] leads to increasing n_0 from ~ 2 x 10^{12} cm^{-2} to ~ 14 x 10^{12} cm^{-2} and an associated decreased μ from ~740 cm^2/Vs to ~ 320 cm^2/Vs, arising from the additional scattering of the carriers on the graphene surface due to *APG* formation.

To further understand the observed response, we probed the binding affinity of *APG* to the graphene, deploying the Hills-Langmuir model [87]. Here, the ΔV_D is a function of the [Pb^{2+}], through the relation:

$$\Delta V_D = A\frac{[\mathrm{Pb}^{2+}]^h}{K_d^h + [\mathrm{Pb}^{2+}]^h} + B \tag{4.3}$$

The A is the maximum ΔV_D response, presumably obtained when all *Ap* binding sites are occupied. The B is a fit to the lowest expected ΔV_D as for a *blank sample* (GFET without [Pb^{2+}]). The K_d is an equilibrium constant (= $\frac{[APG]}{[Ap][\mathrm{Pb}^{2+}]}$) related to the *APG* formation, *i.e.,* with respect to the equilibrium:

$$[Ap] + [\mathrm{Pb}^{2+}] \rightleftharpoons [APG] \qquad (4.4)$$

The square brackets indicate the respective concentrations. When the K_d equals the [Pb^{2+}], the *Ap* on graphene surface is half occupied by Pb^{2+} (see *Section S4* of the *Supporting Information*). The h is a coefficient related to the mutual interaction as manifested through a defined *cooperativity* . It was observed that the A in **Eqn. (4.3),** was increased with a longer incubation time, representing higher response, as also seen through an increased ΔV_D with higher [Pb^{2+}]: see *inset* to Figure4. 3**(a)** The change in the VD (DVD) with [Pb2+], as a function of the Ap incubation time. **(b)** The determination of the LoB and LoD. (**c)** The variation of the transconductance (gm). **(d)** The Raman spectrum of the pristine graphene subsequent to 30 mins, 2 h, and 4 h of Ap incubation. **(e)**. The ratio between I2D and IG.**(a)** - due to a larger [*APG*] on the graphene surface.

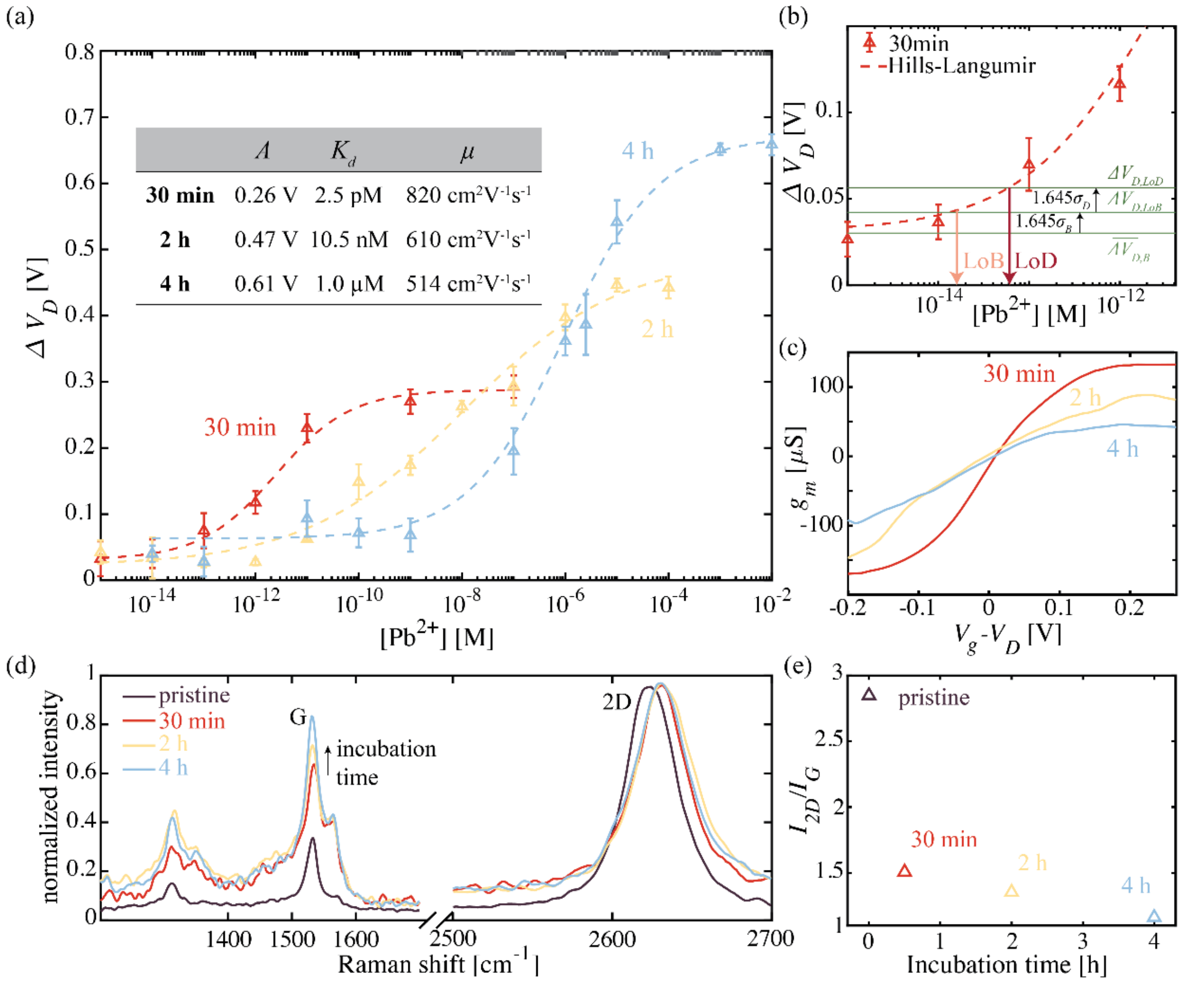

	A	K_d	μ
30 min	0.26 V	2.5 pM	820 $cm^2V^{-1}s^{-1}$
2 h	0.47 V	10.5 nM	610 $cm^2V^{-1}s^{-1}$
4 h	0.61 V	1.0 μM	514 $cm^2V^{-1}s^{-1}$

Figure4. 3**(a)** The change in the V_D (DV_D) with [Pb^{2+}], as a function of the Ap incubation time. **(b)** The determination of the LoB and LoD. (**c)** The variation of the transconductance (g_m). **(d)** The Raman spectrum of the pristine graphene subsequent to 30 mins, 2 h, and 4 h of Ap incubation. **(e)**. The ratio between I_{2D} and I_G.

In Figure4. 3**(a)** The change in the VD (DVD) with [Pb2+], as a function of the Ap incubation time. **(b)** The determination of the LoB and LoD. (**c)** The variation of the transconductance (gm). **(d)** The Raman spectrum of the pristine graphene subsequent to 30 mins, 2 h, and 4 h of Ap incubation. **(e)**. The ratio between I2D and IG.**(a)**, the change in the V_D (ΔV_D) with [Pb^{2+}], as a function of the Ap incubation time was shown. A Hills-Langmuir model (with parameters listed in the inset) incorporating the influence of the Ap incubation times, i.e., at 30 min: red, 2 h: yellow, and 4 h: blue, was used for modeling the associated Ap occupation and the binding kinetics. An LoD of ~

61 fM; ~ 7 pM and ~ 5 nM, were obtained respectively. The error bars were obtained through measurements on four devices tested at each concentration. The fit value of h for all incubation times was less than 1, indicating *negative* cooperativity arising from (i) the increasingly impeded binding of the *Ap* to the Pb^{2+}, due to proximate *APG* formation, as well as (ii) increased Pb^{2+} repulsion by induced positive charge carrier density from the *APG* [90]. At higher *immobilized* [*Ap*] on graphene, induced through longer incubation time, the n_0 increases as more charges from the *Ap* are involved. As seen in the *inset* to Figure4. 3**(a)** The change in the VD (DVD) with [Pb2+], as a function of the Ap incubation time. **(b)** The determination of the LoB and LoD. (**c)** The variation of the transconductance (gm). **(d)** The Raman spectrum of the pristine graphene subsequent to 30 mins, 2 h, and 4 h of Ap incubation. **(e)**. The ratio between I2D and IG. **(a)**, the h was reduced from 0.59 to 0.47 with increased incubation time – from ~ 30 mins to ~ 4 h.

The plots of ΔV_D *vs* Pb^{2+} concentration: Figure4. 3**(a)** The change in the VD (DVD) with [Pb2+], as a function of the Ap incubation time. **(b)** The determination of the LoB and LoD. (**c)** The variation of the transconductance (gm). **(d)** The Raman spectrum of the pristine graphene subsequent to 30 mins, 2 h, and 4 h of Ap incubation. **(e)**. The ratio between I2D and IG. **(a)**, indicate the necessity for considering the LoD and sensor response. A (limit of blank) LoB and an LoD, as a function of *Ap* incubation time, was estimated through the relations [115], also see Figure4. 3**(a)** The change in the VD (DVD) with [Pb2+], as a function of the Ap incubation time. **(b)** The determination of the LoB and LoD. (**c)** The variation of the transconductance (gm). **(d)** The Raman spectrum of the pristine graphene subsequent to 30 mins, 2 h, and 4 h of Ap incubation. **(e)**. The ratio between I2D and IG. **(b),** showing the determination of the LoB (Limit of Blank) and LoD (Limit of Detection) for [Pb^{2+}] with respect to the (ΔV_D) for 30 min *Ap* incubation.

$$\overline{\Delta V_{D,B}} + 1.645\sigma_B = \Delta V_{D,LoB} \leftrightarrow LoB \tag{4.5}$$

$$\Delta V_{D,LoB} + 1.645\sigma_D = \Delta V_{D,LoD} \leftrightarrow LoD$$

Here, the $\overline{\Delta V_{D,B}}$ and σ_B represents the average and standard deviation of the ΔV_D measurements of GFET on *blank* samples, *i.e.*, with no Pb^{2+} analyte *and* only with deionized water. The aspect that 90% of the measurements would be accounted for is indicated through the $1.645\sigma_B$ value correspondent to a standard normal distribution [115]. For example, with 30 mins *Ap* incubation, we obtained from the fits in Figure4. 3**(a)** The change in the VD (DVD) with [Pb2+], as a function of the Ap incubation time. **(b)** The determination of the LoB and LoD. (**c)** The variation of the transconductance (gm). **(d)** The Raman spectrum of the pristine graphene subsequent to 30 mins, 2 h, and 4 h of Ap incubation. **(e)**. The ratio between I2D and IG. **(a)**, that $\overline{\Delta V_{D,B}}$ = 0.030 V and σ_B of 0.0073 V. The determined LoB is 16.2 fM - corresponding to the $\Delta V_{D,LoB}$ = 0.042 V. Subsequently, the LoD was determined from the σ_D (= 0.0085 V) per the standard deviation of responses relative to the lowest [Pb^{2+}] detectable (~ 1 fM). With an estimated $\Delta V_{D,LoD}$ of 0.057 V, the LoD was estimated at 61 fM.

Table 1. The determined Limit of Detection (LoD) as a function of the Ap incubation time

Incubation time	$\overline{\Delta V_{D,B}}$	σ_B	$\Delta V_{D,LoB}$	**LoB**	σ_D	□$V_{D,LoD}$	**LoD**
30 min	0.030 V	0.0073 V	0.042 V	16.2 fM	0.0085 V	0.057 V	61.1 fM
2 h	0.022 V	0.0168 V	0.050 V	0.6 pM	0.0150 V	0.074 V	7.3 pM
4 h	0.063 V	0.0139 V	0.086 V	0.9 nM	0.0163 V	0.113 V	5.5 nM

Similarly, the LoB and the LoD was determined for the measurements on the GFET with 2 h, and 4 h of *Ap* incubation time (**Table 1**), and correlated to a K_d of 10.5 nM and 1.0 µM, respectively. The change in the *immobilized* [*Ap*] – through the K_d - from pM to µM, indicates an effective increase in the interaction of the *Ap* with the PBASE on graphene, presumably due to diffusional limitations. Furthermore, the *immobilized* [*Ap*] seems limited by the incubation time rather than the *bulk* [*Ap*], see Figure. S4 in the *Supporting Information*.

A higher LoD with longer *Ap* incubation time, *i.e.*, larger *immobilized* [*Ap*], could be attributed to a decrease in μ, and correlated to the FET device transconductance [94]: $g_m = \partial I_{ds}/\partial V_g$ (at a given V_{ds}). For example, with 30 mins, 2 h and 4 h incubation at different V_g: Figure4. 3**(a)** The change in the VD (DVD) with [Pb2+], as a function of the Ap incubation time. **(b)** The determination of the LoB and LoD. (**c)** The variation of the transconductance (gm). **(d)** The Raman spectrum of the pristine graphene subsequent to 30 mins, 2 h, and 4 h of Ap incubation. **(e)**. The ratio between I2D and IG. **(c)** showing the variation of the transconductance (g_m) with respect to the V_g, for different Ap incubation times. We observed a higher g_m (with a maximum ~ 130 µS) in the case of 30 min, while the maximum g_m reduces for 2 h and 4 h incubation (with a maximum ~ 90 µS and ~ 50 µS, respectively). The μ obtained through Eqn. (4.2), yielded a lower (/higher) value of 514 (/820) cm^2/Vs with *Ap* incubation time of 4 (/0.5) h, respectively. The decrease in μ may be associated with an increased n_0 at higher *immobilized* [*Ap*]. Since maximal sensing response may be reached when GFET is operated at maximal g_m [104], a higher μ with a higher g_m would be critical in optimizing the LoD.

Further investigation of carrier doping was done through Raman spectroscopy (at 532 nm, Renishaw inVia) on the *pristine* graphene and then on graphene *with* the immobilized *Ap* at different incubation times (30 min, 2 h, and 4 h): Figure4. 3**(a)** The change in the VD (DVD) with [Pb2+], as a function of the Ap incubation time. **(b)** The determination of the LoB and LoD. (**c)** The variation of the transconductance (gm). **(d)** The Raman spectrum of the pristine graphene subsequent to 30 mins, 2 h, and 4 h of Ap incubation. **(e)**. The ratio between I2D and IG. **(d)**. In Figure4. 3**(a)** The change in the VD (DVD) with [Pb2+], as a function of the Ap incubation time. **(b)** The determination of the LoB and LoD. (**c)** The variation of the transconductance (gm). **(d)** The Raman spectrum of the pristine graphene subsequent to 30 mins, 2 h, and 4 h of Ap incubation. **(e)**. The ratio between I2D and IG. **(d)**, The Raman spectrum (normalized to maximum intensity) of the surface of pristine graphene compared to that on the graphene surface subsequent to 30 mins, 2 h, and 4 h of *Ap* incubation. The shift of the 2D peak of graphene with increased *Ap* addition shifted to higher wavenumber indicative of p-type doping. The intensity of the G band (I_G) and D band (I_D) also increased with Ap incubation due to the doping. It was observed that the 2D peak of graphene with the *Ap* shifted to higher wavenumber (from ~ 2660 cm^{-1} to ~ 2667 cm^{-1}), indicative of hole doping [116,117]. The intensity of the *G* band (I_G) and *D* band (I_D) also increased with *Ap* incubation as related to an increased n_0 [118,119]. The ratio between 2D band intensity (I_{2D}) and I_G decreases from ~ 2.9 to ~ 1.5 with the addition of the *Ap* as well as longer incubation time: Figure4. 3**(a)** The change in the VD (DVD) with [Pb2+], as a function of the Ap incubation time. **(b)** The determination of the LoB and LoD. (**c)** The variation of the transconductance (gm). **(d)** The Raman spectrum of the pristine graphene subsequent to 30 mins, 2 h, and 4 h of Ap incubation. **(e)**. The ratio between I2D and IG. **(e)**.

The discriminative detection of Pb^{2+} in aqueous solutions, over other commonly found ions [120,121]. As indicated previously, the *Ap* was carefully chosen to have high affinity to Pb^{2+} alone, and it is consequently expected that other ions would not be able to form a related G-quadruplex [99,100,101,102]. To verify such assumption, Ca^{2+}, Co^{2+}, Al^{3+} and Fe^{3+} electrolyte solutions were prepared through dissolving associated nitrate salts into DI water, with dilution over a range of concentrations. An *Ap* (10 mM) incubation time of 30 min, was chosen, given the better LoD as indicated previously. The statistics from the tests in aqueous media on different GFET devices, along with the obtained ΔV_D, are reported in Figure4. 4 The specificity for Pb2+ detection over alternate ions, e.g., Ca2+, Co2+, Fe3+ and Al3. A threshold value for the ΔVD,T of 0.05V can be used to specifically identify Pb2+ when the electrolyte concentration ≥ 1 pM..

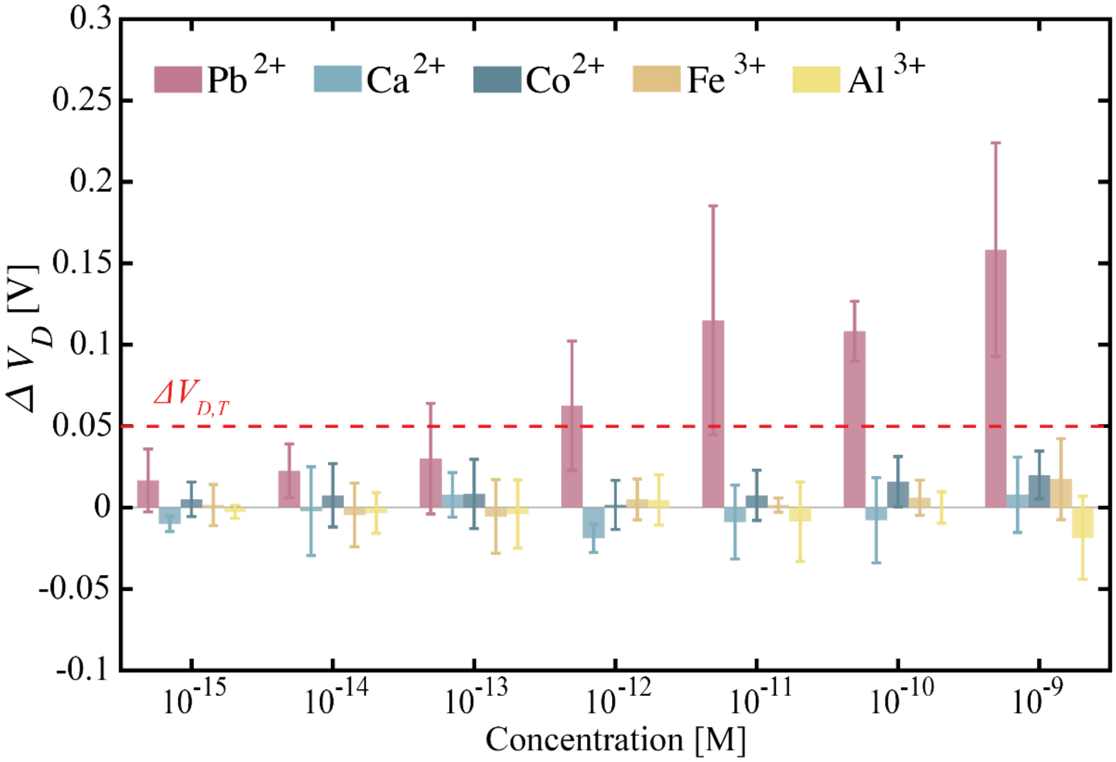

Figure4. 4 The specificity for Pb^{2+} detection over alternate ions, e.g., Ca^{2+}, Co^{2+}, Fe^{3+} and Al^{3}. A threshold value for the $\Delta V_{D,T}$ of 0.05V can be used to specifically identify Pb^{2+} when the electrolyte concentration ≥ 1 pM.

In Figure4. 4 The specificity for Pb2+ detection over alternate ions, e.g., Ca2+, Co2+, Fe3+ and Al3. A threshold value for the ΔVD,T of 0.05V can be used to specifically identify Pb2+ when the electrolyte concentration ≥ 1 pM., we investigated the specificity for Pb^{2+} detection over alternate ions, e.g., Ca^{2+}, Co^{2+}, Fe^{3+} and Al^{3+}, that may be present in aqueous solution-based analyte, indicated through the respective ΔV_D over an ion concentration range of 1 fM to 100 nM**.** The upper and lower bond of the error bar indicates standard deviation of the measured ΔV_D from different GFET devices. A threshold value for the $\Delta V_{D,T}$ of 0.05V can be used to specifically identify Pb^{2+} when the electrolyte concentration ≥ 1 pM. While a pronounced positive ΔV_D was observed for Pb^{2+}, in the case of the other ions, the ΔV_D was indifferent and close to zero, *i.e.*, there was no significant modulation with respect to the baseline ΔV_D, measured in DI water: Figure4. 4 The specificity for Pb2+ detection over alternate ions, e.g., Ca2+, Co2+, Fe3+ and Al3. A threshold value for the $\Delta VD_{,T}$ of 0.05V can be used to specifically identify Pb2+ when the electrolyte concentration ≥ 1 pM.. A threshold ΔV_D was defined ($\Delta V_{D,T}$ = 0.05 V, *red dashed* line), demonstrating ultrasensitive specific Pb^{2+} detection at the pM level.

Table 2. A comparison with the published sensitivity and the specificity of Ap-based Pb^{2+}sensors

Methods & Materials	**Sensitivity (LoD)**	**Specificity**	***Ap* Incubation**
Au electrode; *APG* [123]	35 nM	1 µM	120 mins; 4 µM
Au electrode+Au nanoparticles (NPs); *APG* [124]	4 pM	70 nM	60 mins; 15 µM
GFET, *APG*+Methylene blue [80]	2 µM	not reported	2 h; 15 µM
GFET, *APG* [79]	790 pM	48 nM	4 h; 1 µM
GFET, Pyrene-derivatized 8-17 DNAzyme [81]	181 pM	0.5 nM	30 min; 4 µM
GFET+Au NPs; Pyrene-derivatized 8-17 DNAzyme [82]	20pM	0.1 nM	2 h; 5 µM
GFET, electrolyte gated, *APG*	61 fM	1pM	30 min; 10 µM

Conclusions

Our studies indicate a superior LoD related sensitivity of ~ 61 fM, along with specificity at the 1 pM level, *both* of which are significantly better, by orders of magnitude, compared to previous work on *Ap* based Pb^{2+} detection, as detailed in **Table 2**. We have shown, through extensive characterization and consequent developed understanding, that key factors for the *record* specificity and LoD incorporate: (1) the selection of the *Ap*, along with (2) the optimization of the immobilized *Ap* surface occupation density as a function of the incubation time. Such aspects have not been brought to the fore in previous studies and helps interpret earlier measurements [123,124] as well. Our careful studies and quantification lay the basis for the next-generation Pb^{2+} detection sensors with the advantages of scalable fabrication, and low-cost, along with high sensitivity, and specificity.

Supporting information

S1. Graphene characterization

The single layer graphene (SLG) on SiO_2/Si substrate was characterized by optical microscopy and Raman spectroscopy at 532nm by Renishaw spectrometer (I_{2D}/I_G>2), in Figure4. 5(**a**) Optical microscopy image of the GFET (scale bar: 100μm) and the graphene channel on SiO2 substrate

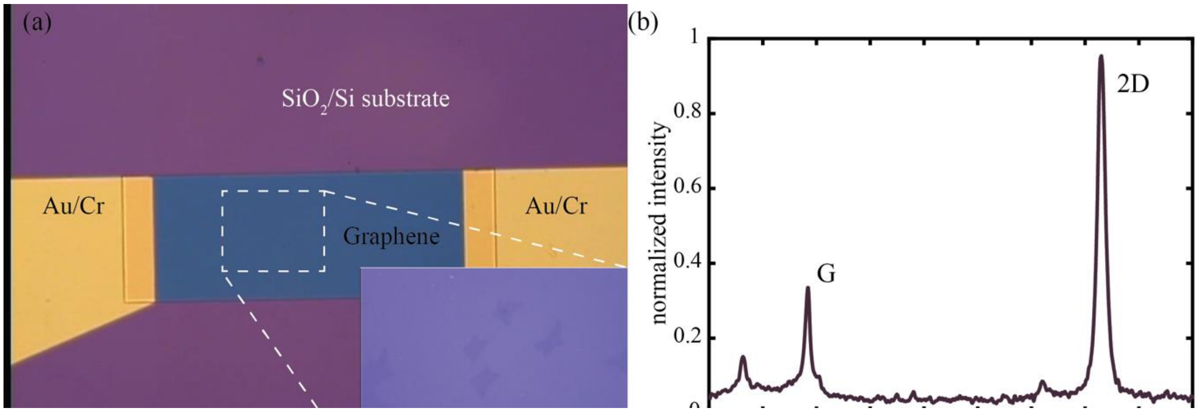

Figure4. 5(**a**) Optical microscopy image of the GFET (scale bar: 100μm) and the graphene channel on SiO_2 substrate (inset). (**b**) The Raman spectroscopy of graphene/SiO_2, the Raman peaks intensity is normalized by 2D peak

(inset). (**b**) The Raman spectroscopy of graphene/SiO2, the Raman peaks intensity is normalized by 2D peak.

S2. The graphene field effect transistor (GFET) fabrication

The graphene field effect transistor (GFET) was fabricated through photolithographic processes on graphene transferred onto thermal oxide SiO_2(300nm)/Si wafers, as the graphene field effect transistor (GFET) fabrication processes schematically shown in Figure4. 6 The graphene field effect transistor (GFET) fabrication processes, include (a) electrode patterning. (b) oxide (SiO2) deposition, (c) Transfer of graphene, (d) definition of the graphene channel (e) FET definition, followed by (f) PDMS mold around the channel to hold the liquid analyte. . A typical device was configured with a 500 µm × 200 µm channel and contacted through source/drain pads constituted from Au (90 nm)/Cr (10 nm) deposited by sputtering deposition and the electrode patterning and definition were done by photolithography: **(a)**. Subsequently, a 100 nm SiO_2 layer was deposited around the channel area to isolate the source/drain pads from the electrolyte, *i.e.,* only 20 µm × 200 µm of the source/drain electrodes were exposed to the analyte solution: **(b)**. The graphene was transferred using PMMA: **(c)**. To define the graphene channel, photolithography using PMGI [127] photoresist was applied as masking layer to protect the graphene channel, with extraneous graphene outside of the channel removed by Oxygen plasma dry etching: **(d)**. The GFET was further annealed at 200 °C for 2 h under a H_2/N_2 ambient: **(e)**. An analyte reservoir was made using Polydimethylsiloxane (PDMS) mold around the channel to hold the sample liquid on the graphene channel: **(f)**.

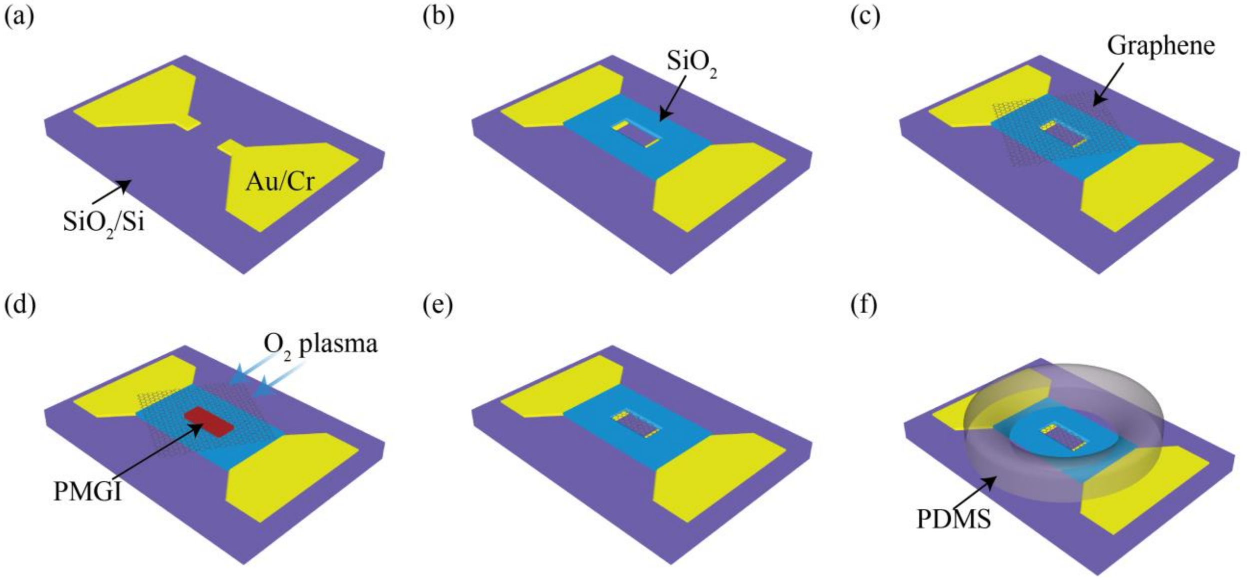

Figure4. 6 The graphene field effect transistor (GFET) fabrication processes, include (a) electrode patterning. (b) oxide (SiO$_2$) deposition, (c) Transfer of graphene, (d) definition of the graphene channel (e) FET definition, followed by (f) PDMS mold around the channel to hold the liquid analyte.

S3. Determination of the constitutive capacitive contributions in the GFET

The C_T (total capacitance) estimation was done by a Capacitance Bridge (AH 2700, Andeen Hagerling) with an *ac* voltage excitation of ~ 30 mV. The source and drain were grounded, and the C_T was measured between the connected source and drain pads of the graphene channel with respect to the gate probe, as a function of the **(a)** V_g, as well as (**b**) *ac* voltage frequency: Figure4. 7**(a)** Measured CT of the GFET as a function of the Vg, **(b)** The variation of the CT (at Vg =0) under at AC frequency. The inset represents the deployed capacitance model.**.** The C_T is constituted from a C_{EDL}: an electrolyte double layer capacitance in parallel to a capacitance C_P [128] contributed by the surface immobilized *Ap*, and a quantum capacitance (C_Q) in series with the C_{EDL} and C_P. The C_Q [= e^2 DOS (E_F)] is defined with respect to the density of states (DOS) of the graphene at the Fermi energy (E_F). See inset to Figure4. 7**(a)** Measured CT of the GFET as a function of the Vg, **(b)** The variation of the CT (at Vg =0) under at AC frequency. The inset represents the deployed capacitance model. **(b),** for the capacitance model, *i.e.*,

$$\frac{1}{C_T} = \left(\frac{1}{C_{EDL} + C_P} + \frac{1}{C_Q}\right) \tag{4.6}$$

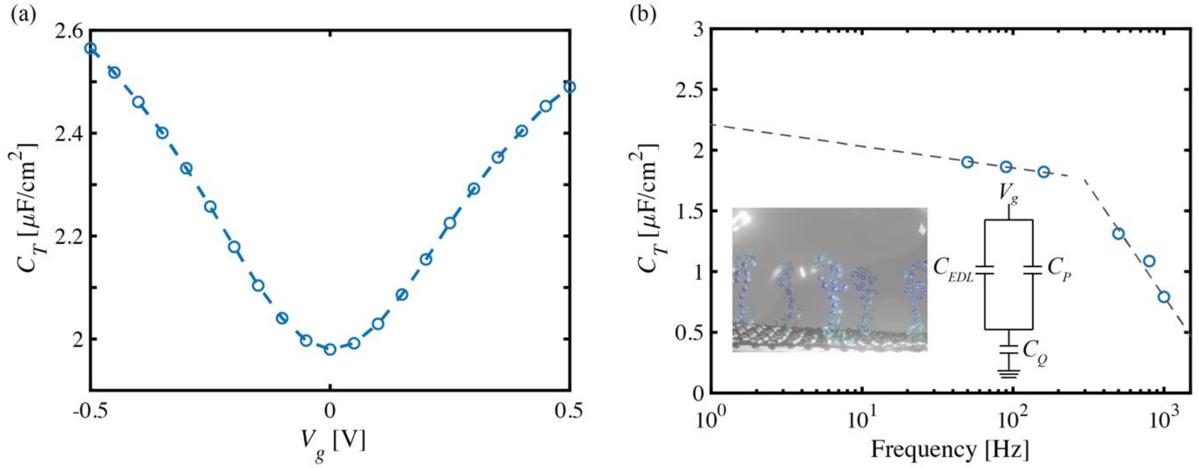

Figure4. 7**(a)** Measured C_T of the GFET as a function of the V_g, **(b)** The variation of the C_T (at V_g =0) under at AC frequency. The inset represents the deployed capacitance model.

As a function of the V_g (at 80 Hz), a U-shaped capacitance characteristic in Figure4. 7**(a)** Measured CT of the GFET as a function of the Vg, **(b)** The variation of the CT (at Vg =0) under at AC frequency. The inset represents the deployed capacitance model. **(a)** indicates a change of C_Q at different gate induced carrier density (n_g). The C_T as a function of frequency (AC frequency of 50 Hz, 80 Hz, 160 Hz, 500 Hz, 800 Hz and 1 kHz.), see Figure4. 7**(a)** Measured CT of the GFET as a function of the Vg, **(b)** The variation of the CT (at Vg =0) under at AC frequency. The inset represents the deployed capacitance model. (b). A cut-off frequency [129] at ~200 Hz was observed, below which there is a plateauing of the C_T at ~2 μF/cm^2.

When a gate bias was applied to an electrolyte, ions and/or dipoles in the electrolyte change their orientation to screen the electric field, forming an electrical double layer (EDL). The Gouy-Chapman-Stern (GCS) model [130,131] incorporates an associated capacitance: C_{EDL}, incorporating an immobile Stern layer of capacitance C_{SL} and a mobile diffuse layer of capacitance

C_{DL} in series. The C_{SL} (per unit area), related to the ionic adsorption on graphene surface, may be estimated by:

$$C_{SL} = \frac{\epsilon_{r,SL}\epsilon_0}{\lambda_{SL}} \tag{4.7}$$

Here, $\epsilon_{r,\,SL}$=6, ϵ_0 =8.85*10^{-12} F/m, λ_{SL}= 0. 3 nm (at [Pb^{2+}]<10nM) - based on the radius of hydrated H$^+$, OH$^-$ ions. A reduced ϵ of ~ 6 was used due to orientational ordering of water (a saturation effect) and depletion of water molecules (excluded volume effect) due to accumulation of counterions in the Stern layer [130]. From Eqn. 4.7, a C_{SL}~17.7 μF/cm^2 was obtained. The C_{DL} was estimated through:

$$C_{DL} = \frac{\epsilon_{r,DL}\epsilon_0}{\lambda_D} \tag{4.8}$$

Here, we used the permittivity of water $\epsilon_{r,DL}$= 78.5, a Debye screening length: $\lambda_D = \sqrt{\frac{\epsilon\epsilon_0 KT}{e^2\sum_j {z_j}^2 c_j}}$ ~ 965nm resulting in a C_{DL} ~ 0.072 μF/cm^2 and C_{EDL}~ C_{DL} ~0.072 μF/cm^2. The C_Q of ~9 μF/cm^2 was obtained from prior experiments in our group [132]. Given that C_T ~ 2 μF/cm^2, a C_P ~2.8 μF/cm^2 was indicated from Eqn. (4.6).

S4. Binding equilibria of the Aptamer-Pb^{2+} G-quadruplex (*APG*):

As indicated in the context of Eqns. (4.3) and (4.4), the Hills-Langmuir model was adopted to demonstrate the variation of the measured ΔV_D with respect to the *APG* formation. The V_D modulation was correlated to the quantity of the *APG* binding sites, from the induced positive charges into graphene channel. Consequently, the binding equilibrium of Hills adsorption, in terms of the fraction of *Ap* binding sites θ, can be expressed as:

$$\theta = \frac{APG \text{ binding sites}}{\text{total number of sites}} = \frac{[APG]}{[APG] + [Ap]} \tag{4.9}$$

From $K_d = \frac{[APG]}{[Ap][\mathrm{Pb}^{2+}]}$, we obtain

$$\theta = \frac{\left(\frac{[Ap][\mathrm{Pb}^{2+}]}{K_d}\right)}{\left(\frac{[Ap][\mathrm{Pb}^{2+}]}{K_d}\right) + [Ap]} = \frac{[\mathrm{Pb}^{2+}]}{[\mathrm{Pb}^{2+}] + K_d} \tag{4.10}$$

Consequently, when $K_d = [\mathrm{Pb}^{2+}]$, then half of the *Ap* would be occupied by Pb^{2+}, *i.e.,* $\theta = 0.5$.

S5. The influence of varying aptamer concentration

The investigation of the kinetics as a function of *Ap* concentration was done for 2 h of incubation, with 10 μM and 100 nM. By decreasing the *bulk* [*Ap*] from 10 μM to 100 nM - at the same incubation time (2 h), the LoD improved slightly from 7.3 pM to 1.0 pM with K_d of 10.5 nM and 0.3 nM, respectively: see Figure4. 8. Compared to the 30 mins 10 μM [*Ap*] incubation: Figure4. 3**(a)** The change in the VD (DVD) with [Pb2+], as a function of the Ap incubation time. **(b)** The determination of the LoB and LoD. (**c)** The variation of the transconductance (gm). **(d)** The Raman spectrum of the pristine graphene subsequent to 30 mins, 2 h, and 4 h of Ap incubation. **(e)**. The ratio between I2D and IG.**(a),** only a minor improvement in the LoD is inferred.

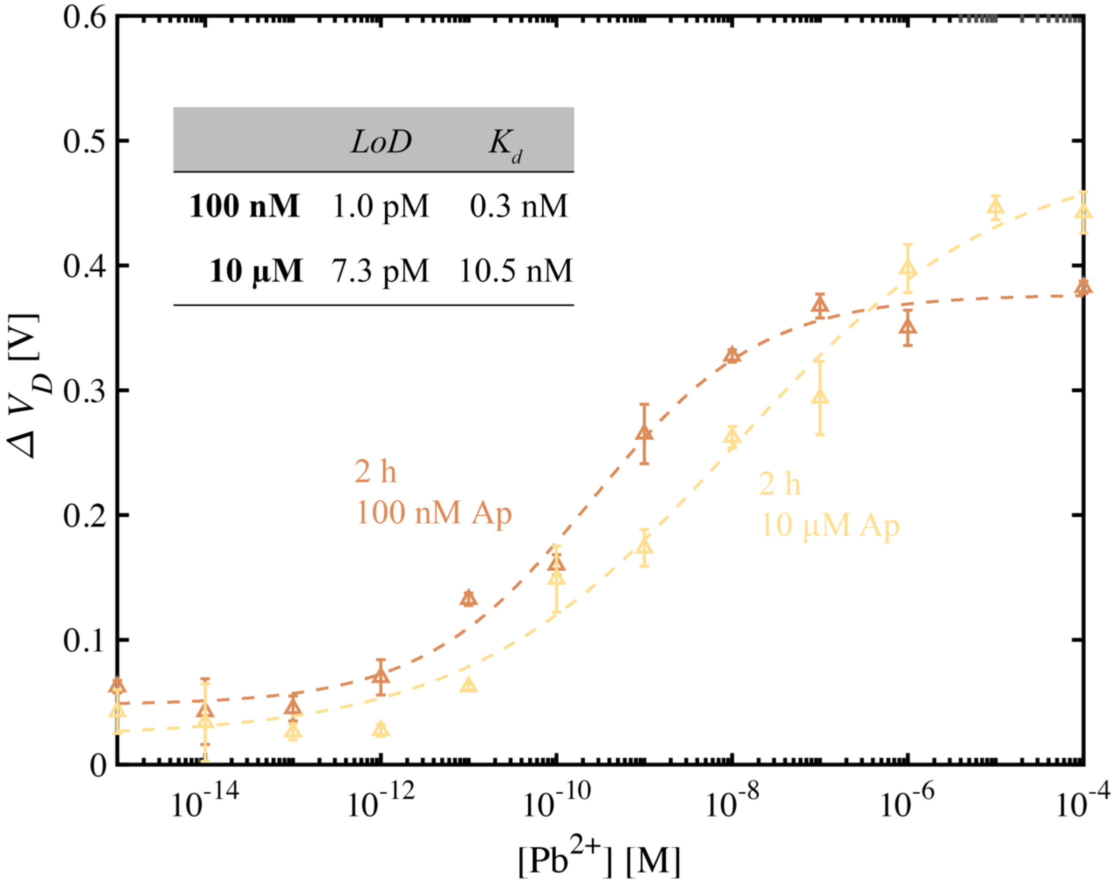

Figure4. 8 The effect of the Ap concentration effect on ΔV_D, at an aptamer concentration: [Ap] of 100 nM and 10 µM [Ap] incubated for 2 h.

Acknowledgements

Chapter 4, in full, has been submitted for publication of the material as it may appear in ACS Applied Nano Materials, 2022, Yongliang Dong, Alex W. Lee, Deependra Kumar Ban, Kesong Wang, Prabhakar Bandaru, 2022. The dissertation author was the primary researcher and author of this paper.

Conclusion and Future Work

Conclusion

In this thesis research, we have investigated both plasmonics and electronic sensors with graphene. The deployment of new materials is one of the key strategies to improve the performance of the sensor in terms of sensitivity and selectivity. In summary, the incorporation of graphene into the surface plasmonics polariton (SPP) resonance sensor and the electrolyte field effect transistor (FET) sensor was showing improved sensor performance.

The SPP sensor is designed and modeled numerically through the finite element simulation study. The metal/dielectric/metal (MDM) SPP resonance interaction has been a comprehensive study in the nanometer-scaled metallic structure, revealing the coupling and energy-splitting behavior. The interaction of SPP resonance was further incorporated with the graphene SPP (GrSPP), demonstrating the significant enhancement of GrSPP through the coupling. With the high GrSPP surface confinement and interaction between GrSPP and MDM SPP, the designed MDM coupled with graphene structure SPP surface refractive index sensitivity has been significantly improved.

Our work also indicated improved electrolyte-gated FET sensors with graphene implementation. The electrolyte-gated FET sensor was studied experimentally with a high throughput Graphene FET (GFET) fabrication process. The aptamer functionalized GFET was designed for detecting the lead ions in an aqueous solution, with a significantly low limit of detection of 61 femtomolar. The improvement has been modeled and understood by the Hills-Langmuir mechanism. We demonstrated that the incubation time effect is impacting the surface aptamer concentration on the graphene surface and further explained the mechanism of the improved sensitivity.

Future Work

The demonstrated improvement of sensor performance by graphene shows the potential application advantages. The development of graphene-related devices is still at an early stage and needs efforts to deliver high-quality, sensitive, and reliable devices. The current dissertation work demonstrated the potential enhanced sensitivity, which can be further improved and understood by the following approaches.

For the SPP resonance sensor, the currently designed GrSPP is working with significantly high doping levels, which is gating the experimental validation. Further investigation can be done to implement a low doping level of graphene or graphene nanoribbon to achieve the potential application regime. The experimental validation can be done through the following two approaches: first, the metal/dielectric/metal SPP resonance in the model can be synthesized by closely packed metallic nanocubes on the surface, which forms gaped SPP resonance along the parallel nanocube walls; second, the graphene can be exfoliated onto the hBN substrate, forming a potential ultra-flat surface for designed SPP resonance condition. Further numerical analysis and potential experimental validation could pave the way for graphene SPP sensors in real biomolecular refractive index-based detection.

The electrolyte-gated graphene field effect transistor sensors have been explored with multiple applications, with DNA, protein, antibody, aptamer, etc. We demonstrate a simple strategy to improve sensor sensitivity. The current experiment indicates a selective measurement of the lead ions, which can be further developed into other biomolecular sensors. We can investigate the current strategy to design clinically applicable GFET sensors to detect certain DNA, proteins, or disease. Additionally, the analytical understanding of the electrical potential on the surface functionalized graphene provides more insightful guidance into GFET sensor design. In future work, further graphene surface electrical characterization can be done through impedance measurement. We are currently applying electrochemical impedance spectroscopy to model the electrolyte interface behavior of the different functionalization groups on the GFET electrolyte interface. The strategy of sensitivity improvement and the fundamental understanding of the surface functionalization group will lead to a promising GFET sensor device development.

REFERENCES

1. National Research Council. Expanding the vision of sensor materials. National Academies Press, 1995.

2. Pedro Estrela, Nikhil Bhalla, Pawan Jolly, Nello Formisano, Pedro Estrela; Introduction to biosensors. Essays Biochem 30 June 2016; 60 (1): 1–8.

3. Lee, Sang Hun, Jong Hwan Sung, and Tai Hyun Park. "Nanomaterial-based biosensor as an emerging tool for biomedical applications." Annals of biomedical engineering40.6 (2012): 1384-1397.

4. Nehra, Anuj, and Krishna Pal Singh. "Current trends in nanomaterial embedded field effect transistor-based biosensor." Biosensors and Bioelectronics 74 (2015): 731-743.

5. Allen, Matthew J., Vincent C. Tung, and Richard B. Kaner. "Honeycomb carbon: a review of graphene." Chemical reviews110.1 (2010): 132-145.

6. Emani, N. K., Kildishev, A. V., Shalaev, V. M., & Boltasseva, A. (2015). Graphene: a dynamic platform for electrical control of plasmonic resonance. *Nanophotonics*, *4*(2), 214-223.

7. Syu, Yu-Cheng, Wei-En Hsu, and Chih-Ting Lin. "Field-effect transistor biosensing: Devices and clinical applications." *ECS Journal of Solid State Science and Technology* 7.7 (2018): Q3196.

8. S. A. Maier, Plasmonics: Fundamentals and Applications (Springer US, 2007).

9. W. L. Barnes, A. Dereux, and T. W. Ebbesen, "Surface plasmon subwavelength optics," Nature 424(6950), 824–830 (2003).

10. L. Liu, Z. Han, and S. He, "Novel surface plasmon waveguide for high integration," Opt. Express **13**(17), 6645 (2005).

11. C. Fei Guo, T. Sun, F. Cao, Q. Liu, and Z. Ren, "Metallic nanostructures for light trapping in energy-harvesting devices," Light Sci. Appl. 3(4), e161–e161 (2014).

12. S. V. Boriskina, H. Ghasemi, and G. Chen, "Plasmonic materials for energy: From physics to applications," Mater. Today **16**(10), 375–386 (2013).

13. S. Y. Ding, J. Yi, J. F. Li, B. Ren, D. Y. Wu, R. Panneerselvam, and Z. Q. Tian, "Nanostructure-based plasmon-enhanced Raman spectroscopy for surface analysis of materials," Nat. Rev. Mater. 1(6), (2016).

14. K. Kneipp, Y. Wang, H. Kneipp, L. T. Perelman, I. Itzkan, R. R. Dasari, and M. S. Feld, "Single molecule detection using surface-enhanced raman scattering (SERS)," Phys. Rev. Lett. (1997).

15. S. Nie and S. R. Emory, "Probing single molecules and single nanoparticles by surface-enhanced Raman scattering," Science (80-.). 275(5303), 1102–1106 (1997).

16. K. A. Willets and R. P. Van Duyne, "Localized Surface Plasmon Resonance Spectroscopy and Sensing," Annu. Rev. Phys. Chem. 58(1), 267–297 (2007).

17. E. N. Economou, "Surface Plasmons in Thin Films," Phys. Rev. **182**(2), 539–554 (1969).

18. I. P. Kaminow, W. L. Mammel, and H. P. Weber, "Metal-Clad Optical Waveguides: Analytical and Experimental Study," Appl. Opt. 13(2), 396 (1974).

19. J. Le Perchec, P. Quémerais, A. Barbara, and T. López-Ríos, "Why Metallic Surfaces with Grooves a Few Nanometers Deep and Wide May Strongly Absorb Visible Light," Phys. Rev. Lett. 100(6), 066408 (2008).

20. A. Moreau, C. Ciracì, J. J. Mock, D. R. Smith, R. T. Hill, A. Chilkoti, Q. Wang, and B. J. Wiley, "Controlled-reflectance surfaces with film-coupled colloidal nanoantennas," Nature **492**(7427), 86–89 (2012).

21. J. B. Lassiter, F. McGuire, J. J. Mock, C. Ciracì, R. T. Hill, B. J. Wiley, A. Chilkoti, and D. R. Smith, "Plasmonic waveguide modes of film-coupled metallic nanocubes," Nano Lett. **13**(12), 5866–5872 (2013).

22. G. M. Akselrod, J. Huang, T. B. Hoang, P. T. Bowen, L. Su, D. R. Smith, and M. H. Mikkelsen, "Large-Area Metasurface Perfect Absorbers from Visible to Near-Infrared," Adv. Mater. **27**(48), 8028–8034 (2015).

23. N. Bonod, G. Tayeb, D. Maystre, S. Enoch, and E. Popov, "Total absorption of light by lamellar metallic gratings," Opt. Express 16(20), 15431 (2008).

24. Z. Yong, S. Zhang, C. Gong, and S. He, "Narrow band perfect absorber for maximum localized magnetic and electric field enhancement and sensing applications," Sci. Rep. 6(March), 1–7 (2016).

25. M. Kuttge, F. J. García de Abajo, and A. Polman, "How grooves reflect and confine surface plasmon polaritons," Opt. Express 17(12), 10385 (2009).

26. Y. Cui, Y. He, Y. Jin, F. Ding, L. Yang, Y. Ye, S. Zhong, Y. Lin, and S. He, "Plasmonic and metamaterial structures as electromagnetic absorbers," Laser Photonics Rev. 8(4), 495–520 (2014).

27. D. Ji, H. Song, X. Zeng, H. Hu, K. Liu, N. Zhang, and Q. Gan, "Broadband absorption engineering of hyperbolic metafilm patterns," Sci. Rep. **4**(1), 4498 (2015).

28. K. Aydin, V. E. Ferry, R. M. Briggs, and H. A. Atwater, "Broadband polarization-independent resonant light absorption using ultrathin plasmonic super absorbers," Nat. Commun. 2(1), 517 (2011).

29. J. Hao, J. Wang, X. Liu, W. J. Padilla, L. Zhou, and M. Qiu, "High performance optical absorber based on a plasmonic metamaterial," Appl. Phys. Lett. **96**(25), 10–13 (2010).

30. Z. Sun and X. Zuo, "Tunable Absorption of Light via Localized Plasmon Resonances on a Metal Surface with Interspaced Ultra-thin Metal Gratings," Plasmonics 6(1), 83–89 (2011).

31. W. Zhou, J. Y. Suh, Y. Hua, and T. W. Odom, "Hybridization of Localized and Guided Modes in 2D Metal–Insulator–Metal Nanocavity Arrays," J. Phys. Chem. C 117(6), 2541–2546 (2013).

32. L. Lin and Y. Zheng, "Optimizing plasmonic nanoantennas via coordinated multiple coupling," Sci. Rep. 5, 1–11 (2015).

33. Y. Zhai, G. Chen, J. Xu, Z. Qi, X. Li, and Q. Wang, "Multiple-band perfect absorbers based on the combination of Fabry-Perot resonance and the gap plasmon resonance," Opt. Commun. 399(April), 28–33 (2017).

34. I. H. Malitson, "Interspecimen Comparison of the Refractive Index of Fused Silica*,†," J. Opt. Soc. Am. **55**(10), 1205 (1965).

35. A. Moreau, C. Lafarge, N. Laurent, K. Edee, and G. Granet, "Enhanced transmission of slit arrays in an extremely thin metallic film," J. Opt. A Pure Appl. Opt. **9**(2), 165–169 (2007).

36. E. S. Barnard, J. S. White, A. Chandran, and M. L. Brongersma, "Spectral properties of plasmonic resonator antennas," Opt. Express **16**(21), 16529 (2008).

37. H. Li, M. Qin, Y. Ren, and J. Hu, " Angle-independent strong coupling between plasmonic magnetic resonances and excitons in monolayer WS 2 ," Opt. Express 27(16), 22951 (2019).

38. Q. Lin, X. Zhai, L. L. Wang, X. Luo, G. D. Liu, J. P. Liu, and S. X. Xia, "A novel design of plasmon-induced absorption sensor," Appl. Phys. Express 9(6), (2016).

39. H.-J. Li, J.-G. Hu, L.-L. Wang, M. Qin, and Y.-Z. Ren, "Wavelength-Selective Wide-Angle Light Absorption Enhancement in Monolayers of Transition-Metal Dichalcogenides," J. Light. Technol. Vol. 36, Issue 16, pp. 3236-3241 36(16), 3236–3241 (2018).

40. H. H. Nguyen, J. Park, S. Kang, and M. Kim, “Surface plasmon resonance: a versatile technique for biosensor applications,” Sensors 15(5), 10481–10510 (2015).

41. Y. Zhao, R.-j. Tong, F. Xia, and Y. Peng, “Current status of optical fiber biosensor based on surface plasmon resonance,” Biosens. Bioelectron. 142, 111505 (2019).

42. J. Dostalek, J. Čtyroky, J. Homola, E. Brynda, M. Skalsk ` y, P. Nekvindova, J. Špirková, J. Škvor, and J. Schröfel, ` "Surface plasmon resonance biosensor based on integrated optical waveguide," Sensors actuators B: Chem. 76, 8–12 (2001).

43. K.-L. Lee, W.-S. Wang, and P.-K. Wei, "Sensitive label-free biosensors by using gap plasmons in gold nanoslits," Biosens. Bioelectron. 24, 210–215 (2008).

44. Y. Dong and P. R. Bandaru, "Interaction and hybridization of orthogonal fabry-pérot like surface plasmon modes in metal-dielectric grating structures," Opt. express 28, 3541–3551 (2020).

45. L. Wu, H. Chu, W. Koh, and E. Li, "Highly sensitive graphene biosensors based on surface plasmon resonance," Opt. express 18, 14395–14400 (2010).

46. K. N. Shushama, M. M. Rana, R. Inum, and M. B. Hossain, "Sensitivity enhancement of graphene coated surface plasmon resonance biosensor," Opt. Quantum Electron. 49, 1–13 (2017).

47. Q. Zhang, X. Li, M.M. Hossain, Y. Xue, J.Zhang, J. Song, J. Liu, M.D. Turner, S. Fan, Q. Bao, and M. Gu, "Graphene surface plasmons at the near-infrared optical regime," Sci. reports 4, 1–6 (2014).

48. S. Zeng, K.V. Sreekanth, J. Shang, T. Yu, C.K. Chen, F. Yin, D. Baillargeat, P. Coquet, H.P. Ho, A.V. Kabashin, and K.T. Yong, "Graphene–gold metasurface architectures for ultrasensitive plasmonic biosensing," Adv. Mater. 27, 6163–6169 (2015).

49. H. Zhang, D. Song, S. Gao, J. Zhang, H. Zhang, and Y. Sun, "Novel spr biosensors based on metal nanoparticles decorated with graphene for immunoassay," Sensors Actuators B: Chem. 188, 548–554 (2013).

50. P. K. Maharana, R. Jha, and P. Padhy, "On the electric field enhancement and performance of spr gas sensor based on graphene for visible and near infrared," Sensors Actuators B: Chem. 207, 117–122 (2015).

51. A. Verma, A. Prakash, and R. Tripathi, "Sensitivity enhancement of surface plasmon resonance biosensor using graphene and air gap," Opt. communications 357, 106–112 (2015).

52. Y. Wan, L. Deng, L. Wang, M. Yang, and Y. Wang, "Modulation of visible and near-infrared surface plasmon resonance of au nanoparticles based on highly doped graphene," Plasmonics 12, 1317–1324 (2017).

53. B. Zhao, and Z. M. Zhang. "Strong plasmonic coupling between graphene ribbon array and metal gratings." Acs Photonics 2.11 (2015): 1611-1618.

54. B. Zhao, J. M. Zhao, and Z. M. Zhang. "Resonance enhanced absorption in a graphene monolayer using deep metal gratings." JOSA B 32.6 (2015): 1176-1185.

55. K. Araki, and R. Z. Zhang. "Plasmon-resonance emission tailoring of “origami” graphene-covered photonic gratings." Optics Express 28.15 (2020): 22791-22802.

56. K. Araki, and R. Z. Zhang. "Mechano-Optical Resonant Emission by Edge Angle Modulation of Wrinkled Graphene on Plasmonic Metal Gratings." ACS Applied Nano Materials 4.8 (2021): 8399-8407.

57. J. Xue, J. Sanchez-Yamagishi, D. Bulmash, P. Jacquod, A. Deshpande, K. Watanabe, T. Taniguchi, P. Jarillo-Herrero, and B.J. LeRoy. "Scanning tunnelling microscopy and spectroscopy of ultra-flat graphene on hexagonal boron nitride." Nature materials 10.4 (2011): 282-285.

58. X. Luo, T. Qiu, W. Lu, and Z. Ni. "Plasmons in graphene: recent progress and applications." Materials Science and Engineering: R: Reports 74.11 (2013): 351-376.

59. F. H. Koppens, D. E. Chang, and F. J. García de Abajo. "Graphene plasmonics: a platform for strong light–matter interactions." Nano letters 11.8 (2011): 3370-3377.

60. Y. Francescato, V. Giannini, and S.A. Maier, "Strongly confined gap plasmon modes in graphene sandwiches and graphene-on-silicon." New Journal of Physics 15.6 (2013): 063020.

61. Z.H. Ni, H.M. Wang, J. Kasim, H.M. Fan, T. Yu, Y.H. Wu, Y.P. Feng, and Z.X. Shen, "Graphene thickness determination using reflection and contrast spectroscopy." Nano letters 7.9 (2007): 2758-2763.

62. D.K. Efetov, and P. Kim. "Controlling electron-phonon interactions in graphene at ultrahigh carrier densities." Physical review letters 105.25 (2010): 256805.

63. R.S. Shishir, F. Chen, J. Xia, N.J. Tao, and D.K. Ferry. "Room temperature carrier transport in graphene." Journal of computational electronics 8.2 (2009): 43-50.

64. J. Fang, W. G. Vandenberghe, and M. V. Fischetti. "Microscopic dielectric permittivities of graphene nanoribbons and graphene." Physical Review B 94.4 (2016): 045318.

65. A. Laturia, M.L. Van de Put, and W.G. Vandenberghe. "Dielectric properties of hexagonal boron nitride and transition metal dichalcogenides: from monolayer to bulk." npj 2D Materials and Applications 2.1 (2018): 1-7.

66. K. Li, J.M. Fitzgerald, X. Xiao, J.D. Caldwell, C. Zhang, S.A. Maier, X. Li, and V. Giannini. "Graphene plasmon cavities made with silicon carbide." ACS omega 2.7 (2017): 3640-3646.

67. S.H. Chang, and Y.L. Su, "Mapping of transmission spectrum between plasmonic and nonplasmonic single slits. I: resonant transmission." JOSA B 32.1 (2015): 38-44.

68. T. Fang, A. Konar, H. Xing, and D. Jena, "Carrier statistics and quantum capacitance of graphene sheets and ribbons." Applied Physics Letters 91.9 (2007): 092109.

69. Kriss, R., Pieper, K. J., Parks, J., & Edwards, M. A. (2021). Challenges of detecting lead in drinking water using at-home test kits. Environmental Science & Technology, 55(3), 1964-1972.

70. Nguyen, H., Sung, Y., O'Shaughnessy, K., Shan, X., & Shih, W. C. (2018). Smartphone nanocolorimetry for on-demand lead detection and quantitation in drinking water. Analytical chemistry, 90(19), 11517-11522.

71. Maity, A., Sui, X., Tarman, C. R., Pu, H., Chang, J., Zhou, G., Ren, R., Mao, S. and Chen, J. (2017). Pulse-driven capacitive lead ion detection with reduced graphene oxide field-effect transistor integrated with an analyzing device for rapid water quality monitoring. ACS sensors, 2(11), 1653-1661.

72. Pieper, K. J., Tang, M., & Edwards, M. A. (2017). Flint water crisis caused by interrupted corrosion control: Investigating "ground zero" home. Environmental science & technology, 51(4), 2007-2014.

73. Pieper, K. J.; Martin, R.; Tang, M.; Walters, L.; Parks, J.; Roy, S.; Devine, C.; Edwards, M. A. (2018). Evaluating water lead levels during the Flint water crisis. Environmental science & technology, 52(15), 8124-8132.

74. Masten, S. J., Davies, S. H., & Mcelmurry, S. P. (2016). Flint water crisis: what happened and why?. Journal ‐ American Water Works Association, 108(12), 22-34.

75. Lopez, P. D. United States Environmental Protection Agency Letter to Commissioner. (2019).

76. Lanphear, B. P.; Hornung, R.; Khoury, J.; Yolton, K.; Baghurst, P.; Bellinger, D. C.; Canfield, R. L.; Dietrich, K. N.; Bornschein, R.; Greene, T.; Rothenberg, S. J.; Needleman, H. L.; Schnaas, L.; Wasserman, G.; Graziano, J.; Roberts, R. (2005). Low-level environmental lead exposure and children's intellectual function: an international pooled analysis. Environmental health perspectives, 113(7), 894-899.

77. Wilbur, S. (2005). A comparison of the relative cost and productivity of traditional metals analysis techniques versus ICP-MS in High Throughput commercial laboratories. Agilent Technologies Application Note.

78. Tighe, M., Bielski, M., Wilson, M., Ruscio-Atkinson, G., Peaslee, G. F., & Lieberman, M. (2020). A sensitive XRF screening method for lead in drinking water. Analytical chemistry, 92(7), 4949-4953.

79. Li, Y., Wang, C., Zhu, Y., Zhou, X., Xiang, Y., He, M., & Zeng, S. (2017). Fully integrated graphene electronic biosensor for label-free detection of lead (II) ion based on G-quadruplex structure-switching. Biosensors and Bioelectronics, 89, 758-763.

80. Xu, K., Meshik, X., Nichols, B. M., Zakar, E., Dutta, M., & Stroscio, M. A. (2014). Graphene- and aptamer-based electrochemical biosensor. Nanotechnology, 25(20), 205501.

81. Wang, C., Cui, X., Li, Y., Li, H., Huang, L., Bi, J., ... & Miao, F. (2016). A label-free and portable graphene FET aptasensor for children blood lead detection. Scientific reports, 6(1), 1-8.

82. Wen, Y., Li, F.Y., Dong, X., Zhang, J., Xiong, Q. and Chen, P. (2013), The Electrical Detection of Lead Ions Using Gold-Nanoparticle- and DNAzyme-Functionalized Graphene Device. Advanced Healthcare Materials, 2: 271-274.

83. Falina, S., Syamsul, M., Rhaffor, N. A., Sal Hamid, S., Mohamed Zain, K. A., Abd Manaf, A., & Kawarada, H. (2021). Ten years progress of electrical detection of heavy metal ions (HMIs) using various field-effect transistor (FET) nanosensors: A Review. Biosensors, 11(12), 478.

84. Yang, D., Liu, X., Zhou, Y., Luo, L., Zhang, J., Huang, A., Mao, Q., Chen, X. & Tang, L. (2017). Aptamer-based biosensors for detection of lead (ii) ion: a review. Analytical Methods, 9(13), 1976-1990.

85. Aliakbarinodehi, N., Jolly, P., Bhalla, N., Miodek, A., De Micheli, G., Estrela, P., & Carrara, S. (2017). Aptamer-based field-effect biosensor for tenofovir detection. Scientific reports, 7(1), 1-10.

86. Nakatsuka, N., Yang, K. A., Abendroth, J. M., Cheung, K. M., Xu, X., Yang, H., Zhao, C., Zhu, B., Rim, Y.S., Yang, Y., Weiss, P.S., & Andrews, A. M. (2018). Aptamer–field-effect transistors overcome Debye length limitations for small-molecule sensing. Science, 362(6412), 319-324.

87. Kumar, N., Rana, M., Geiwitz, M., Khan, N. I., Catalano, M., Ortiz-Marquez, J. C., Kitadai, H., Weber, A., Dweik, B., Ling, X., van Opijnen, T., & Burch, K. S. (2022). Rapid, multianalyte detection of opioid metabolites in wastewater. ACS nano, 16(3), 3704-3714.

88. Cai, S., Yan, J., Xiong, H., Liu, Y., Peng, D., & Liu, Z. (2018). Investigations on the interface of nucleic acid aptamers and binding targets. Analyst, 143(22), 5317-5338.

89. Gao, Z., Xia, H., Zauberman, J., Tomaiuolo, M., Ping, J., Zhang, Q., Ducos, P., Ye, H., Wang, S., Yang, X., Lubna, F., & Johnson, A. T. C. (2018). Detection of sub-fM DNA with target recycling and self-assembly amplification on graphene field-effect biosensors. Nano letters, 18(6), 3509-3515.

90. Ping, J., Vishnubhotla, R., Vrudhula, A., & Johnson, A. C. (2016). Scalable production of high-sensitivity, label-free DNA biosensors based on back-gated graphene field effect transistors. ACS nano, 10(9), 8700-8704.

91. Xu, S., Zhan, J., Man, B., Jiang, S., Yue, W., Gao, S., ... & Zhou, Y. (2017). Real-time reliable determination of binding kinetics of DNA hybridization using a multi-channel graphene biosensor. Nature communications, 8(1), 1-10.

92. Dong, X., Shi, Y., Huang, W., Chen, P., & Li, L. J. (2010). Electrical detection of DNA hybridization with single‐base specificity using transistors based on CVD‐grown graphene sheets. Advanced Materials, 22(14), 1649-1653.

93. Seo, G., Lee, G., Kim, M. J., Baek, S. H., Choi, M., Ku, K. B., Lee, C.S., Jun, S., Park, D., Kim, H.G., Kim, S.J., & Kim, S. I. (2020). Rapid detection of COVID-19 causative virus (SARS-CoV-2) in human nasopharyngeal swab specimens using field-effect transistor-based biosensor. ACS nano, 14(4), 5135-5142.

94. Kang, H., Wang, X., Guo, M., Dai, C., Chen, R., Yang, L., ... & Wei, D. (2021). Ultrasensitive detection of SARS-CoV-2 antibody by graphene field-effect transistors. Nano Letters, 21(19), 7897-7904.

95. Kaisti, M. (2017). Detection principles of biological and chemical FET sensors. Biosensors and Bioelectronics, 98, 437-448.

96. Meng, Z., Stolz, R. M., Mendecki, L., & Mirica, K. A. (2019). Electrically-transduced chemical sensors based on two-dimensional nanomaterials. Chemical reviews, 119(1), 478-598.

97. Sakata, T. (2019). Biologically coupled gate field-effect transistors meet in vitro diagnostics. ACS omega, 4(7), 11852-11862.

98. Vu, C. A., & Chen, W. Y. (2019). Field-effect transistor biosensors for biomedical applications: recent advances and future prospects. Sensors, 19(19), 4214.

99. Da Costa, C. P., & Sigel, H. (2000). Lead (II)-binding properties of the 5 ‘-monophosphates of adenosine (AMP2-), inosine (IMP2-), and guanosine (GMP2-) in aqueous solution. Evidence for nucleobase− lead (II) interactions. Inorganic Chemistry, 39(26), 5985-5993.

100. Sigel, H., Da Costa, C. P., & Martin, R. B. (2001). Interactions of lead (II) with nucleotides and their constituents. Coordination Chemistry Reviews, 219, 435-461.

101. Liu, W., Fu, Y., Zheng, B., Cheng, S., Li, W., Lau, T. C., & Liang, H. (2011). Kinetics and mechanism of conformational changes in a G-quadruplex of thrombin-binding aptamer induced by Pb2+. The Journal of Physical Chemistry B, 115(44), 13051-13056.

102. Yang, Y., Li, W., & Liu, J. (2021). Review of recent progress on DNA-based biosensors for Pb2+ detection. Analytica Chimica Acta, 1147, 124-143.

103. Xu, G., Abbott, J., Qin, L., Yeung, K. Y., Song, Y., Yoon, H., ... & Ham, D. (2014). Electrophoretic and field-effect graphene for all-electrical DNA array technology. Nature communications, 5(1), 1-9.

104. Fu, W., Feng, L., Panaitov, G., Kireev, D., Mayer, D., Offenhäusser, A., & Krause, H. J. (2017). Biosensing near the neutrality point of graphene. Science advances, 3(10), e1701247.

105. Chen, F., Qing, Q., Xia, J., & Tao, N. (2010). Graphene Field‐Effect Transistors: Electrochemical Gating, Interfacial Capacitance, and Biosensing Applications. Chemistry–An Asian Journal, 5(10), 2144-2153.

106. Torricelli, F., Adrahtas, D. Z., Bao, Z., Berggren, M., Biscarini, F., Bonfiglio, A., ... & Torsi, L. (2021). Electrolyte-gated transistors for enhanced performance bioelectronics. Nature Reviews Methods Primers, 1(1), 1-24.

107. Ang, P. K., Chen, W., Wee, A. T. S., & Loh, K. P. (2008). Solution-gated epitaxial graphene as pH sensor. Journal of the American Chemical Society, 130(44), 14392-14393.

108. Ohno, Y., Maehashi, K., Yamashiro, Y., & Matsumoto, K. (2009). Electrolyte-gated graphene field-effect transistors for detecting pH and protein adsorption. Nano letters, 9(9), 3318-3322.

109. Khan, N. I., Mousazadehkasin, M., Ghosh, S., Tsavalas, J. G., & Song, E. (2020). An integrated microfluidic platform for selective and real-time detection of thrombin biomarkers using a graphene FET. Analyst, 145(13), 4494-4503.

110. Chu, S. W., Baek, S. J., Kim, D. C., Seo, S., Kim, J. S., & Park, Y. W. (2012). Charge transport in graphene doped with diatomic halogen molecules (I2, Br2) near Dirac point. Synthetic metals, 162(17-18), 1689-1693.

111. Kim, S., Nah, J., Jo, I., Shahrjerdi, D., Colombo, L., Yao, Z., Tutuc, E. & Banerjee, S. K. (2009). Realization of a high mobility dual-gated graphene field-effect transistor with Al 2 O 3 dielectric. Applied Physics Letters, 94(6), 062107.

112. Dorgan, V. E., Bae, M. H., & Pop, E. (2010). Mobility and saturation velocity in graphene on SiO 2. Applied Physics Letters, 97(8), 082112.

113. Palazzo, G., De Tullio, D., Magliulo, M., Mallardi, A., Intranuovo, F., Mulla, M. Y., Favia, P., Vikholm‐Lundin, I. & Torsi, L. (2015). Detection Beyond Debye's Length with an Electrolyte‐Gated Organic Field‐Effect Transistor. Advanced Materials, 27(5), 911-916.

114. Li, J., & Burke, P. J. (2019). Measurement of the combined quantum and electrochemical capacitance of a carbon nanotube. Nature communications, 10(1), 1-9.

115. Armbruster, D. A., & Pry, T. (2008). Limit of blank, limit of detection and limit of quantitation. The clinical biochemist reviews, 29(Suppl 1), S49.

116. Das, A., Pisana, S., Chakraborty, B., Piscanec, S., Saha, S. K., Waghmare, U. V., Novoselov, K.S., Krishnamurthy, H.R., Geim, A.K., Ferrari, A.C. & Sood, A. K. (2008). Monitoring dopants by Raman scattering in an electrochemically top-gated graphene transistor. Nature nanotechnology, 3(4), 210-215.

117. Wang, X., Zhu, Y., Olsen, T. R., Sun, N., Zhang, W., Pei, R., & Lin, Q. (2018). A graphene aptasensor for biomarker detection in human serum. Electrochimica acta, 290, 356-363.

118. Liu, J., Li, Q., Zou, Y., Qian, Q., Jin, Y., Li, G., Jiang, K. & Fan, S. (2013). The dependence of graphene Raman D-band on carrier density. Nano letters, 13(12), 6170-6175.

119. Bruna, M., Ott, A. K., Ijäs, M., Yoon, D., Sassi, U., & Ferrari, A. C. (2014). Doping dependence of the Raman spectrum of defected graphene. Acs Nano, 8(7), 7432-7441.

120. Buledi, J. A., Amin, S., Haider, S. I., Bhanger, M. I., & Solangi, A. R. (2021). A review on detection of heavy metals from aqueous media using nanomaterial-based sensors. Environmental Science and Pollution Research, 28(42), 58994-59002.

121. López, Y. C., Ortega, G. A., & Reguera, E. (2022). Hazardous ions decontamination: from the element to the material. Chemical Engineering Journal Advances, 100297.

122. Purwidyantri, A., Domingues, T., Borme, J., Guerreiro, J. R., Ipatov, A., Abreu, C. M., Martins, M., Alpuim, P. & Prado, M. (2021). Influence of the electrolyte salt concentration on DNA detection with graphene transistors. Biosensors, 11(1), 24.

123. Jarczewska, M., Kierzkowska, E., Ziółkowski, R., Górski, Ł., & Malinowska, E. (2015). Electrochemical oligonucleotide-based biosensor for the determination of lead ion. Bioelectrochemistry, 101, 35-41.

124. Xu, S., Chen, X., Peng, G., Jiang, L., & Huang, H. (2018). An electrochemical biosensor for the detection of Pb2+ based on G-quadruplex DNA and gold nanoparticles. Analytical and bioanalytical chemistry, 410(23), 5879-5887.

125. Li, X., Magnuson, C. W., Venugopal, A., Tromp, R. M., Hannon, J. B., Vogel, E. M., Colombo, L. & Ruoff, R. S. (2011). Large-area graphene single crystals grown by low-pressure chemical vapor deposition of methane on copper. Journal of the American Chemical Society, 133(9), 2816-2819.

126. Kim, S., Shin, S., Kim, T., Du, H., Song, M., Lee, C., Kim, K., Cho, S., Seo, D.H. & Seo, S. (2016). Robust graphene wet transfer process through low molecular weight polymethylmethacrylate. Carbon, 98, 352-357.

127. Gao, Z., Kang, H., Naylor, C. H., Streller, F., Ducos, P., Serrano, M. D., Ping, J., Zauberman, J., Carpick, R.W., Wang, Y.J., Park, Y.W., & Johnson, A. C. (2016). Scalable production of sensor arrays based on high-mobility hybrid graphene field effect transistors. ACS Applied Materials & Interfaces, 8(41), 27546-27552.

128. Palazzo, G., De Tullio, D., Magliulo, M., Mallardi, A., Intranuovo, F., Mulla, M. Y., Favia, P., Vikholm‐Lundin, I. & Torsi, L. (2015). Detection Beyond Debye's Length with an Electrolyte‐Gated Organic Field‐Effect Transistor. Advanced Materials, 27(5), 911-916.

129. Ki Min, B., Kim, S. K., Jun Kim, S., Ho Kim, S., Kang, M. A., Park, C. Y., Song, W., Myung, S., Lim, J. & An, K. S. (2015). Electrical double layer capacitance in a graphene-embedded Al2O3 gate dielectric. Scientific reports, 5(1), 1-7.

130. Macdonald, J. R. (1987). Impedance spectroscopy and its use in analyzing the steady-state AC response of solid and liquid electrolytes. Journal of electroanalytical chemistry and interfacial electrochemistry, 223(1-2), 25-50.

131. Khademi, M., & Barz, D. P. (2020). Structure of the electrical double layer revisited: Electrode capacitance in aqueous solutions. Langmuir, 36(16), 4250-4260.

132. Narayanan, R., Yamada, H., Karakaya, M., Podila, R., Rao, A. M., & Bandaru, P. R. (2015). Modulation of the electrostatic and quantum capacitances of few layered graphenes through plasma processing. Nano letters, 15(5), 3067-3072.

Notes:

- *Single space within each entry. Double space in between entries.*
- *No “et al.” or “. . .” allowed; add full author list.*
- *Work with your faculty advisor to determine your citation style (MLA, APA, etc.) – any style is accepted, just be consistent between all references.*

******Students are responsible for adhering to all requirements as described in the manual. This template contains auto-features that are optional. Use at your own discretion. Graduate Division does not provide any technical support.******